NUMERICAL AND SEMI-EMPIRICAL MODELING OF PARTICLES UNDERGOING PHASE CHANGE UNDER THE INFLUENCE OF CONVECTION

by

Hemant Bansal

A thesis submitted in partial fulfillment of the requirements for the degree of

Master of Science

in

Chemical Engineering

Department of Chemical and Materials Engineering
University of Alberta

Abstract

This work is devoted to the development and validation of subgrid models describing heat and mass transfer between the bulk flow of gas/liquid and a moving particle undergoing phase change under the influence of free/mixed/forced convection. Such kind of submodels plays the role of '*scale bridges*' between microscale (e.g. interfacial phenomena) and macroscale phenomena (e.g. continuous casting). Applied to the multiscale modeling, our new model serves as a coupling between equations describing particle movement in Lagrangian space and mass, momentum, heat and species conservation equations defining melt flow in Eulerian space. Input parameters are Reynolds number (Re), Grashof number (Gr), Stefan number (Ste) and Prandtl number (Pr). The models have been validated against experimental data published recently in the literature applied to the melting of spherical and cylindrical ice particle under different flow conditions. Good agreement between numerical predictions and experimental data is observed. Additionally, some of the experiments are repeated numerically using CFD-based particle-resolved simulations. Basic flow features are discussed. Finally, the models developed for a single particle can be adopted for multi-particles systems.

Preface

Chapter 2 was partially based on a manuscript accepted for publication as "H. Bansal, P. Nikrityuk. A submodel for spherical particles undergoing phase change under the influence of convection. Can. J. Chem. Eng. accepted, 2016". Dr. Petr Nikrityuk was responsible for development and formulation of submodels. I was responsible for their programming, carrying out simulations, their validation against the existing experimental data in literature and explanation of the results obtained.

Acknowledgements

There are many people in my list to whom I am sincerely grateful for their support and help. The first and most earnest acknowledgement must go to my mentor and my supervisor, **Dr. Petr Nikrityuk** for his everlasting enthusiasm, guidance and encouragement for my research throughout my Masters. He was always ready to provide me with intelligent and ingenious ideas and knowledge about CFD in general. Apart from my research, he equipped me with lot of useful insights in time management, career goals and life outside academia. I pay my deepest gratitude to him and I am deeply indebted to him for all his efforts and help.

I would also like to thank Dr. Sina Ghaemi for allowing me to conduct experiments in his lab. I am grateful to Dipl.-Math. Frank Dierich for helping me in QUICK discretization scheme implementation.

I would like to thank all my friends at Windsor Park Plaza for providing me a temporary place to eat, stay and sleep whenever I needed. Also, I would like to thank my friends in Edmonton: Amit Dahiya, Tarang Jain, Nikhil Agrawal, Nanami Shimizu, Rohtaz Singh, Sahil Kapila, Kaushik Sivaramakrishnan, Hemant Charaya for sharing their time and joy with me.

At last but not the least, I would like to express my gratitude to my mom, dad and my sister for their love, constant support and encouragement. Without them, I can't imagine myself doing what I am doing today.

Table of Contents

List of Tables

List of Figures

List of Symbols

t	time
l	length
r	radius
d	diameter
v	volume
T	temperature
u	velocity
g	acceleration due to gravity
ρ	density
c	specific heat
μ	dynamic viscosity
ν	kinematic viscosity
h	heat transfer coefficient
h_{sf}	latent heat of fusion
h_v	latent heat of evaporation
k	thermal conductivity
r_t	radius at which average temperature lies
l_t	length at which average temperature lies
β	thermal expansion coefficient
α	thermal diffusivity
y	mass fraction
q	heat rate
$q"$	heat flux rate
$\dot{m}"$	mass flux rate
$\dot{m}$	rate of change of mass
D_{lg}	diffusion coefficient between liquid vapor and ambient gas
δ	layer thickness

ϵ	emissivity
α_{ab}	absorptivity
τ	transmissivity
σ	Stefan–Boltzmann constant
Nu	Nusselt number
Gr	Grashof number
Re	Reynolds number
Pr	Prandtl number
Ra	Rayleigh number
Ste	Stefan number
Ph	Phase change number

Subscripts

p	particle
s	side surface
t	top surface
b	bottom surface
m	melting/interface
l	liquid
∞	ambient
c	convection
bl	boundary layer

Superscripts

c	characteristic length

Chapter 1

Introduction

1.1 Particle flow with phase change: Applications

There are numerous instances in natural and engineering processes when solid-liquid two-phase flows are encountered. Flow behavior of solid–liquid two-phase flow systems depends on the properties of the dispersed solid phase, the continuous liquid phase that suspends the solids, and the interactions between the two phases. Dispersed solid phase can undergo dissolution, phase change or can participate in chemical reaction depending upon the nature of the system. This study specifically deals with the case when solid phase undergoes phase change. There are many industrial applications which deal with the phase changing solid-liquid two phase flows such as metal casting technology, injection moulding of polymers etc. In the context of casting technology, understanding of solidification processes under the influence of gravity-driven convection in a liquid phase is absolute necessary for any technological breakthrough in the design of new materials or in enhancement of material quality. Fig. 1.2 shows the dendrite formation in a solidifying alloy. Despite the long history of industrial casting technology, there are still many little-investigated phenomena which, if better understood, could significantly improve the process of industrial casting such as:

- Impact of the bulk flow on the phase change dynamics taking into account the three-dimensionality of solidification front.
- Transport of free-floating dendrites (if exist) in bulk flow
- Interaction between bulk flow turbulence and solidification front
- Impact of bulk flow on the heat and mass transfer between free floating dendrites and the melt

It is difficult to understand these phenomena through the experiments because of the complexity involved and their microscopic nature. The adequate numerical modeling of transport and expansion of free-floating equiaxed dendrites in the melt flow can address this problem and thereby can open the gate to the designing of high quality materials.

This study focuses on the numerical modeling of particulate flow system with particles undergoing phase change in the liquid of same material. Thus, the numerical model will solve a two-phase one-component system.

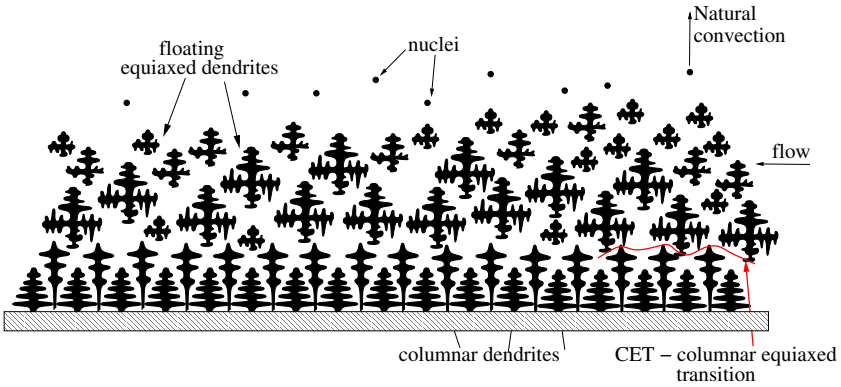

Figure 1.1: Free floating equiaxed dendrites and columnar dendrites in solidifying alloy

1.2 Modeling concepts and basic challenges

The extraordinary development of computers specially multicore processors along with the reduction in their price over last two decades have made it possible to perform sophisticated scientific computations on many important chemical engineering phenomena which are experimentally difficult to study. For e.g., slurry transport processes, fluidized beds, pneumatic transport processes etc. Moreover, experiments are often expensive to conduct. In lieu of this, various CFD packages like ANSYS-FLUENT, Flow-3D, COMSOL, openFOAM etc. and open source codes have appeared to efficiently solve these processes numerically. Particulate flow with particles undergoing phase change is one of the important engineering phenomena which are difficult to analyze experimentally. Specially, the study of morphology of melting/solidifying particles experimentally can be very expensive. Numerical modeling of particulate flow with particles undergoing phase change is a multiscale problem. The phenomena such as solidification sequence of the particles, shrinkage cavity formation, macrosegregation formations are governed by the mass, momen-

tum, heat and species transport equations solved in system scale (or macroscopic scale) whereas modeling of solidification morphology, particle growth (in case of solidification) or decay (in case of melting) requires the use of microscopic scales. There has been lot of research efforts in the past to numerically model this phenomena. A lot of CFD numerical models have been developed for particulate flows. However, particulate flows with particles undergoing solidification or melting (in other words, phase change) are still not modeled properly. In general, mathematical models used for the numerical simulation of particulate flow systems can be divided into two categories: Euler-Euler models and Euler-Lagrangian models as shown in fig. 1.2.

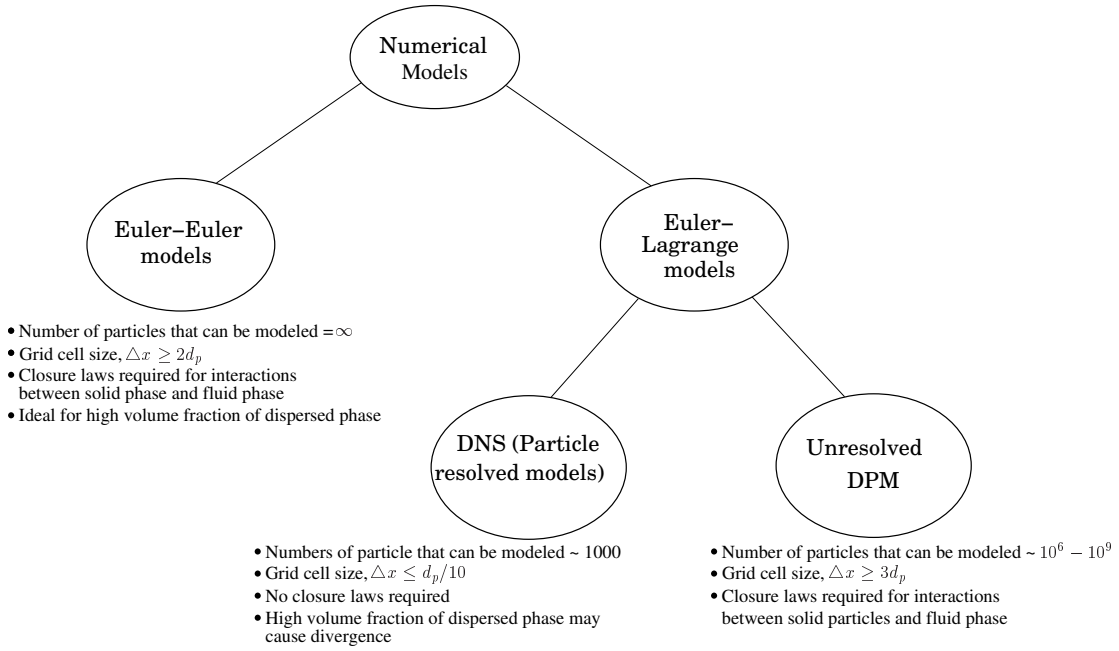

Figure 1.2: Flowchart of numerical models used to solve multiphase flow problems

1.2.1 Euler-Euler Models

Euler-Euler (EE) models drop the concept of solid phase consisting of individual discrete particles. Both the fluid phase and solid phase are considered as interpenetrating continuum. Volume-averaged mass, momentum and energy conservation equations are written for each phase in Eulerian space. Additional source terms in each conservation equation are responsible for the mass, momentum, energy and species concentration exchange between the solid phase and fluid phase. These source terms, often termed as closure laws, are often based on heuristics which is the primary drawback of this model. These models escape the requirement of equa-

tions describing the collision between particles which takes up lot of computational time in Euler-Lagrange models. However, collision of particles with the walls need to be modeled. Polydisperse systems i.e. systems having different sized particles are hard to solve using EE models because size distribution requires the solution of several sets of conservation equations. Due to the low resolution requirement of grid, these models are computationally least expensive but require lots of effort to develop the closure laws.

Applied to the casting technology, equiaxed globular solidification has caught special attention of various researchers because of its easy-to-define morphology. In equiaxed globular solidification, it is assumed that only free floating equiaxed dendrites are involved in the solidification i.e. columnar dendrites are ignored. Thus, dendrites in this case can be simplified as spheres and overall dendrite size can be expressed with a volume-averaged diameter. This also simplifies and avoid uncertainties in the equations required to predict the morphological details of the dendrites.

Wang and Beckermann [7] developed first ever Euler-Euler model for multiscale modeling of solidification. The model described the equiaxed dendritic solidification of an alloy taking into account the melt flow, transport of particles as well as the grain nucleation and growth mechanisms taking place over microscopic scales. The conservation equations for mass, momentum, species and heat was written for both the phases and separate exchange terms were included in each of the conservation equations to describe the mass, momentum, heat and species transport between the dendrites and fluid at dendrite-fluid interface. These exchange terms in each conservation equation were divided into two terms; exchanges due to diffusion across interface and exchanges due to the movement of interface (because of solidification or melting). A separate equation for conservation of number of dendrites was also written. The generation of new dendrites in the solidifying fluid was represented using the 'nucleation rate' term in the conservation equation of number of dendrites. Several supplementary relations were written in the model to define various terms like interfacial area concentration, nucleation rate, grain growth, particle density etc. Due to the lack of realistic supplementary relations and exchange terms, this model failed to agree well with the observed experimental phenomena. However, this was one promising starting model for the multiscale modeling of particulate flow with phase change. Ludwig and Wu [8] modified the above mentioned model [7]. Similar to previous model, they also provided the model for the equiaxed dendritic solidification of an two-component alloy. More emphasis was given on microscopic modeling, i.e., the definition of different exchange terms for the macroconservation

equations. Some of the supplementary relations like definition of nucleation rate were modified to make the model more realistic. At the end of the paper, many important physical phenomena were explained including macrosegregation, grain settlement. However, there was no validation of the results.

Later, Wu, Ludwig, Bührig-Polaczek, Fehlbier, and Sahm [9] used above model and presented different case studies of solidification in an aluminum casting to study the influence of melt convection and grain movement on the process. They played with the some model parameters such as grain movement, slip/non-slip boundary conditions etc. to create three different cases of movement of grains inside the casting mold. In one case, they did not consider the movement of grains and in two other cases, the grains were allowed to move. It was shown that grain movement was the prime cause of macrosegregation inside the mold. Movement of grains changes the local density of grains at different locations. Once the grain density becomes more than the packing limit of grains (as defined in the numerical model), they stop moving and oncoming grains adhere and settle there. It was shown that the inclusion of grain movement changes the solidification sequence and isotherms were also changed. Without any grain movement, solidification front and isotherms proceed equally from the bottom and side walls whereas with grain movement, solidification front and isotherms proceed much faster from the bottom regions as compared to the side regions. One of the drawbacks as said by the authors was the model's incapability to consider free surface boundary condition. So, constant pressure boundary condition was implemented at the casting top. This allows hot melt to continuously enter into the casting mold to compensate for the volume decrease caused by solidification shrinkage ($\rho_l > \rho_s$). This basically meant that casting could never be solidified completely.

Ludwig and Wu [10] modeled the columnar to equiaxed transition (CET) using the three phase Eulerian approach. Three phases were parent melt, the solidifying columnar dendrites and the solidifying equiaxed dendrites. Spherical morphology for equiaxed and cylindrical morphology for columnar dendrites is assumed. Conservation equations were solved for all the three phases. Momentum conservation equation for columnar dendrite phase was not solved because it was considered to be stationary. Additional transport equation for the number density of equiaxed grains was also written taking into account the grain nucleation term. Several supplementary relations were defined for diffusion controlled growth for both columnar and equiaxed phases, drag forces between the phases, species partitioning at the solid-liquid interface etc.. As said by the authors, most challenging point in this model was to define the closure laws for the competitive growth of both the solid

phases and mechanical interaction between the two phases. The stationary columnar dendrites are considered to generate at the mold wall and grows preferentially along the heat flow direction. CET occurs at the end of solidification when columnar dendrite tips are blocked by equiaxed grains. A binary steel ingot casting was simulated to demonstrate the model potentials. Motion of the columnar tip front, occurrence of CET, etc. were studied and their effect on the final macroscopic phase was studied. The results of the model were claimed to reproduce the widely accepted explanations of experimental findings.

Wu and Ludwig [11] presented a summary of previous model for equiaxed solidification with slight modifications. In second part of this study [12], the model provided was validated with an existing experimental result in literature. Discrepancies from the experiment were very large and few model parameters and assumptions like grain morphological parameters and determination of diffusion lengths in different phase regions were said to be the most critical factors influencing the model results.

As seen, despite considerable progress in the multiscale modeling of solidification using Euler-Euler models, existing models are very often not capable of reproducing the experimentally observed phenomena. The main limitation of EE models is the requirement of closure laws to describe the interactions between the solid and fluid phase.

1.2.2 Euler-Lagrange Models

The Euler-Lagrange models can be used as an alternative approach for adequately forecasting multiscale solidification/melting process with free floating dendrites. In this approach, solid particles are considered as individual discrete distinguishable particles. Motion of solid particles is treated individually using Newton's law of motion. Fluid flow is solved with a fixed Eulerian grid with Navier-Stokes equation.

DNS methods

Euler-Lagrange models can be divided into two categories depending upon the method used to couple the two phases. First category is Resolved discrete particle model (RDPM) or Direct Numerical Simulation (DNS) in which all the particles are fully resolved using appropriate fine grid. Grid size should be at least one order of magnitude smaller than the particle size. All continuum time and length scales are fully resolved in this class of numerical modeling. Thus, these models have the highest requirement of physical resolution due to which they need least modeling

effort. However, high physical resolution entails high computational cost. Due to computationally expensive in nature, these models can only predict solidification phenomena for limited number of particles using even one of the fastest computers available today.

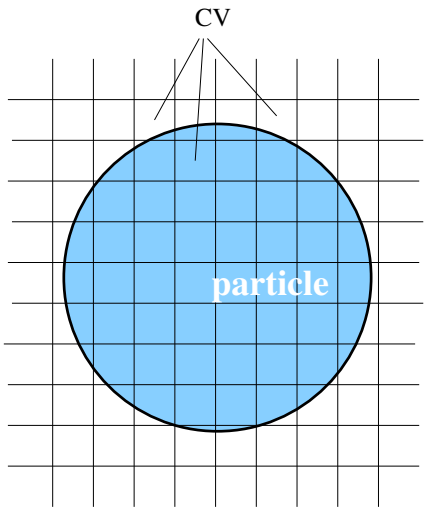

Figure 1.3: Fully resolved Eulerian grid in non-body fitted Direct Numerical Simulation (DNS) methods

Depending upon the type of grid used, DNS methods can be classified into two families i.e. Body-fitted methods and non-body fitted methods. In the body fitted methods, grid is fitted according to the flow boundaries. As the boundaries move, remeshing needs to be done so that new grid also fits the flow boundaries. In the non-body fitted methods, single stationary grid is used for all the phases as shown in fig. 1.4. Geometry being studied is 'immersed' in the discretized volume. A virtual boundary is created in place of the actual flow boundary using different techniques namely stair-step technique, SLIC (Simple line interface calculation) and PLIC (Piecewise linear interface calculation). This virtual boundary is many times also called as Immersed Boundary. Most of the fluid related applications deal with time dependent geometries. Body fitted methods are computationally very expensive in these cases because new grid needs to be generated at each time step. Also flow field from previous mesh needs to be mapped to the new mesh at each time step which makes overall process of problem solving very slow. In the non-body fitted methods, a single mesh occupying the entire calculation domain is built. In this case mesh doesn't conform to the flow boundaries. Arbitrary Lagrangian-Eulerian (ALE) finite element technique is most widely used method to solve CFD problem using body fitted grid which is explained below. Depending upon the cou-

pling of solid and fluid equations, non-body fitted DNS methods can be further categorized into following methods: Direct forcing IBM (Direct forcing Immersed Body method), DLM-FD (Distributed Lagrange Multiplier/Fictious Domain), CGM (Cartesian Grid Method), Lattice Boltzmann method (LBM). To track the interface due to phase change, use of Stefan boundary condition [13] is the most popular.

Hu et al. [14] modeled a two-dimensional unsteady solid-liquid two-phase flow using the body fitted DNS approach. Specifically, he modeled sedimenting flow of upto 4 cylinders in a channel. Particle motion was solved separately with Newton's equation. Motion of particles and fluid flow was coupled via hydrodynamic forces and moment and boundary conditions on the particle surfaces. Simplest fully explicit scheme for Newton's equation was found to be unstable. To correct this instability, they proposed explicit-implicit scheme in which at each time step, positions of particles were updated explicitly, computational domain is remeshed, solution at previous time is mapped onto new mesh and finally nonlinear NS equation and implicit discretized Newton's equation for particle velocities are solved on new mesh iteratively. Three major challenges in this numerical technique was first, generation of new mesh at each time step according to the position of particles, second, mapping of flow field at previous time step to the new mesh and third, numerical scheme that discretizes the coupled NS equation and particle equation has to be stable and efficient. The numerical model could be improved in many ways, like a more accurate scheme (second order error accuracy of time derivative terms).

Meanwhile, Hesla [15] combined fluid and particle motion equations into a single weak equation called the combined equation of motion, or total momentum equation. It eliminates the hydrodynamic forces and torque terms from the numerical scheme. Modifying the method provided by Hu et al. [14], Hu [16] used the combined formulation provided by Hesla [15] The new numerical model developed was named "Arbitrary Lagrangian-Eulerian (ALE) moving mesh technique".

The first popular DNS model for phase changing particulate flow system was provided by Gan et al. [17]. Gan et al. [17] modeled the sedimentation of melting solid particles in a hot Newtonian fluid of Prandtl number = 0.7 using Arbitrary Lagrangian-Eulerian (ALE) scheme. Both the phases were made of the same material. Motion of particles and fluid flow was coupled via hydrodynamic force and moment and boundary conditions on the particle surfaces. It was shown that sedimentation of melting particles depends strongly on the upward flow of the warm bulk fluid and downward flow of cold melt.

Yu et al. [18] used the non-body fitted DNS method to study the heat transfer in particulate flows. Distributed Lagrange Multiplier/Fictious Domain (DLM/FD)

method was used to track the interface. The fluid-flow equations were solved with the finite-difference projection method on a half-staggered grid. It is shown that DLM/FD method is reliable and efficient for the heat transfer problem in complex geometries and also usable for particulate flows where heat conduction inside the moving particles and thermal convection in fluids are coupled.

Feng and Michaelides [19] modeled momentum and heat interactions in particulate flows using a non-body fitted DNS model and Immersed Boundary Method (IBM) to track the interface. Modified momentum and energy equations was solved for the entire flow regime with the use of regular staggered Eulerian grid. In the region occupied by particles, second particle-based moving Lagrangian grid was used to track particles. No-slip boundary condition on the particle surface and rigid body motion of particles are enforced only in Lagrangian grid. A force density function and a energy density function are introduced to represent the momentum interaction and thermal interaction between particle and fluid.

Dan and Wachs [20] used a 2D non-body fitted DNS model to solve the heat transfer in non-isothermal particulate flow. Discrete Element Method (DEM) is used to compute the motion of particles. Heat transfer equation was solved in each particle using Finite Element Method (FEM) to calculate the temperature distribution inside the particles. DLM/FD method was used for coupling between fluid and particles unknowns. For each particle, a single FEM grid was generated which is rotated and translated at each time step to match the physical configuration of each particle.

Dierich et al. [21] carried out the numerical simulations for particulate flow with phase change. Two different cases of phase change process were modeled. In first case, single cylindrical ice particle held in a free stream of water was undergoing phase change due to convection. In second case, multiple cylindrical ice particles rising up in the water due to buoyancy were melting because of forced convection. 2D non-body fitted DNS was performed in both the cases. A fixed Euler grid was used to model the entire fluid flow. Particles motion was modeled using Lagrangian approach. Hydrodynamic forces were calculated using surface integrals without use of supplementary correlations. Interface velocity was modeled using Stefan boundary condition [13] for each particle. Optimal Nu-based zero dimensional model was provided at the end to predict the numerical results obtained by simulations.

Unresolved Discrete Particle Model (UDPM)

Since complete kinematics around each solid body is fully resolved, DNS models don't require any closure laws to relate the momentum, mass, heat and species

transport between solid particles and fluid. However, these models are computationally very expensive which limits the number of particles which these models can solve. This problem can be overcome by the use of second category of Euler-Lagrange models known as Unresolved Discrete Particle Model (UDPM).

Applied to the industrial multiphase flow, it is impractical to fully resolve all the scales and one must rely on the equations describing average flow or large scale flows. In UDPM models, the Eulerian grid is at least an order of magnitude larger than the particle size. Particles are tracked using separate moving Lagrangian grid and fluid equations are solved using a fixed Eulerian grid. The particle-particle interaction in these models is modeled in two ways: hard sphere and soft sphere model. Soft sphere model can handle large number of particles thereby becoming the popular choice. This category of Euler-Lagrange models is also called coupled DEM-CFD models because particle equations are solved using Discrete Element Models (DEMs) and fluid equations are solved using typical conservations equations for momentum, heat and mass in fixed Eulerian grid.

One of the limitations of this class of models is the requirement of so-called subgrid model equations or closure laws which describe the transport of momentum, heat, mass and species between the particles and fluid. For e.g., Gas-solid drag relations for momentum transfer, Stefan conditions between phase changing particles and fluid, etc.. Compared to DNS models, these models are computationally less expensive but requires larger modeling effort (in order to develop the constitutive relations). Most of the computational time in these models is spent in detecting the contact of particles. There are several different methods in literature to efficiently detect the contact of particles namely Direct simulation Monte Carlo (DSMC) method, Multiphase particle in-cell (MPPIC) method [22] . MPPIC uses the part of both, Euler-Euler models and Euler-Lagrange models, mapping the particle properties from Lagrangian coordinates to Eulerian grid.

Euler-Euler models, as described earlier, treat solid particles as a continuum like liquids and gases. So, these models don't need to detect the collision between the particles. This makes these models computationally cheaper than UDPM models but at the same time, required modeling effort increases in Euler-Euler models. Many complex constitutive equations need to be developed in EE models in order to close the system of equations. These constitutive relations often lack the physical background due to which these models often fail to describe the experimental results.

DNS models which essentially represent the exact solution of the numerical system being modeled, can be used to define these subgrid model equations that can be further used to represent the interactions between particle and fluid in a coarse grid

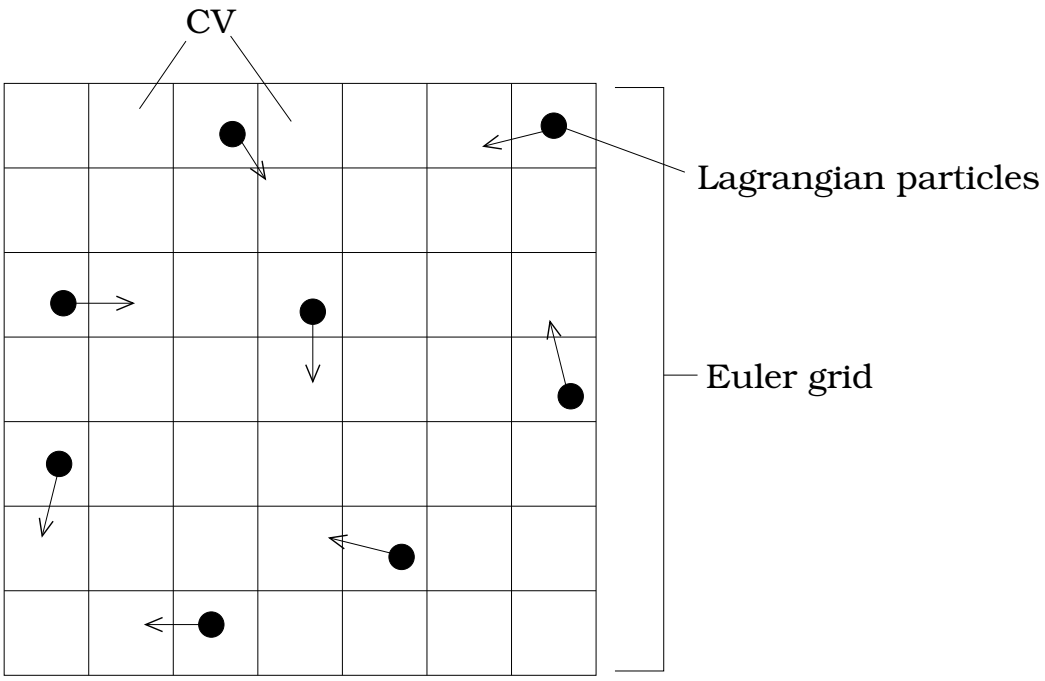

Figure 1.4: Grid in Unresolved Discrete Particle Model (UDPM)

formulation like UDPM. This work is devoted to the development and validation of the subgrid models or closure laws required in UDPM models describing heat transfer between the bulk flow and moving particles undergoing phase change under the influence of forced and free convection. These subgrid models depend upon the basic dimensionless numbers like Reynolds number, Stefan number, Prandtl number etc. as shown in fig. 1.5. These models serve as a coupling between equations describing particle motion in Lagrangian space and equations defining melt flow in Eulerian space. In order to obtain these subgrid models, DNS models can be used to understand the physics and then accurate subgrid models can be developed. However, in spite of numerous works devoted to the DNS modeling of isothermal particulate flows, there are few works concentrating on modeling phase change processes in solid-liquid two-phase flows. Gan et al. [17] and Dierich et al. [21] used DNS modeling to describe the particulate flow with phase change but number of particles were limited. Euler-Lagrange models have a great capability to model the convection-driven solidification of a multicomponent alloy due to their more natural multi-scale character and flexibility regarding grid resolution in comparison to Euler-Euler based approached. Euler-Euler models have to use coarse grid (of the order of 1 meter) so that statistically reliable volume average of each variable can be written in each grid cell. Euler-Euler models are suitable for highly dense systems

i.e. systems having high volume fraction of dispersed solid particles.

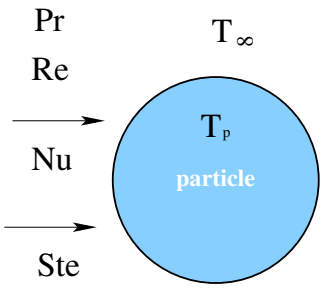

Figure 1.5: Principle scheme of a moving particle and basic input parameters for semi-empirical models for heat and mass transport between particle and fluid. Typical size of a particle is > 100 μm.

1.3 Objectives

The long term objectives of this study are to contribute to the significant improvement of computational software used for multiphase process optimization; to develop and validate a new Euler-Lagrangian model describing complex interactions between equiaxed dendrites and the melt during solidification; to obtain better understanding of the behavior of phase-change phenomena in particulate flows. The short term objectives are to develop subgrid models describing the interfacial heat transfer between moving particles undergoing phase change and the bulk flow.

Chapter 2

Semi empirical model for particles undergoing phase change: Two phase model[1]

This chapter is devoted to the development and validation of a subgrid model (also known as submodels and semi-empirical models) describing heat transfer between the bulk flow and moving particles undergoing phase change under the influence of forced and free convection. Such kind of submodels plays the role of *"scale bridges"* between microscale (e.g., interfacial heat transfer) and macroscale (e.g., bulk flow) phenomena. Applied to multiscale modeling of particulate flows with phase change phenomena, our model serves as a coupling between equations describing particle movement in Lagrangian space and the mass and heat conservation equation defining melt flow in Eulerian space. The input parameters in our model are the particulate Reynolds number (Re), the Grashof number (Gr), the Stefan number (Ste) and the Prandtl number (Pr). These models are called subgrid models because they are applied to the particles having much smaller size than the cell size of grid. The model is validated against experimental data published recently in the literature applied to the melting of ice spheres under different flow conditions. Good agreement between our model predictions and published experimental data (A. Shukla et al. Metal. Mater. Trans. B, 42B, 2011 and Y. Hao & Y. Tao. J. Heat Transfer, 124, 2002.) was observed.

[1]based on a manuscript "A Submodel for Spherical Particles Undergoing Phase Change Under the Influence of Convection" accepted for publication in Can. J. Chem. Engg.

2.1 Introduction

During the last thirty years, the modeling of solidification of metals and alloys has made significant progress using novel numerical methods and algorithms, finally becoming a quantitative engineering science [23]. One of the crucial parts in so-called multiphase models describing phase change phenomena is a scale bridge between heat, mass and fluid flow in the bulk phase and interfacial heat and mass transfer. One of the widely used multiphase approaches corresponds to the so-called Euler-Euler models: see the pioneering works by Wang & Beckermann [24, 25, 26] and later by Wu & Ludwig [27, 28]. The Euler-Euler models use volume-averaged mass, momentum, energy and species conservation equations written for each phase in Eulerian space. Additional source terms in each conservation equation are responsible for the mass, momentum, energy and species concentration exchange between the phases, which are often based on heuristic models. Despite considerable progress in the multiscale modeling of solidification using Euler-Euler models, (e.g., see the works [27, 28]), existing models are very often not capable of predicting solidification phenomena relating to the moving equiaxed crystals (particles). In light of this, the Euler-Lagrange-based models can be used as an alternative approach for adequately forecasting multiscale solidification/melting processes with free-floating dendrites. In this approach, the motion of the solid particles is treated individually using Newton's law of motion. To model heat and mass transfer between the particles and fluid, subgrid equations (submodels) are used if the size of a particle is less than the cell of a numerical grid used for calculation of conservation equation in Eulerian space. To overcome the problem of subgrid models, the so-called *resolved* discrete particle model (RDPM) or particle-resolved direct numerical modeling (PR-DNS) can be used [29, 30] when the cell of a numerical grid is less than the particle size. However, applied to particulate flows where phase change phenomena plays significant effect, PR-DNSs are still computationally expensive tools used to understand the physics and at the same time to develop more accurate subgrid models [31, 32]. In this view, experimental studies on particulate flows with complex "interfacial-physics" are non-avoidable instruments of obtaining a basic understanding of particles melting under different flow conditions, (e.g., see the works [33, 34, 35, 3, 36, 2]).

Nevertheless, recent significant progress in modeling of dense particulate flows, (e.g., fluidized-bed systems) has been achieved using the Euler-Lagrange-based models coupled with discrete element models (DEM) originally introduced by Cundall and Strack [37], see reviews [38, 39]. However, applied to the modeling of phase

change phenomena (e.g., dendritic solidification), one of the limitations of this class of models is the lack of subgrid equations (submodels) to predict interfacial heat and mass transfer between the particles and fluid for different flow conditions (e.g., see the review [40]). To overcome this gap, the main objectives of this work are to develop subgrid models describing the interfacial heat and mass transfer between a moving particle and the bulk flow undergoing phase change. For the validation of our model, two cases are considered: The first case corresponds to the melting of ice particles under the influence of natural convection only, and the second case corresponds to the melting of ice particles under the influence of mixed conditions comprised of forced flow and natural convection. Finally, we validate the model against experimental data published in the literature [3, 2].

2.2 Phase change of single particle in the fluid of same material

In this section, we develop the required submodel equations to describe the heat transfer between bulk flow and moving particles undergoing phase change under the influence of convection. To illustrate the derivation of our model, we consider two different cases: spherical and cylindrical ice particle moving in a bulk flow of water. Water temperature is above the melting point of ice thereby causing the melting of ice particle. In this melting process, driven by the temperature difference, heat energy flows from bulk water to inside the ice particle via these two heat transfer processes:

- Convective heat transfer between particle surface and bulk water.
- Conductive heat transfer inside the ice particle.

As the ice particle gets heated, it begins to melt as soon as its surface temperature reaches the melting point. The following subsections will provide the submodel equations to predict the size of spherical and cylindrical ice particle in this melting process.

2.2.1 Model Formulation for spherical particle

The required equation to find the radius of spherical particle in the considered melting process can be obtained by applying well-known Stefan boundary condition at ice-water interface [13]. Consider the spherical ice particle as shown in fig. 2.1.

The application of Stefan boundary condition at ice-water yields following equation:

$$\begin{aligned}\rho_p h_{sf} u^* &= q_l^{''} - q_p^{''} \\ &= \left(k_p \frac{\partial T_p}{\partial x}\right)|_{solid} - \left(k_l \frac{\partial T_l}{\partial x}\right)|_{liquid}\end{aligned} \tag{2.1}$$

where u^* is local interface velocity, $q_l^{''}$ and $q_p^{''}$ are heat fluxes on liquid side and particle side respectively. Applied to a spherical particle undergoing the phase change, this equation can be integrated over the particle surface and re-written as follows:

$$\rho_p h_{sf} \frac{4}{3}\pi \frac{dr_p^3}{dt} = q_l - q_p \tag{2.2}$$

where r_p represents the volume average radius of the particle. The heat rates in the liquid and solid sides can be formulated as follows:

$$q_l = 4\pi r_p^2 h(T_m - T_\infty) \tag{2.3}$$

$$q_p = \frac{4\pi k_p (T_p - T_m) r_t r_p}{r_p - r_t} \tag{2.4}$$

where T_p is the average temperature of the ice sphere corresponding to the temperature at the distance r_t ($= 0.5^{1/3} r_p$) from the center [41]. To calculate particle temperature we use following heat balance equation:

$$\rho_p v_p c_p \frac{dT_p}{dt} = \frac{4\pi k_p (T_m - T_p) r_t r_p}{r_p - r_t} \tag{2.5}$$

Inserting the convective heat transfer coefficient $h = \frac{Nu_{d_p} k_\infty}{d_p}$ into the eq. 2.3 and substituting this equation into eq. 2.2 reveals final equation for the evolution of the particle radius:

$$\rho_p h_{sf} \frac{dr_p}{dt} = \frac{Nu_{d_p} k_\infty}{2r_p}(T_m - T_\infty) + \frac{k_p (T_m - T_p) r_t}{r_p (r_p - r_t)} \tag{2.6}$$

Finally, Eq. 2.5 and Eq. 2.6 can be used to predict solidification/melting of a moving spherical particle. Correlation for Nusselt number in eq. 2.6 depends upon the nature of convective heat transfer which is governed by the flow regime around the ice sphere. It should be noted that if initial particle temperature T_p is equal to

the melting temperature T_m, Eq. 2.6 reduces to:

$$\rho_p h_{sf} \frac{dr_p}{dt} = \frac{Nu_{d_p} k_\infty}{2r_p}(T_m - T_\infty)$$

This equation can be easily transformed into the following form:

$$\frac{dr_p^2}{dt} = \frac{Nu_{d_p} k_\infty}{\rho_p h_{sf}}(T_m - T_\infty) = -Nu_{d_p} \cdot Ph \cdot \alpha_l. \tag{2.7}$$

where $\alpha_l = \frac{k_\infty}{\rho_l c_{p,l}}$ is the thermal diffusivity of the liquid phase and Ph is the Phase change number calculated as follows:

$$Ph = \frac{\rho_l}{\rho_p} Ste_l$$

where Ste_l is the Stefan number for the liquid phase given by:

$$Ste = \frac{c_{p,l}(T_m - T_\infty)}{h_{sf}}$$

The Eq. 2.7 is termed as 'one temperature model' since temperature of ice particle is assumed to be equal to 0^o C and the only temperature value required to solve this equation is ambient fluid temperature, T_∞. Eqs. 2.5 and 2.6 collectively are termed as 'Two temperature model' since two temperature values, T_p and T_∞, needs to be known to solve these two equations simultaneously.

Depending upon the flow of water around the ice particle, convective heat transfer between particle surface and water can be forced, free or mixed [1]. The term $\frac{Gr_{d_p}}{Re_{d_p}^2}$ defines the type of convective heat transfer. In particular, according to classical heat transfer theory [1], three regimes can be distinguished according to the following values of $\frac{Gr_{d_p}}{Re_{d_p}^2}$:

- If $\frac{Gr_{d_p}}{Re_{d_p}^2} >> 1$, free convection dominated flow regime.
- If $\frac{Gr_{d_p}}{Re_{d_p}^2} < 10^{-2}$, forced convection dominated flow regime.
- Otherwise, mixed convection dominated flow regime

Next, we introduce classical Nu-relations for the heat transfer between a sphere and fluid flow under under different flow regimes:

Forced Convection: Here, the Nusselt number correlation known as Ranz-Marshall

relation [42] can be used as follows:

$$Nu_{d_p} = 2 + 0.6 Pr_{\infty}^{1/3} Re_{d_p}^{1/2} \tag{2.8}$$

where Re_{d_p}, Reynolds number is give by:

$$Re_{d_p} = \frac{\rho_{\infty} |u_p - u_{\infty}| d_p}{\mu_{\infty}} \tag{2.9}$$

Free Convection: The following correlation provided by Churchill [43] can be used and is valid when $Pr_{\infty} \geq 0.7$, $Ra_{d_p} \leq 10^{11}$

$$Nu_{d_p} = 2 + \frac{0.59 Ra_{d_p}^{0.25}}{(1 + \frac{0.469}{Pr_{\infty}}^{\frac{9}{16}})^{4/9}} \tag{2.10}$$

where Ra_{d_p}, Rayleigh number is given by:

$$Ra_{d_p} = \frac{g \beta_{\infty} (T_{\infty} - T_m) d_p^3}{\alpha_{\infty} \nu_{\infty}} \tag{2.11}$$

Mixed Convection: Here, Nusselt number is given by [1]:

$$Nu_{mixed}^n = Nu_{forced}^n \pm Nu_{free}^n, n \approx 3 \tag{2.12}$$

where "+" or "-" depends on the direction of forced flow relative to the natural convection driven flow. The plus sign is used for *assisting* (buoyancy-induced and forced motions have the same direction) and *transverse* (buoyancy-induced and forced motions have perpendicular directions) flows whereas the minus sign is used for opposing flows [1]. It should be noted that according to the book [1] *'...the best correlation of data is often obtained for $n = 3$, although values of 7/2 and 4 may be better suited for transverse flows involving horizontal plates and cylinders (or spheres), respectively'.*

Now our submodel for spherical particle is closed and can be validated against the experimental results published in literature.

2.2.2 Model formulation for cylindrical particle

Similar approach can be followed to derive the equation for prediction of size of cylindrical ice particle with axis in the vertical direction i.e. along the gravity. Writing Stefan Boundary condition [13] eq. 2.1 at ice-water interface and then

taking surface integral, we get

$$\rho_p h_{sf} \frac{dv_p}{dt} = q_l - q_p$$

Above equation can be split into two different equations to predict the height and radius of cylinder by using the appropriate forms of q_l and q_p. The equation to calculate height, l_p can be written as

$$\rho_p h_{sf} \pi r_p^2 \frac{dl_p}{dt} = h_t \pi r_p^2 (T_m - T_\infty) + h_b \pi r_p^2 (T_m - T_\infty) - \frac{2k_p \pi r_p^2 (T_p - T_m)}{l_p - l_t}$$

where l_p is the length of particle, h_t and h_b are the heat transfer coefficients on the top and bottom surface of cylinder respectively, T_p is the average temperature of the particle. Similarly, the equation to calculate the radius, r_p can be written as

$$\rho_p h_{sf} \pi l_p \frac{dr_p^2}{dt} = h_s 2\pi l_p r_p (T_m - T_\infty) - \frac{2\pi k_p l_p (T_p - T_m)}{ln(r_p/r_t)}$$

where h_s is the heat transfer coefficient on the side curved surface of cylinder. The average temperature T_p exists at distance r_t and l_t from the center. Similar to the case of spherical particle, $r_t = 0.5^{1/3} r_p$ and $l_t = 0.5^{1/3} l_p$ [41]. The previous two equations can be re-written as follows

$$\rho_p h_{sf} \frac{dl_p}{dt} = (h_t + h_b)(T_m - T_\infty) + \frac{2k_p (T_m - T_p)}{l_p - l_t} \tag{2.13}$$

$$\rho_p h_{sf} \frac{dr_p^2}{dt} = 2h_s r_p (T_m - T_\infty) + \frac{2k_p (T_m - T_p)}{ln(r_p/r_t)} \tag{2.14}$$

The average particle temperature, T_p can be calculated using following heat balance equation on particle:

$$\rho_p v_p c_p \frac{dT_p}{dt} = \frac{2k_p \pi r_p^2 (T_m - T_p)}{l_p - l_t} + \frac{2\pi k_p l_p (T_m - T_p)}{ln(r_p/r_t)} \tag{2.15}$$

where left hand side term represents the rate at which heat energy is stored in particle and right hand side represents the rate at which the heat energy is entering the particle at solid-liquid interface.

For cylindrical ice particle, three different Nusselt number correlations have to be used; each for three different surfaces. For instance, following correlations can be used for the case of free convection:

For side surface: Correlation for "vertical flat plate" can be used given that

the thermal boundary layer thickness is less than the diameter of cylinder. This condition translates to [1]:

$$\frac{d_p}{l_p} \geq \frac{35}{Gr_{l_p}^{3/4}} \tag{2.16}$$

$$Nu_{l_p} = 0.68 + \frac{0.67Ra_{l_p}^{1/4}}{\left[1 + \left(\frac{0.492}{Pr}\right)^{9/16}\right]^{4/9}} \tag{2.17a}$$

For top surface: $$Nu_{d_p/4} = 0.27Ra_{d_p/4}^{1/4} \tag{2.17b}$$

For bottom surface: $$Nu_{d_p/4} = 0.15Ra_{d_p/4}^{1/3} \tag{2.17c}$$

The submodel for cylindrical particle is closed now and can be validated against experimental results. Collectively, eqs. 2.13, 2.14, 2.15 coupled with appropriate Nusselt number correlations constitute the submodel.

2.3 Model validation

The submodel equations are validated against different experimental data published in the literature. The submodel for ice sphere is validated for the case of natural convection, mixed convection and forced convection flow regimes where the submodel for ice cylinder is validated for natural convection flow regime. The physical properties of water at different temperatures used in the validation process are summarized in Table 2.1. Latent heat of fusion of ice was considered to be ≈334 kJ/kg [1].

2.3.1 Free convection

Shukla et al. [2] carried out series of experiments in which spherical and cylindrical ice particle was submerged and held in a particular position inside a cylindrical vessel. The cylindrical vessel wad made of some transparent material and was filled with water. Argon gas was introduced from the bottom of vessel through small openings. The original idea of the experiments was to study the impact of the resulting bubble flow on the melting dynamics of ice-made spheres and cylinders under different ambient water temperatures. We will consider only those results in which there was no introduction of argon gas into the water, thereby resulting in quiescent water and making this a case of free convection melting of the ice particle. Using a high-speed camera and planar laser-induced fluorescence technique, the

Table 2.1: Thermophysical properties [1] of water and ice at different temperatures used during validation of the model.

T (K)	ρ (kg/m^3)	c $(J/kg.K)$	k $(W/m.K)$	Pr	β $(10^{-6}K^{-1})$	μ $(10^{-6}N.s/m^2)$
Water						
281.15	1000.00	4195.93	0.58384	9.9265	61.694	1376.69
283.15	1000.00	4192.33	0.58704	9.3465	88.917	1297.89
284.15	1000.00	4190.53	0.58864	9.0565	102.5298	1258.49
286.15	999.77	4187.85	0.59184	8.5225	127.877	1191.65
289.15	999.17	4184.85	0.59664	7.7725	163.817	1104.65
293.15	998.37	4182.11	0.60340	6.9678	207.705	1003.77
294.15	998.17	4181.51	0.60464	6.7798	218.405	979.57
299.15	997.18	4179.34	0.61181	5.9643	267.838	872.68
303.15	995.76	4178.37	0.61741	5.4331	304.135	800.82
333.15	983.03	4185.26	0.65378	2.9799	523.845	466.32
Ice						
273.15	920	2040	1.88	–	–	–

thickness of the ice particle was measured in all of the experiments. Principle scheme of the experiments is shown in Fig.2.1.

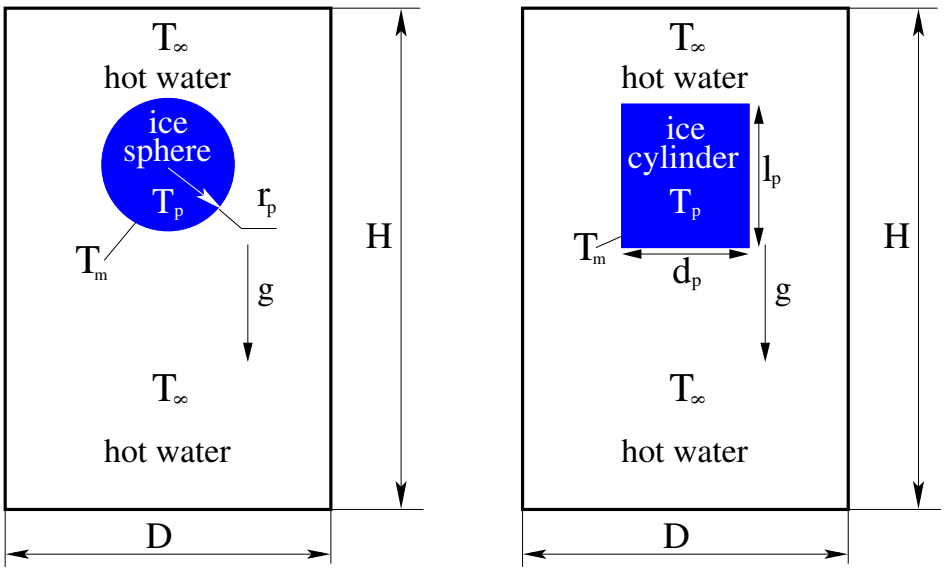

Figure 2.1: Principle scheme of experiments for melting of ice particle conducted by Shukla et al. [2]

Table 2.2 shows the various conditions in which experiments were carried out. Axial length of cylinder in all the cases was 0.05 m. Rayleigh number in the table

indicates whether the flow in thermal boundary layer is laminar or turbulent. Water height (H) in the vessel and its diameter (D) were 0.5 m and 0.445 m, respectively. It should be noted that authors did not provide the exact temperature of ice spheres used in experiments. Instead different values of the ice's initial temperature were used in our simulations.

Table 2.2: Ice sample and water properties in different experiments as conducted by Shukla et al. [2]

Ice shape	Diameter, d_p (m)	Water temp., T_∞ (^oC)	Rayleigh number
Sphere	0.073	20	$3.74 \cdot 10^7$
Sphere	0.075	60	$6.33 \cdot 10^8$
Cylinder	0.080	20	$1.20 \cdot 10^7$

Fig. 2.2 depicts the time history of ice sphere's radius predicted by solving Eqs. 2.5, 2.6 and 2.10 using an Euler explicit-based method. A time step of 0.01 seconds was used in calculations. Lower values of Δt produced similar results. Due to the fact that our submodel is 0D-model, which does not require any spatial coordinates, a grid study is not necessary. Since no information was given regarding the temperature of the ice particle in the experiments [2], we solved the submodel by assuming different initial values of the particle's temperature T_p^o. The ambient T_∞ was $20\,^oC$. Before we analyze the model performances, it should be emphasized that many physical properties of water involved in the formulation of the submodel (e.g., thermal expansion coefficient β, molecular viscosity μ_∞ and the Prandtl number Pr) are strong functions of the temperature. Due to natural convection, the temperature in the boundary layer around the ice particle varies from melting temperature, 273 K, to bulk temperature, 293 K. To maintain the simplicity of the submodel, a single constant temperature value of the boundary layer should be used as a reference temperature (T_{ref}) for water properties. The most obvious choice for T_{ref} is an average of bulk and melting temperature (referred as *film temperature*). Alternatively, we also considered *bulk temperature* T_∞ as the reference temperature to compare the results against experimental data [2]. Initial values of Ra numbers based on the *film* and *bulk* temperatures are $3.73 \cdot 10^7$ and $1.09 \cdot 10^8$, respectively. An analysis of fig. 2.2 shows a significant impact of T_{ref} on the time history of the ice-sphere radius. In particular, the use of the *film temperature* as a reference gives better agreement with experimental measurements in comparison to the *bulk temperature* case. From the figure, it can be seen that the impact of the initial ice sphere temperature T_p^o value (-10 ^{0}C, -5 ^{0}C, 0 ^{0}C) is insignificant in comparison to the influence of T_{ref} value.

To illustrate the model performances for $T_\infty = 60\,^oC$ corresponding to $Ra_{film} = 6.33 \cdot 10^8$, fig. 2.3 plots the time history of r_p calculated using the submodel with transport properties referring to the film temperature. The comparison with experimental data reveals good agreement at the beginning of melting and increasing deviation after 40 s. We explain this deviation by the significant impact of turbulent flow caused by the natural convection on the melting regime. In particular, the shape of the particle does not remain spherical due to turbulent jets in the bottom part of the particle, (e.g., see experimental work [34]). This turbulent flow causes faster melting of the sphere in the bottom region in comparison to the top region of sphere. Since horizontal maximum dimension of the ice particle was measured as the radius of the particle in the experiments, submodel results in this case are expected not to match with the experimental results. In the submodel, the sphere-equivalent radius of the particle is calculated, which would decrease at a faster rate compared to the experimental radius, which can also be seen in the results plotted in fig. 2.3. It should be noted that the use of different Nu-relations for a sphere did not produce better agreement with experiments than results predicted by the use of eq. 2.10.

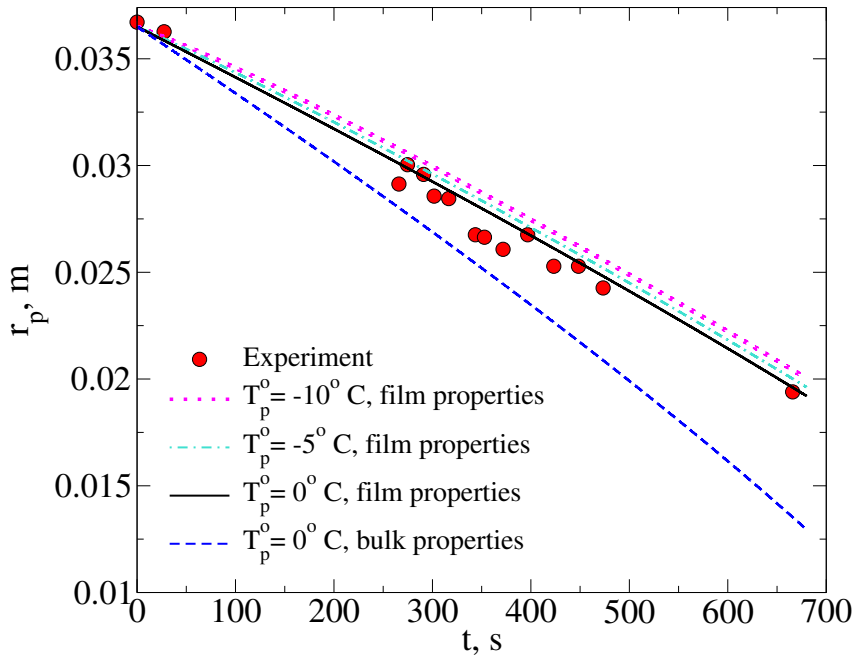

Figure 2.2: Time history of the radius of spherical ice particle as it melts due to natural convection with ambient water temperature T_∞ of $20\,^oC$. Experimental data correspond to the work [2]. Initial values of Ra numbers based on the film and bulk temperatures are $3.74 \cdot 10^7$ and $1.09 \cdot 10^8$, respectively.

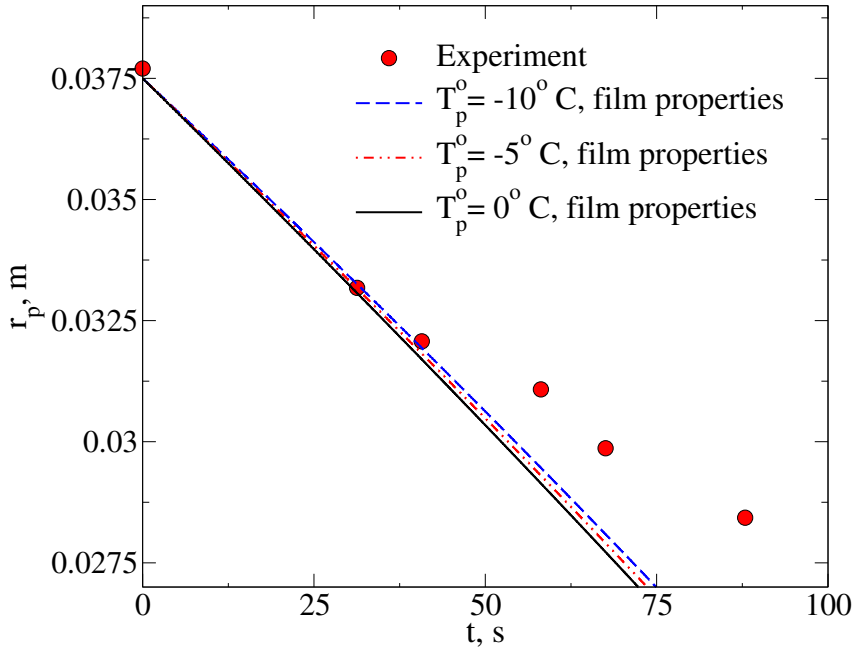

Figure 2.3: Time history of the radius of spherical ice particle as it melts due to natural convection with ambient water temperature T_∞ of 60 ^oC. Experimental data correspond to the work [2]. Initial values of Ra numbers based on the film and bulk temperatures are $6.33 \cdot 10^8$ and $1.73 \cdot 10^9$, respectively.

Fig. 2.4 depicts the submodel result for cylindrical particle. The results were obtained by solving eqs. 2.13, 2.14, 2.15 and 2.17 using an Euler explicit-based method with time step of 0.01 seconds. Lower values of time steps produced the similar results. Since, no information about the initial ice temperature was given in the experiments [2], ice temperature was assumed to be -10^oC. It should be noted that the curves in fig. 2.4 starts from time = 77 seconds. Experimental results had an unexpected 'increase' in the cylinder radius at this time. This might happen due to some error while conducting experiments. As can be seen from figure, similar to the spherical particle, use of film temperature as reference gives better agreement with experimental results.

2.3.2 Mixed convection

To validate the model for a case of forced and mixed convection, we used a series of experiments carried out by Hao and Tao [3] to study the convective melting of ice sphere placed in horizontally flowing water. The principle scheme of the experiment is shown in Fig. 2.5. In particular, in the experimental setup, the water was circulated at the desired flow rate and temperature past the ice sphere through a

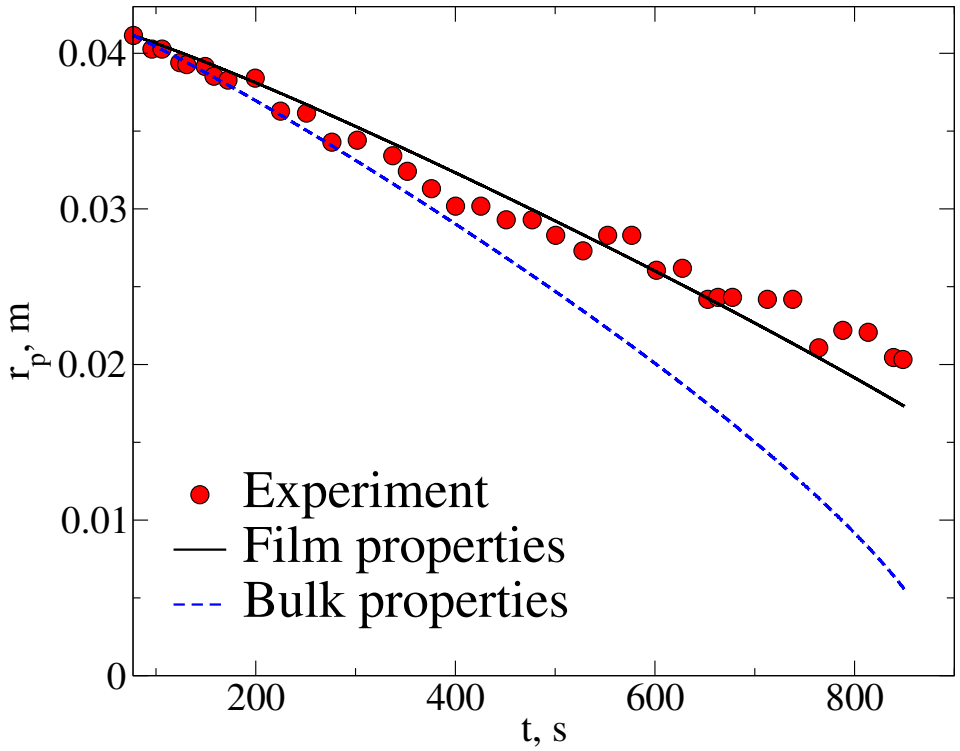

Figure 2.4: Time history of the radius of cylindrical ice particle as it melts due to natural convection with ambient water temperature T_∞ of $20\,^oC$. Experimental data correspond to the work [2]. Initial values of Ra numbers based on the film and bulk temperatures are $1.20 \cdot 10^7$ and $3.51 \cdot 10^7$, respectively.

horizontal open channel made of Plexiglas with dimensions of 500 x 152 x 216 mm. The sphere was fixed on a movable base through a plastic straw and was placed into the water flow in the channel. Water level was controlled in channel using an overflow plate placed at a downstream location. The temperature of the water in the channel was measured at various locations using thermocouples. The central temperature of the ice sphere was also measured by placing thermocouples inside it. A digital camcorder was used to record the images of the sphere as it melted. Each test was stopped when ice broke away from the base and drifted downstream with the water flow: for details, we refer to the original work [3]. Table 2.3 lists the various input parameters used in experiments [3] which we used to validate our model. In this validation test, we used the term $\frac{Gr}{Re^2}$, which characterizes the flow regime (forced, mixed or free convection) around the ice sphere (see section 2.2.1). Since experiments were carried out at wide span of temperatures and velocities, the term $\frac{Gr}{Re^2}$ took different values, which resulted in mixed convection and free convection in different cases. Here again, we used film and bulk temperature as

reference for calculation of water properties as described in section 2.3.1.

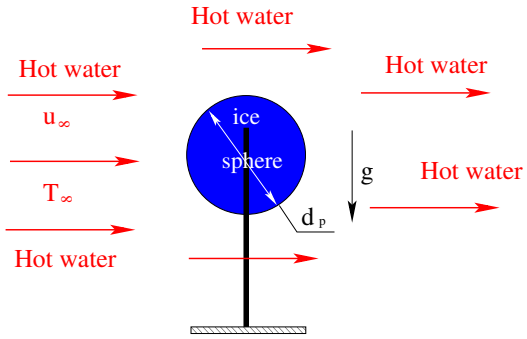

Figure 2.5: Principle scheme of experiments for melting of spherical ice particle conducted by Hao and Tao [3]

Table 2.3: Ice sample and water properties in different experiments as conducted by Hao and Tao [3]

Water temperature	11 C - 30 C
Water velocity	0.01 m/s - 0.06 m/s
Ice sphere temperature	-8 C, -16 C
Ice sphere diameter	36 mm

Before we proceed with a comprehensive validation of the model performances in terms of the forced and mixed convection, we illustrate the impact of the reference temperature choice (film or bulk) on the melting dynamics of the sphere. Fig. 2.6 depicts the time history of the ice sphere's diameter predicted using the submodel (lines) and experiments [3] (red circles) for the water temperature of 26 ^oC, water velocity of 0.06 m/s and ice temperature of -16 ^oC, which correspond to $Gr = 4.16 \cdot 10^6$, $Re = 2468.1$, $\frac{Gr}{Re^2} = 0.683$ if the film temperature is used as reference for water properties. As explained in section 2.2.1, this values of $\frac{Gr}{Re^2}$ entails that we have mixed convection dominated regime in this case. We found out that in the case of mixed and forced convection, the use of the bulk temperature instead of film temperature as a reference temperature to calculate transport properties of the water gives better agreement with experimental data. It can be seen in figure that use of bulk temperature provides better agreement with experimental data. On the other hand, film temperature proves to be better choice of reference temperature for the case of free convection dominated regime. Fig. 2.7 depicts the time history of the melting rate of an ice sphere predicted using the model (line) and measured [3] (circles) at the water velocity of 0.01 m/s and $T_p^o = -8\,^oC$, $T_\infty = +16\,^oC$, which refer to $\frac{Gr}{Re^2} = 9.25$. Thus, this is a case of free convection dominated regime and

use of film temperature as T_{ref} provides better agreement with experiments. It should be noted here that significant deviation between experimental data and our model predictions at the initial time can be attributed to the establishment of the boundary layer around the particle. Thus, we think that at the beginning of melting the reference temperature can differ from the film temperature we used. And the second possible reason of this deviation can be invalidity of the Nu relation we used during the start up phase at the initial time.

Table 2.4: Nondimensional numbers calculated for different water velocities according to the different experimental conditions of fig. 2.8 with use of bulk and film temperature as reference for water properties

Velocity (m/s)	Reference temperature	Ra	Gr	Re	Gr/Re^2
0.06	bulk	$7.6 \cdot 10^6$	$9.81 \cdot 10^5$	1953.75	0.2574
0.06	film	$2.36 \cdot 10^6$	$2.38 \cdot 10^5$	1568.98	0.0968
0.03	bulk	$7.6 \cdot 10^6$	$9.81 \cdot 10^5$	976.87	1.0282
0.03	film	$2.36 \cdot 10^6$	$2.38 \cdot 10^5$	784.49	0.3872
0.02	bulk	$7.6 \cdot 10^6$	$9.81 \cdot 10^5$	651.25	2.3134
0.02	film	$2.36 \cdot 10^6$	$2.38 \cdot 10^5$	522.99	0.8712

Fig. 2.8 shows the effect of water velocity on the melting rate of the ice sphere, keeping water temperature constant, for the *mixed convection regime*. Nondimensional numbers, Gr, Re, and $\frac{Gr}{Re^2}$ are given in Table 2.4, where nondimensional numbers are calculated using the bulk and film temperature. In particular, Fig. 2.8a shows comparisons between experimentally measured [3] (circles) and predicted (lines) melting rates using the bulk temperature, and Fig. 2.8b depicts the same melting rates predicted using the film temperature. It can be seen that better overall agreement between experimental and submodel results is obtained with the use of bulk temperature. The effect of changing water temperature while keeping water velocity constant can be seen in fig. 2.9. All different tests in this figure represent the mixed convection case, and therefore, bulk temperature is used as reference for water properties.

Finally, it should be noted that the analysis of fig. 2.8 and fig. 2.9 shows some significant deviation between experimental data and our model predictions at the initial time. We think that this effect can be caused by the fact that our model is not able to capture the establishment of the boundary layer around the particle. In particular, the Nu relations we used are not valid for the start up phase at the initial time.

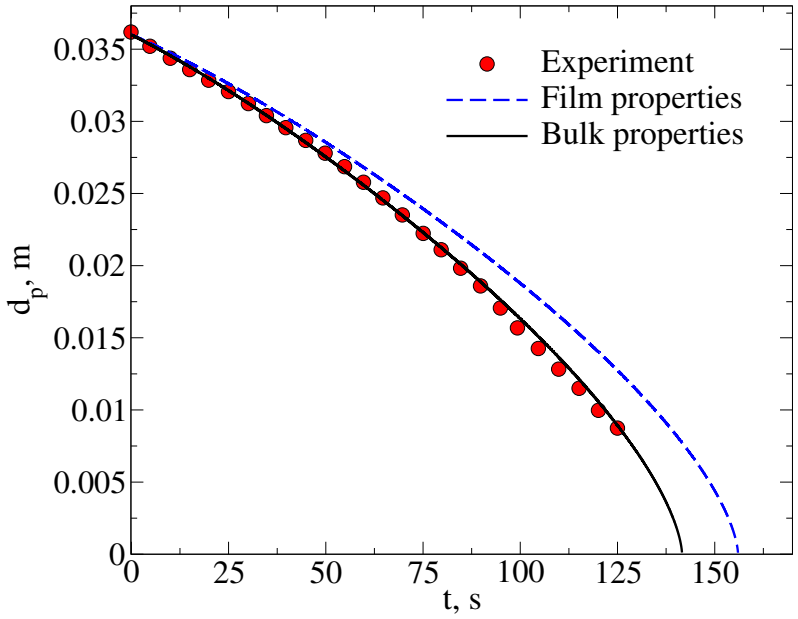

Figure 2.6: Time history of the diameter of spherical ice particle predicted using submodel and experiment [3] for $u_\infty = 0.06$ m/s, $T_p^o = -16^oC$, $T_\infty = +26^oC$. Initial values of the dimensionless numbers based on the film temperature are as follows: $Gr = 4.16 \cdot 10^6$, $Re = 2468.1$, $\frac{Gr}{Re^2} = 0.683$.

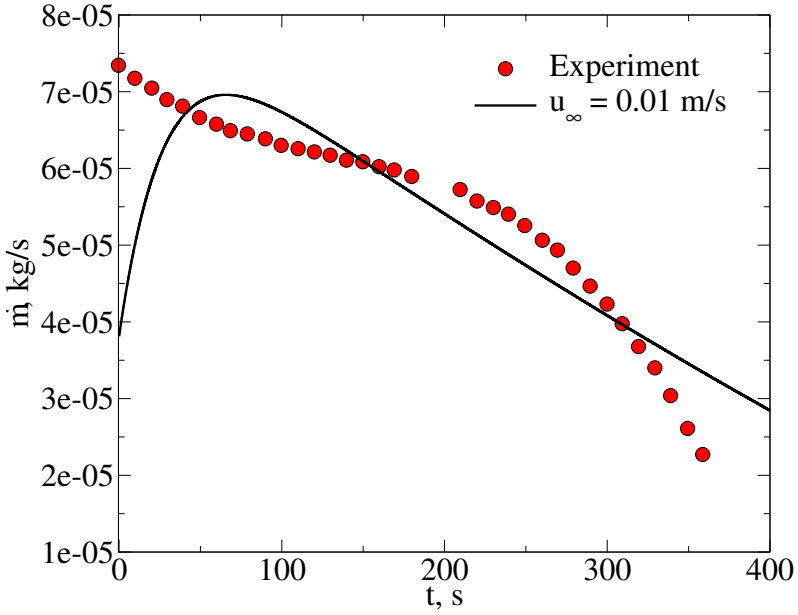

Figure 2.7: Time history of the melting rate of spherical ice particle predicted using submodel and experiment [3] for $u_\infty = 0.01$ m/s, $T_p^o = -8^oC$, $T_\infty = +16^oC$. Initial values of the dimensionless numbers based on the film temperature are as follows: $Gr = 9.81 \cdot 10^5$, $Re = 325.62$ and $\frac{Gr}{Re^2} = 9.25$.

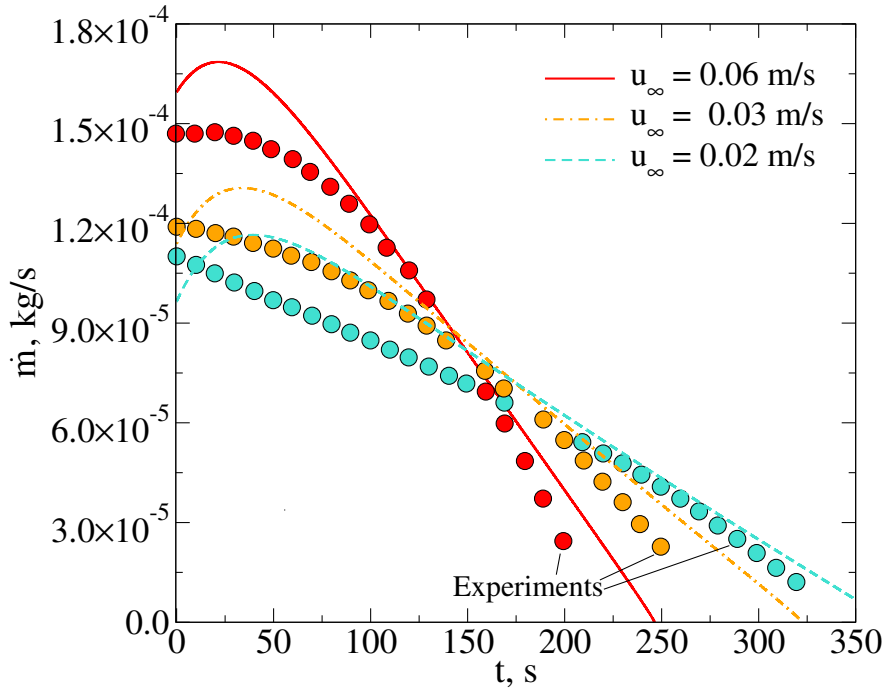

a

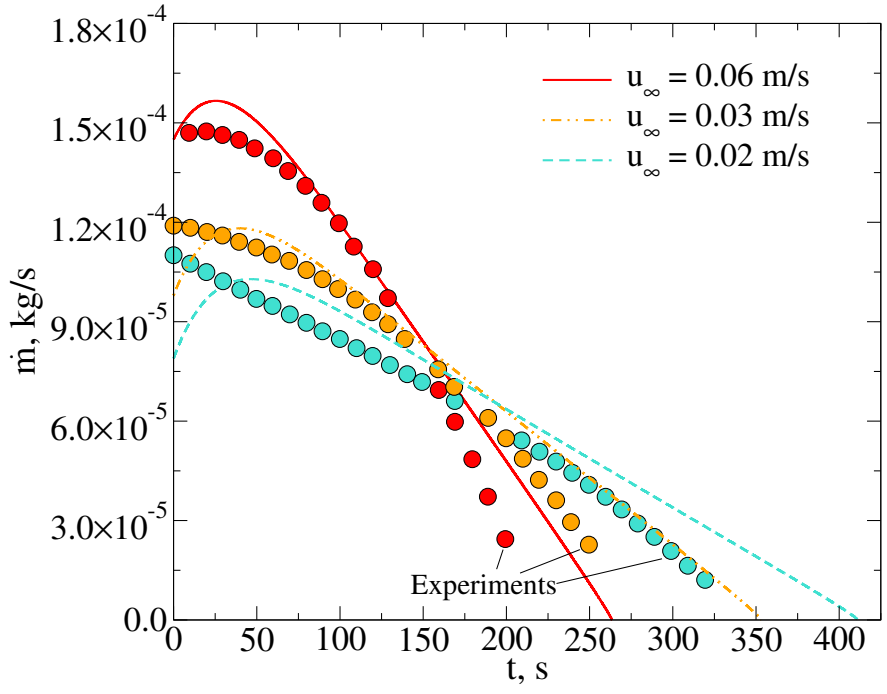

b

Figure 2.8: Time history of the melting rate of spherical ice particle measured using experiments [3] and calculated using submodel with T_{ref}: a) bulk temperature and b) film temperature at different water velocities (all corresponding to mixed convection): $T_p^o = -8^oC$, $T_\infty = +16^oC$, $\frac{Gr}{Re^2}$ range: $0.2574 \div 2.313$.

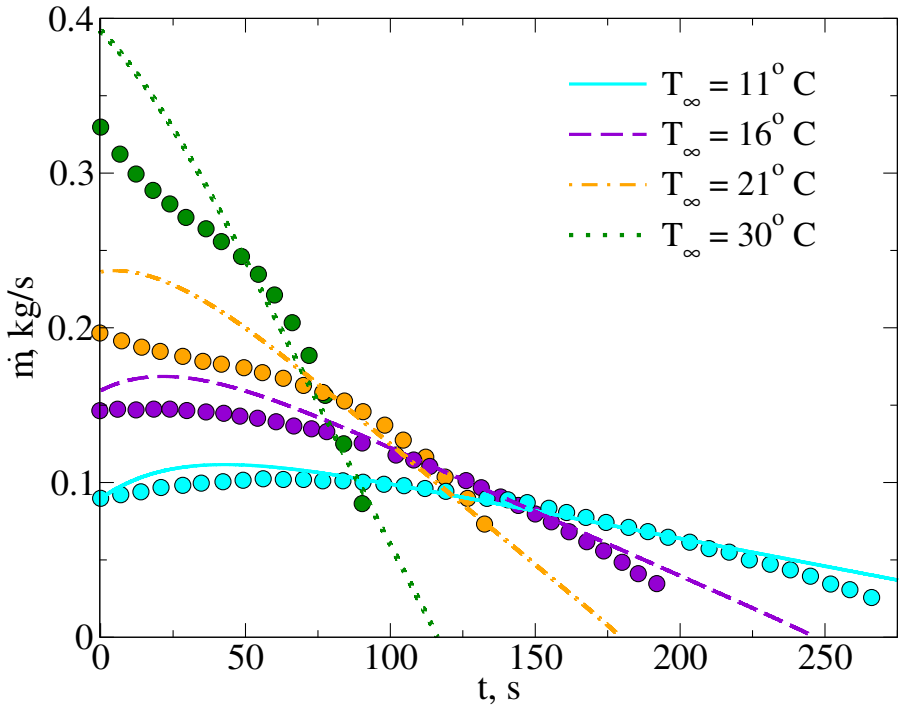

Figure 2.9: Time history of the melting rate of spherical ice particle measured using experiments [3] (circles) and calculated using submodel (lines) with T_{ref} as bulk temperature at different water temperatures (all corresponding to mixed convection): $u_\infty = 0.06$ m/s, $T_p^o = -8^oC$, $\frac{Gr}{Re^2}$ range: $0.11 \div 0.895$

2.4 Conclusions

A new semi-empirical submodel for a particle undergoing phase change phenomena under the influence of convection has been developed. Comparison with experimental data available in the literature showed very good agreement. In particular, we showed that, applied to free convection flows, the use of the film temperature, which is an average of the bulk and surface temperature, gives better agreement with experiments compared to the use of the bulk temperature as a reference. At the same time, when applied to a forced convection or a case when free convection can be neglected, the use of bulk temperature produces results closer to experimental data. Performances of two-temperature formulations of the model are better in comparison to simple one-temperature models. Finally, our model presented in this work can be used in Euler-Lagrange models to "bridge" interfacial (micro) heat and mass transfer with large-scale models used for the modeling of particulate flows where a phase change effect plays an important role.

Chapter 3

Semi Empirical model for particles undergoing phase change: Three phase model

The previous chapter deals with the phase change problems involving two phases, namely solid and liquid. However, there are ample applications in industrial engineering which depend upon the phase change processes involving three phases. So, the idea of semi-empirical models is extended in this chapter for cases where three phases are involved. This work is devoted to the development and validation of a subgrid model describing heat and mass transfer between a hot ambient gas and moving particles undergoing phase change from solid to gas under the influence of convection. As described in previous chapter, such kind of submodels plays the role of 'scale bridges' between microscale (e.g. interfacial heat transfer) and macroscale (e.g. bulk flow) phenomena in different applications in chemical and materials science. Applied to multiscale modeling of particulate flows with phase change phenomena, our model serves as a coupling between equations describing particle movement in Lagrangian space and mass and heat conservation equations defining gas and liquid phases in Eulerian space. The input parameters in our model are the particulate Reynolds number (Re), the Grashof number (Gr), the Stefan number (Ste) and the Prandtl number (Pr) for liquid and gas phases. The model takes into account the solid phase melting/solidification and liquid phase evaporation/condensation. The model has been validated against experimental data applied to the melting of ice sphere and ice cylinder in the atmospheric air under different flow conditions. Good agreement between our model predictions and published experimental data is observed. Before deriving the required equations, the

recent efforts in this area are discussed in next section.

3.1 Introduction

The problem of three phases change 'solid-liquid-gas' is relevant in many engineering applications, such as aerospace (e.g. frost preventing), chemical engineering including combustion engineering. One of the most recurring problem in industrial engineering relevant to three phase change problem is the frost generation on the internal cold surface of pipe when humid air passes through inside which results in decreased heat transfer between air and pipe and higher pressure loss in airflow. Recently, with increased demand on modeling and numerical optimization of transport phenomena in different engineering devices (from aircraft and heat exchangers to large scale chemical reactors and boilers) the role of reliable mathematical models in the engineering design of such devices grew correspondingly. In addition to being robust, such models have to predict adequately (close to reality) the transport phenomena occurring inside devices. In this case the validation of new models is essential part in model justification.

In spite of many experimental works devoted to solid-liquid-gas phase change, numerical or modeling works are rare. In particular, Lee et al. [44] developed an analytical one dimensional model for the frost formation taking into account the molecular diffusion of water vapor and heat generation in frost layer because of sublimation of water vapor. However, they didn't consider the radiative heat transfer between air and frost layer. They calculated the heat and mass transfer in frost layer using empirical correlations on the air side. An absorption coefficient was introduced in Fick's law to obtain the mass transfer equation. The results were compared with experiment results in which humid air was passed over the cooled horizontal plate thereby resulting in frost formation. Lee et al. [45] restricted/skipped the use of empirical correlations and solved set of PDEs instead assuming the frost layer as a porous medium. The heat transfer within the frost layer was defined using the effective thermal conductivity. The model was in good agreement with experimental results with error less than 10% unlike previous existing models since this model didn't use any empirical correlations. However, radiative heat transfer between air and frost layer was again ignored. Murray et al. [46] conducted an experimental study the ice nucleating ability of kaolinite particles immersed within water droplets as function of particle surface area, cooling rate etc.. It was found that freezing temperature changes with the surface area of particles. Wu et al. [47] carried out numerical modeling of an existing experiment in literature applied to

the frost formation. In experiment they considered, a humid airflow was introduced above a cooling source through a thin rectangular channel such that the water vapor in air directly starts condensing into ice crystals as soon as it enters the channel. A mass transfer model was developed in the numerical study to define the phase change mass transfer rate in order to predict the frost layer growth. The calculated mass transfer rate was used in the source terms used in each conservation equation in FLUENT with the implementation of Euler multiphase flow model. The obtained results were claimed to be in good agreement with experiments.

Finally, from the analysis of work cited, it can be seen that some models do not consider the impact of evaporation/condensation on the solid-liquid phase change. Moreover the role of convection in the interaction between liquid and gas phase was not covered at all.

3.2 Model formulation for melting of ice particle in air

A zero-dimensional model for prediction of the size of ice particle melting in atmospheric air is provided in this section. It should be noted that as the ice particle melts, a thin layer of water will develop around its surface. Thus, atmospheric air will exchange heat directly with the water layer and not the solid ice particle. Specifically, following heat transfer processes will be take place as the ice sphere melts:

- Convective heat transfer between air and water layer
- Radiative heat transfer between air and water layer
- Evaporative cooling of water layer
- Conductive heat transfer from air-water interface to water-ice interface

The conductive heat transported to water-ice interface will cause the melting of ice particle and increase in the temperature of ice particle.

3.2.1 Model formulation for spherical ice particle

The required set of equations to find the radius of melting spherical ice particle can be obtained by applying heat balance on the air-water interface and by applying Stefan Boundary condition [13] at ice-water interface. Consider the spherical ice particle shown in fig. 3.1. The water layer around the ice particle is shown by dashed lines with thickness δ_l and with outer surface temperature of T_l and outer

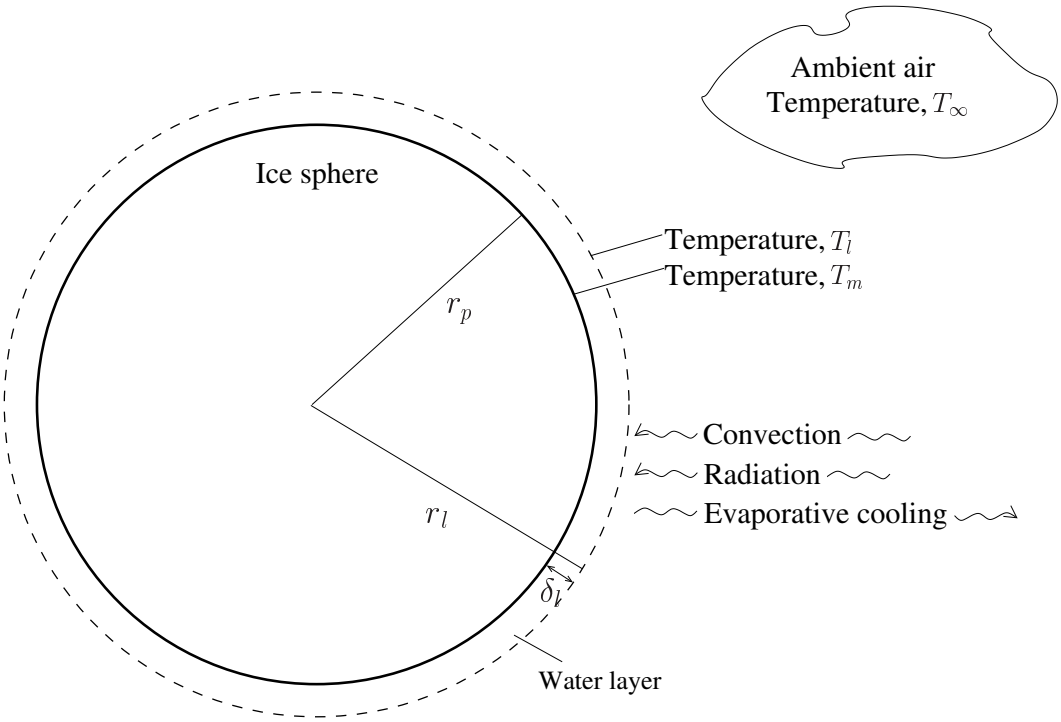

Figure 3.1: Schematic of melting of ice sphere in atmospheric air

radius of r_l. Stefan Boundary condition can be written on ice-water interface as follows:

$$\rho_p h_{sf} \frac{dv_p}{dt} = \frac{4\pi k_p (T_m - T_p)}{1/r_t - 1/r_p} + \frac{4\pi k_l (T_m - T_l)}{1/r_p - 1/r_l} - \tau\sigma T_\infty^4 4\pi r_p^2$$
$$\implies \rho_p h_{sf} r_p^2 \frac{dr_p}{dt} = \frac{k_p (T_m - T_p)}{1/r_t - 1/r_p} + \frac{k_l (T_m - T_l)}{1/r_p - 1/r_l} - \tau\sigma T_\infty^4 r_p^2 \tag{3.1}$$

Similar to the case of spherical particle in chapter 2, $r_t = 0.5^{1/3} r_p$ [41]. Particle temperature can be calculated using following equation:

$$\rho_p v_p c_p \frac{dT_p}{dt} = \frac{4\pi k_p (T_m - T_p)}{1/r_t - 1/r_p} \tag{3.2}$$

The heat balance on water-air interface can be written as follows:

$$\underbrace{h_c(T_l - T_\infty)}_{\text{convection}} + \underbrace{\epsilon\sigma T_l^4 - \alpha_{ab}\sigma T_\infty^4}_{\text{radiation}} + \underbrace{\dot{m}_l'' h_v}_{\text{evaporative cooling}} = \underbrace{\frac{k_l (T_m - T_l)}{(1/r_p - 1/r_l) r_l^2}}_{\text{conduction}} \tag{3.3}$$

where $r_l = r_p + \delta_l$. $\dot{m}_l''$ is the mass flux rate of water vapors leaving the particle surface because of evaporation. The formulation for $\dot{m}_l''$ is derived later in this section.

The equation to calculate water layer thickness, δ_l is provided in section 3.3. The convection coefficient h_c on ice-water interface can be obtained using an appropriate Nusselt number correlation ($h_c = Nu_{d_l} k_\infty / d_l$) according to the free/mixed/forced convection regime. For instance, for the case of free convection, following correlation can be used:

$$Nu_{d_l} = 2 + \frac{0.589 Ra_{d_l}^{1/4}}{(1 + (\frac{0.469}{Pr})^{9/16})^{4/9}} \tag{3.4}$$

where Ra_{d_p}, Rayleigh number is given by:

$$Ra_{d_l} = \frac{g\beta_\infty (T_\infty - T_m) d_l^3}{\alpha_\infty \nu_\infty} \tag{3.5}$$

Next, an equation to determine the mass flux rate of water vapor, $\dot{m}_l^{''}$ will be derived. Consider the spherical particle shown in the fig. 3.2.

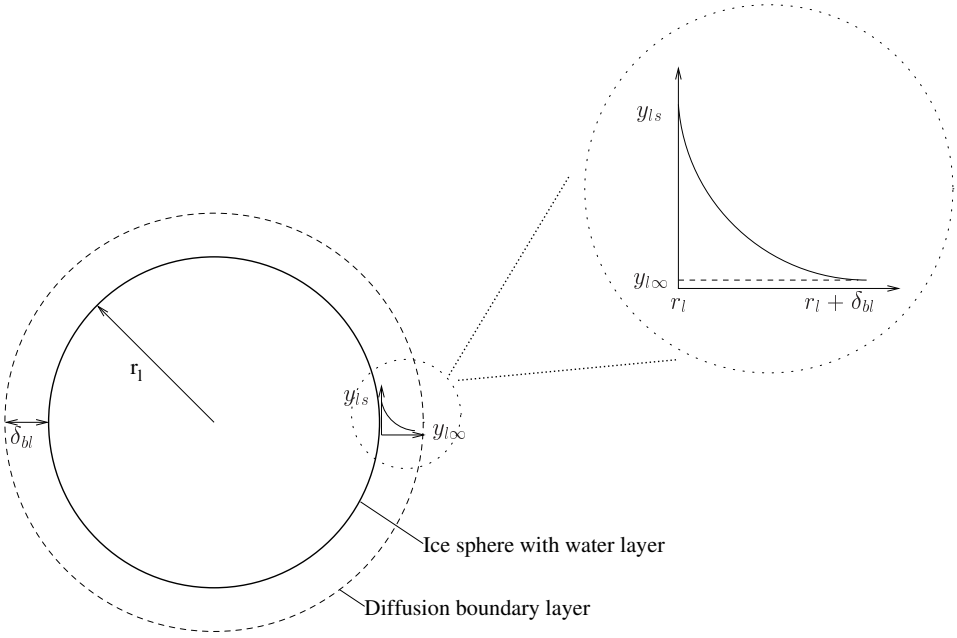

Figure 3.2: Evaporation model for a sphere

The diffusion boundary layer around the surface is shown by dashed lines. The water vapor concentration varies from y_{ls} to $y_{l\infty}$ within this boundary layer where y_{ls} is the mass fraction of water vapor in the atmospheric air at relative humidity of 100% and $y_{l\infty}$ is mass fraction of water vapor in atmospheric air at given air humidity.

Now, for a general 1D case, total mass flux of species A can be written as:

$$\dot{m}_A^{"} = \underbrace{y_A(\dot{m}_A^{"} + \dot{m}_B^{"})}_{\text{Bulk flux}} - \underbrace{\rho D_{AB}\frac{dy_A}{dx}}_{\text{Diffusion flux}} \tag{3.6}$$

Applying this equation to the mass flux of water vapor through the diffusion boundary layer, it takes following form:

$$\dot{m}_l^{"} = y_l \dot{m}_l^{"} - \rho D_{lg}\frac{dy_l}{dr}$$
$$\implies \dot{m}_l^{"} = -\frac{1}{1-y_l}\rho D_{lg}\frac{dy_l}{dr}$$

Multiplying surface area of sphere on both sides, we get mass flow rate of water vapor as follows:

$$\dot{m}_l = 4\pi r^2 \dot{m}_l^{"}$$
$$\implies \dot{m}_l = -\left(\frac{4\pi r^2}{1-y_l}\right)\rho D_{lg}\frac{dy_l}{dr}$$

Since $\dot{m}_l$ remains constant within the boundary layer, above equation can be integrated with respect to y_l and r with following limits:

$$\text{at } r = r_l,\ y_l = y_{ls}$$
$$\text{at } r = r_l + \delta_{bl},\ y_l = y_{l\infty}$$

After integration, $\dot{m}_l$ takes following form:

$$\dot{m}_l = 4\pi\rho D_{lg} ln\left(\frac{1-y_{w\infty}}{1-y_{ws}}\right)\left(\frac{r_l(r_l+\delta_{bl})}{\delta_{bl}}\right)$$
$$\implies \dot{m}_l^{"} = \rho D_{lg} ln\left(\frac{1-y_{w\infty}}{1-y_{ws}}\right)\left(\frac{1}{\delta_{bl}} + \frac{1}{r_l}\right) \tag{3.7}$$

Now, the diffusion boundary layer thickness, δ_{bl} needs to be calculated. It should be noticed that Lewis number for the air is close to 1. It means mass transfer boundary layer thickness is equal to thermal layer boundary thickness for gases. So, δ_{bl} can be calculated by using heat balance at water-air interface. The conductive heat transfer between the water and air through the thermal boundary layer should be equal to the convective heat transfer between water and air. It can be written

as follows:

$$q^{"}_{cond} = \frac{4\pi k_\infty (T_s - T_\infty)}{\left(\frac{1}{r_l} - \frac{1}{r_l+\delta_{bl}}\right) 4\pi r_l^2} \implies q^{"}_{cond} = k_\infty (T_s - T_\infty)\left(\frac{1}{r_l} + \frac{1}{\delta_{bl}}\right)$$

$$q^{"}_{conv} = h_c (T_s - T_\infty)$$

Equating above two heat fluxes, we get

$$\delta_{bl} = \frac{r_l}{Nu_{d_l}/2 - 1} \tag{3.8}$$

where hr_l/k_∞ has been substituted by Nusselt number, Nu_{r_l}. This Nusselt number is exactly the same as used to calculate h_c in eq. 3.3.

Collectively eqs. 3.1, 3.2, 3.3, 3.7, 3.8 completes the submodel for prediction of radius of solid particle melting in atmospheric air due to hot ambient temperature under free/mixed/forced convection. The only parameter which is still undefined is liquid layer thickness, δ_l which is formulated in section 3.3.

3.2.2 Model formulation for cylindrical ice particle

This section provides the submodel to predict the melting of a cylindrical solid particle. Consider a solid ice particle as shown in fig. 3.3. Similar to spherical particle, melting of cylindrical particle can be explained by using the Stefan boundary condition [13] at the ice-water interface and heat balance at air-water interface. Since, cylinder has three distinguished surfaces, Stefan boundary condition will take following form for different surfaces:

Side surface Stefan BC:

$$\rho_p h_{sf} r_p \frac{dr_p}{dt} = \frac{k_p (T_m - T_p)}{ln(r_p/r_t)} + \frac{k_l (T_m - T_{l,s})}{ln(r_l/r_p)} - \tau\sigma T_\infty^4 r_l \tag{3.9a}$$

Top and bottom surface Stefan BC:

$$\rho_p h_{sf} r_p^2 \frac{dl_p}{dt} = \frac{2k_p (T_m - T_p) r_p^2}{(l_p - l_t)/2} + \frac{k_l (T_m - T_{l,t}) r_p^2}{\delta_{l,t}} + \frac{k_l (T_m - T_{l,b}) r_p^2}{\delta_{l,b}} - 2\tau\sigma T_\infty^4 r_p^2 \tag{3.9b}$$

Similar to the case of cylindrical particle in chapter 2, $r_t = 0.5^{1/3} r_p$ and $l_t = 0.5^{1/3} l_p$ [41]. The equation for particle temperature can be obtained as follows:

$$\rho_p v_p c_p \frac{dT_p}{dt} = \frac{2k_p \pi r_p^2 (T_m - T_p)}{(l_p - l_t)/2} + \frac{2\pi k_p l_p (T_m - T_p)}{ln(r_p/r_t)} \tag{3.10}$$

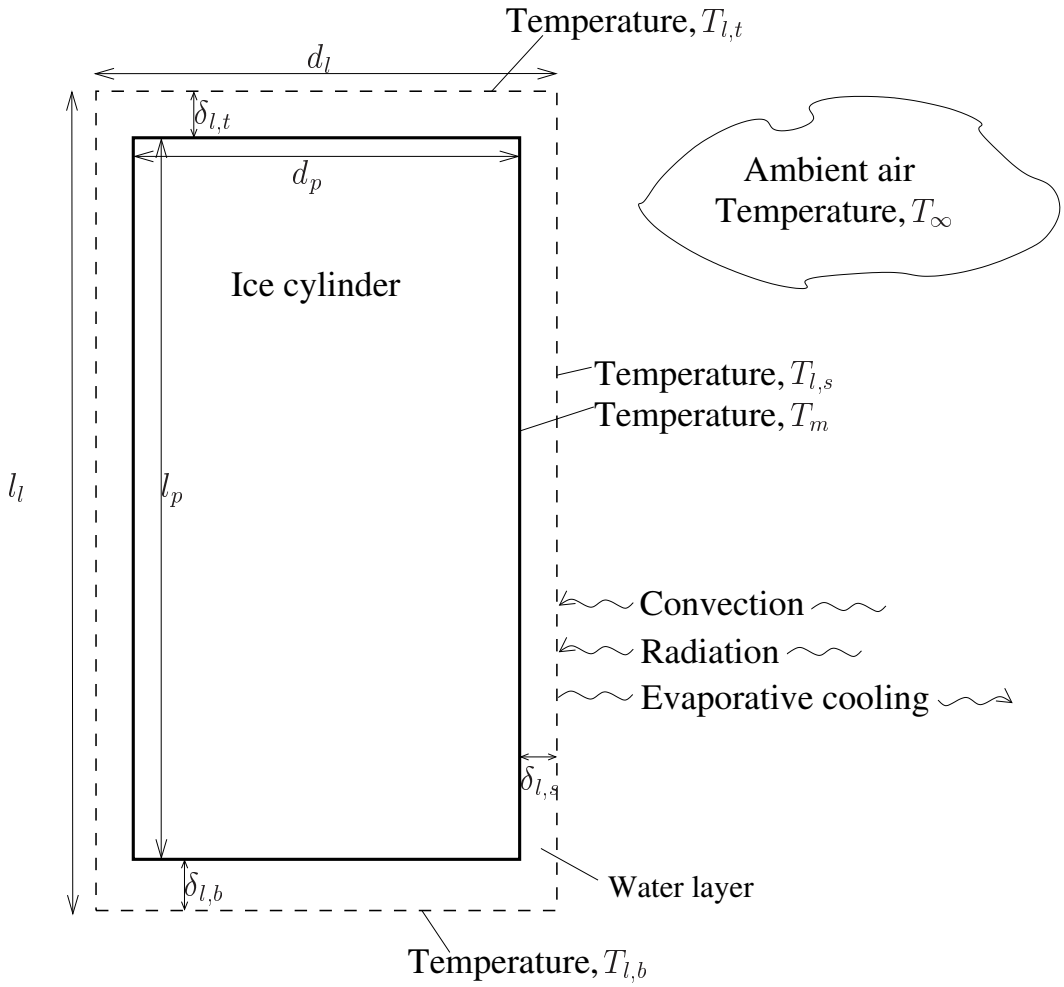

Figure 3.3: Scheme of cylindrical particle submodel

The heat balance equations can be written on the surfaces as follows:

Side surface heat balance:

$$(h_{c,s}(T_{l,s} - T_\infty) + (\epsilon\sigma T_{l,s}^4 - \alpha_{ab}\sigma T_\infty^4)r_l + r_l\dot{m}_{l,s}^{''}h_v = \frac{k_l(T_m - T_{l,s})}{ln(r_l/r_p)} \tag{3.11a}$$

Top surface heat balance:

$$h_{c,t}(T_{l,t} - T_\infty) + \epsilon\sigma T_{l,t}^4 - \alpha_{ab}\sigma T_\infty^4 + \dot{m}_{l,t}^{''}h_v = \frac{k_l(T_m - T_{l,t})}{\delta_{l,t}} \tag{3.11b}$$

Bottom surface heat balance:

$$h_{c,b}(T_{l,b} - T_\infty) + \epsilon\sigma T_{l,b}^4 - \alpha_{ab}\sigma T_\infty^4 + \dot{m}_{l,b}^{''}h_v = \frac{k_l(T_m - T_{l,b})}{\delta_{l,b}} \tag{3.11c}$$

The formulations for evaporation mass fluxes, $\dot{m}''_{l,s}$, $\dot{m}''_{l,t}$, $\dot{m}''_{l,b}$ are provided later in this section. The formulation for water layer thickness, $\delta_{l,s}$, $\delta_{l,t}$, $\delta_{l,b}$ are provided in section 3.3. The heat transfer coefficients are given by:

$$h_{c,s} = \frac{Nu_{l_s^c,s} k_\infty}{l_s^c}; h_{c,t} = \frac{Nu_{l_t^c,t} k_\infty}{l_t^c}; h_{c,b} = \frac{Nu_{l_b^c,b} k_\infty}{l_b^c} \tag{3.12}$$
$$\text{with characteristic lengths: } l_s^c = l_l;\ l_t^c = d_l/4;\ l_b^c = d_l/4$$

where characteristic length for top and bottom surface is calculated by dividing area by parameter of surface. Appropriate Nusselt number correlations according to the nature of convective heat transfer process should be used. For instance, for free convection around the particle, following correlations can be used:

$$Nu_{l_s^c,s} = 0.68 + \frac{0.67 Ra_{l_s^c}^{0.25}}{\left(1 + \left(\frac{0.492}{Pr}\right)^{(9/16)}\right)^{(4/9)}}; \quad Nu_{l_t^c,t} = 0.27 Ra_{l_t^c}^{0.25}; \quad Nu_{l_b^c,b} = 0.54 Ra_{l_b^c}^{0.25} \tag{3.13}$$

$$Ra_{l_s^c} = \frac{g\beta_\infty (T_\infty - T_m) {l_l}^3}{\nu_\infty \alpha_\infty};\ Ra_{l_t^c} = Ra_{l_b^c} = \frac{g\beta_\infty (T_\infty - T_m)(d_l/4)^3}{\nu_\infty \alpha_\infty} \tag{3.14}$$

The mass flux rates of water vapor, $\dot{m}''_{l,s}$, $\dot{m}''_{l,t}$, $\dot{m}''_{l,b}$ can be derived in similar way to spherical particle. Applying 3.6 in this case results in following equations:

$$\dot{m}''_{l,s} = -\frac{1}{1-y_l} \rho D_{lg} \frac{dy_l}{dr}$$
$$\dot{m}''_{l,t} = -\frac{1}{1-y_l} \rho D_{lg} \frac{dy_l}{dz}$$
$$\dot{m}''_{l,b} = -\frac{1}{1-y_l} \rho D_{lg} \frac{dy_l}{dz}$$

Multiplying both sides by flux area to obtain mass transfer rates:

$$\dot{m}_{l,s} = -\frac{2\pi r l}{1-y_l} \rho D_{lg} \frac{dy_l}{dr}$$
$$\dot{m}_{l,t} = -\frac{\pi r^2}{1-y_l} \rho D_{lg} \frac{dy_l}{dz}$$
$$\dot{m}_{l,b} = -\frac{\pi r^2}{1-y_l} \rho D_{lg} \frac{dy_l}{dz}$$

Since mass transfer rates would remain constant within the boundary layer, above equations can be integrated with respect to y_l and r and z with the integral limits

of y_{ls} and $y_{l\infty}$ to get following mass flux equations:

$$\dot{m}''_{l,s} = \frac{\rho D_{lg} ln\left(\frac{1-y_{l\infty}}{1-y_{ls}}\right)}{r_l ln\left(\frac{r_l+\delta_{bl,s}}{r_l}\right)} \tag{3.15a}$$

$$\dot{m}''_{l,t} = \frac{\rho D_{lg} ln\left(\frac{1-y_{l\infty}}{1-y_{ls}}\right)}{\delta_{bl,t}} \tag{3.15b}$$

$$\dot{m}''_{l,b} = \frac{\rho D_{lg} ln\left(\frac{1-y_{l\infty}}{1-y_{ls}}\right)}{\delta_{bl,b}} \tag{3.15c}$$

The diffusion boundary layers, $\delta_{bl,s}$, $\delta_{bl,t}$, $\delta_{bl,b}$ can be defined in similar way as for spherical particle by comparing it with the thermal boundary layers. So,

$$\delta_{bl,s} = (exp(2/Nu_{l^c_s,s}) - 1)r_l \tag{3.16a}$$

$$\delta_{bl,t} = k_\infty/h_{c,t} = l^c_t/Nu_{l^c_t,t}; \tag{3.16b}$$

$$\delta_{bl,b} = k_\infty/h_{c,b} = l^c_b/Nu_{l^c_b,b}; \tag{3.16c}$$

where Nusselt numbers are same as used in eq. 3.12. Collectively, eqs. 3.9, 3.10, 3.11,3.12 and 3.15 constitute the submodel for cylindrical particle. The formulation for water layer thickness $\delta_{l,s}$, $\delta_{l,t}$, $\delta_{l,b}$ are provided in section 3.3.

3.3 Water layer thickness around the particle

As the ice particle melts, it will develop a thin layer of water over its surface. Starting from zero, the thickness of this layer will keep increasing until the weight of this layer becomes larger than the friction force between the layer and surface of solid particle. Thereafter, water will start flowing down because of gravity and water layer would attain a steady constant thickness profile. This water layer around the particle is crucial in deciding the conductive heat transfer from air-water interface to ice-water interface which insulates, however minimal, the solid particle from ambient temperatures. Applied to our case of melting of ice particle, water layer thickness is expected to be of the order of 10^{-4} m (as shown later in this section). The thickness profile can be predicted numerically via microscopic momentum equation i.e. Navier Stokes equation. While deriving the final equation, we will make following assumptions:

- Thickness of layer is very small such that velocity in the direction perpendicular to surface of particle is much smaller than that in the direction of flow.

This assumption will be justified at the end of this section.

- Due to symmetry of all the geometries, velocity in the y-axis (for Cartesian coordinates), $\vec{\theta}$ direction (for cylindrical coordinates) and in $\vec{\theta}$ direction (for spherical particle) will assumed to be zero.

- Water layer thickness at the top of the particle will assumed to be zero

The first two assumptions leave us with only one component of velocity which is in the direction of gravity. In subsequent calculations, melting rate of particle will be taken into account using the term v_{melt}. v_{melt} is melting velocity at which water comes out throughout the entire solid surface as shown in figs. 3.4, 3.5, 3.6 for different geometries. Thus, mass flux of water because of melting will be equal to ρv_{melt}. The two different approaches are used to calculate water layer thickness in following subsections. First subsection uses the Navier-Stokes equation and second subsection uses the overall balance between drag forces and gravity forces on particle. In this section, subscript 'l' from water layer thickness, δ_l will be omitted.

3.3.1 Equation of motion

Cartesian coordinates:
Consider the differential volume element of thickness dz of the falling film of water as shown in fig. 3.4. Within this element, local velocity of water in $\vec{z}$ direction can be assumed to be independent of z and due to symmetry, independent of y as well leaving it to be a function of x alone i.e. $v_z \equiv v_z(x)$. Thus, Navier stokes equation can be written as:

$$0 = \mu \frac{\partial^2 v_z}{\partial x^2} + \rho g_z$$

Integrating above equation using the following boundary conditions:

$$\frac{\partial v_z}{\partial x} \text{ (at x = } \delta) = 0$$
$$v_z(x = 0) = 0$$

we get,

$$v_z = -\frac{\rho g}{\mu}(\frac{x^2}{2} - \delta x)$$

Taking average over the thickness, we get:

$$\bar{v_z}(z) = \frac{\rho g \delta(z)^2}{3\mu}$$

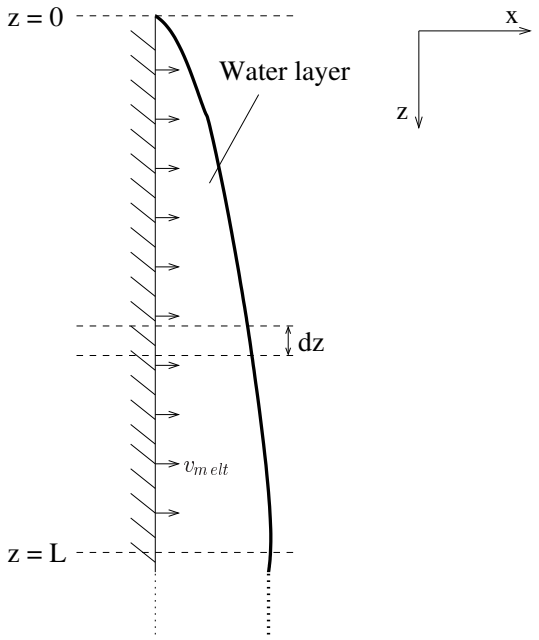

Figure 3.4: Water layer on a vertical flat surface

This gives us the dependency between water layer thickness and its average falling velocity. To relate the thickness with melting velocity v_{melt}, following mass balance can be applied on the control volume between $z = 0$ and $z = L$ as shown in fig. 3.4:

$$\underbrace{\rho \bar{v}_z(L)\delta(L) + \dot{m}''_{evap}L}_{\text{mass out}} - \underbrace{\dot{m}''_{melt}L}_{\text{mass in}} = 0$$

where $\dot{m}''_{evap}$ and $\dot{m}''_{melt}$ are water mass flux terms due to evaporation and melting respectively. Here, it is assumed that the surface over which $\dot{m}''_{evap}$ is acting has same area as for $\dot{m}''_{melt}$. Substituting v_z in this equation, we get

$$\frac{\rho^2 g \delta(L)^3}{3\mu} + (\dot{m}''_{evap} - \dot{m}''_{melt})L = 0$$

$$\implies \delta(L) = \left(\frac{3\mu(\dot{m}''_{melt} - \dot{m}''_{evap})L}{\rho^2 g} \right)^{1/3} \tag{3.17}$$

Mass flux terms $\dot{m}''_{evap}$ and $\dot{m}''_{melt}$ can also be written as ρv_{evap} and ρv_{melt} respectively where v_{evap} and v_{melt} are the evaporation and melting velocity of water.

Cylindrical coordinates:
Same equation for water layer thickness can be derived for cylindrical particle as

well. Consider the cylindrical ice particle shown in fig. 3.5. Let us consider the

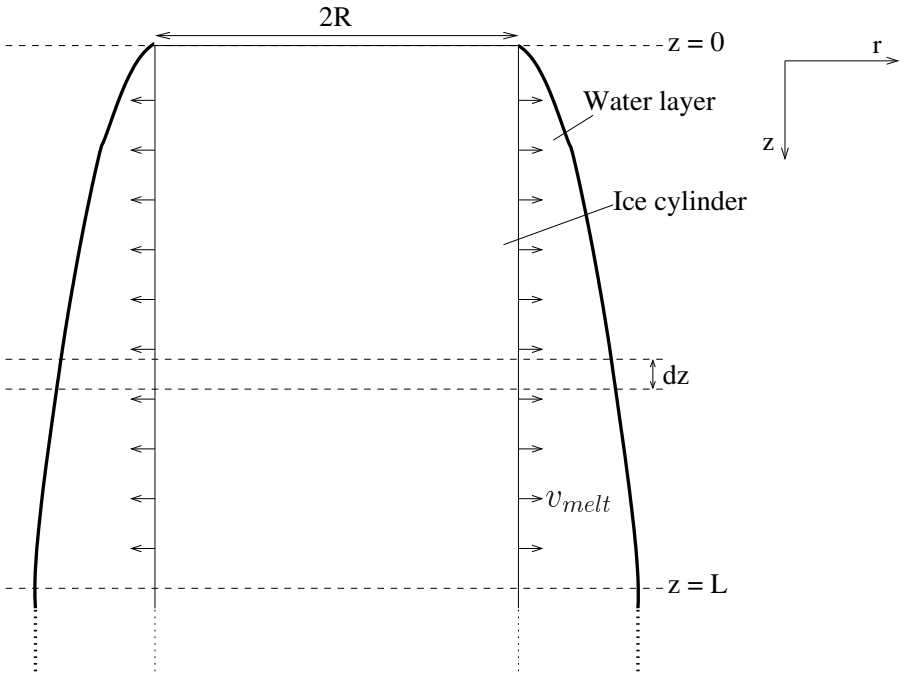

Figure 3.5: Water layer around cylindrical ice particle

differential element of thickness dz as shown in fig. 3.5. Similar to Cartesian coordinates, assuming symmetry in $\vec{\theta}$ direction, velocity v_z will be the function of radial distance alone i.e. $v_z \equiv v_z(r)$. Applying the Navier Stokes equation on the differential element shown, we get

$$0 = \mu \left(\frac{1}{r} \frac{\partial}{\partial r} \left(r \frac{\partial v_z}{\partial r} \right) \right) + \rho g_z$$

Integrating it with following boundary conditions:

$$\frac{\partial v_z}{\partial r} \text{ (at r = R+ } \delta) \ = 0$$

$$v_z \text{ (at r = R)} \ = 0$$

we get,

$$v_z(r) = \frac{-\rho g_z}{2\mu} \left(\frac{r^2 - R^2}{2} - (R+\delta)^2 ln \left(\frac{r}{R} \right) \right)$$

Taking average over the water layer,

$$\bar{v}_z = \frac{\int_R^{R+\delta} v_z 2\pi r dr}{\pi((R+\delta)^2 - R^2)} = \frac{\int_R^{R+\delta} v_z 2\pi r dr}{2\pi R\delta} = \frac{\int_R^{R+\delta} v_z r dr}{R\delta}$$

where

$$\int_R^{R+\delta} v_z r dr = \int_R^{R+\delta} \frac{-\rho g}{2\mu} \left(\left(\frac{r^3 - R^2 r}{2} \right) - (R+\delta)^2 ln \left(\frac{r}{R} \right) r \right) dr$$

$$= \frac{-\rho g}{2\mu} \left(\frac{(R+\delta)^4 - R^4}{8} - \frac{R^2}{4}((R+\delta)^2 - R^2) \right) +$$
$$\frac{\rho g}{2\mu}(R+\delta)^2 \left(\frac{(R+\delta)^2}{2} ln(1+\delta/R) - \frac{(R+\delta)^2 - R^2}{4} \right)$$

Expanding all the terms and ignoring all the terms in which δ has exponent higher than 3, we get

$$\int_R^{R+\delta} v_z r dr = \frac{\rho g R \delta^3}{3\mu}$$

Substituting it in expression for $\bar{v}_z$, we get

$$\bar{v}_z(z) = \frac{\rho g \delta(z)^2}{3\mu}$$

To relate the thickness with v_{melt}, mass balance can be performed on the control volume between $z = 0$ and $z = L$ shown in fig. 3.5. Mass balance equation can be written as follows:

$$\underbrace{\rho \bar{v}_z \pi((R+\delta)^2 - R^2) + \dot{m}''_{evap} 2\pi RL}_{\text{mass out}} - \underbrace{\dot{m}''_{melt} 2\pi RL}_{\text{mass in}} = 0$$
$$\implies \rho \bar{v}_z 2\pi R\delta + (\dot{m}''_{evap} - \dot{m}''_{melt}) 2\pi RL = 0$$

Here, advantage of small δ with respect to R has been utilized to write the surface area of film flow as $2\pi R\delta$. Substituting expression for $\bar{v}_z$ in above equation and rearranging, we get

$$\delta = \left(\frac{3\mu(\dot{m}''_{melt} - \dot{m}''_{evap})L}{\rho^2 g} \right)^{1/3} \tag{3.18}$$

Spherical coordinates:

Considering the spherical ice particle shown in fig. 3.6, same approach can be used in this case to calculate water layer thickness.

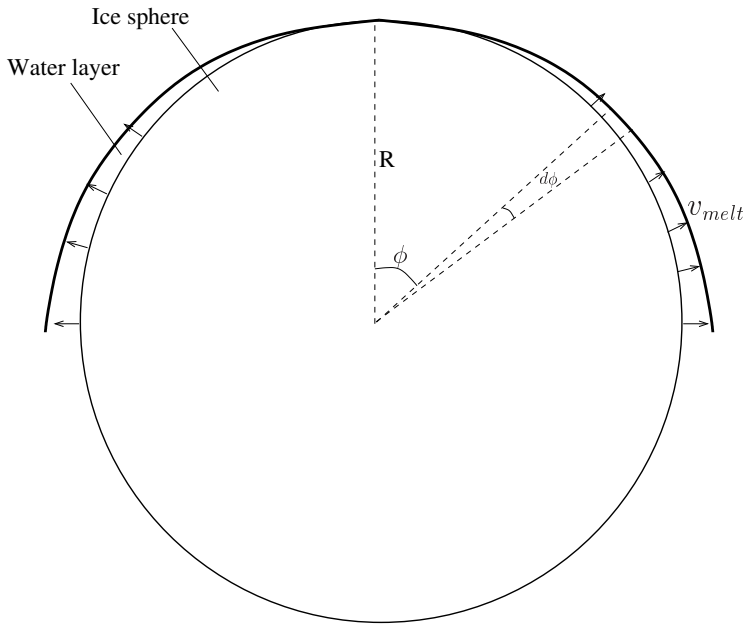

Figure 3.6: Water layer around spherical ice particle

As shown in figure, a differential element is considered at the angle ϕ from the vertical axis. Assuming symmetry in θ, velocity in the differential element can be represented by the function of r alone i.e. $v_\phi \equiv v_\phi(r)$. Applying the Navier Stokes equation for this differential element shown, we get

$$0 = \rho g sin\phi + \mu \left(\frac{1}{r^2} \frac{\partial}{\partial r} \left(r^2 \frac{\partial v_\phi}{\partial r} \right) \right)$$

Integrating above equation using following boundary conditions:

$$\begin{aligned} \frac{\partial v_\phi}{\partial r} \text{ (at } r = R + \delta) &= 0 \\ v_\phi \text{ (at r = R)} &= 0 \end{aligned}$$

we get,

$$v_\phi = \frac{-\rho g sin\phi}{3\mu} \left(\frac{r^2 - R^2}{2} + (R+\delta)^3 \left(\frac{1}{r} - \frac{1}{R} \right) \right)$$

Average velocity, $\bar{v}_\phi$ over the water layer can be calculated as:

$$\bar{v}_\phi = \frac{\int_R^{R+\delta} v_\phi 2\pi r sin\phi dr}{2\pi R sin\phi \delta} = \frac{\int_R^{R+\delta} v_\phi r dr}{R\delta}$$

where

$$\int_R^{R+\delta} v_\phi r dr = \frac{-\rho g sin\phi}{6\mu}\left(\frac{(R+\delta)^4 - R^4}{4} - \frac{R^2}{4}((R+\delta)^2 - R^2)\right) - \frac{\rho g sin\phi}{6\mu}(R+\delta)^3\left(\delta - \frac{1}{2R}((R+\delta)^2 - R^2)\right)$$

Expanding all the terms and ignoring terms in which δ has exponent more than 3, we get

$$\int_R^{R+\delta} v_\phi r dr = \frac{\rho g sin\phi R\delta^3}{3\mu}$$

Substituting it in expression for $\bar{v}_\phi$,

$$\bar{v}_\phi = \frac{\rho g sin\phi \delta^2}{3\mu}$$

Considering the control volume between $\phi = 0$ and $\phi = \pi/2$, mass balance can be applied as follows:

$$\underbrace{\rho\bar{v}_\phi 2\pi R\delta + \dot{m}''_{evap} 2\pi R^2}_{\text{mass out}} - \underbrace{\dot{m}''_{melt} 2\pi R^2}_{\text{mass in}} = 0$$

Substituting expression for $\bar{v}_\phi$ in above equation and rearranging, we get:

$$\delta = \left(\frac{3\mu(\dot{m}''_{melt} - \dot{m}''_{evap})R}{\rho^2 g}\right)^{1/3} \tag{3.19}$$

3.3.2 Simple model - balancing gravity and friction

In this section, a simple model is provided for prediction of water layer thickness. This model balances the drag and gravitational force on water layer resulting in following equations for different geometries:

Cartesian coordinates:

$$\frac{1}{2}C_D\rho\bar{v}_\phi^2 = \rho\delta g \tag{3.20}$$

Cylindrical coordinates:

$$\frac{1}{2}C_D\rho\bar{v}_\phi^2 2\pi RL = \rho\pi((R+\delta)^2 - R^2)Lg \tag{3.21}$$

Spherical coordinates:

$$\frac{1}{2}C_D\rho\bar{v}_\phi^2 4\pi R^2 = \rho\frac{4\pi}{3}((R+\delta)^3 - R^3)g \tag{3.22}$$

where appropriate correlation for drag coefficient should be used according to the Reynolds number of water film flow. Coupling above equations with the mass balance equations given in section 3.3.1 for each geometry, δ can be calculated.

3.3.3 Validation

Due to the lack of experimental data, the results of the above mentioned equations were compared to a FLUENT-based [48] CFD model for spherical particle. The principle scheme of the CFD model is shown in fig. 3.7. The Volume of Fluid (VOF) model was used in FLUENT. The evaporation velocity v_{evap} is absent in this model. So, v_{evap} will be considered zero in the subsequent calculations in this section. The model was run for four different values of v_{melt} namely 0.001 m/s, 0.05 m/s, 0.01 m/s and 0.1 m/s. Figs. 3.8 and 3.9 shows the snapshots of FLUENT results after water layer attains steady thickness. Fig. 3.10 plots the FLUENT-based CFD model results and results from equations derived in sections 3.3.1 and 3.3.2. As it can be seen from the figure, Navier-Stokes based model is in good agreement with CFD data only for small melting velocities. However, in our case of melting of ice particles, melting velocities are typically very low. For example, in case of our experiments of melting of spherical ice particle (explained in next section), melting velocity averaged over the entire time of melting and averaged over the surface of sphere comes out to be $1.009 \cdot 10^{-6}$ m/s which is way lower than the melting velocities considered in CFD-based model. The grid used in CFD-based model consisted of 50756 cells. The time step of $5 \cdot 10^{-5}$ second was used. Second order upwind scheme was used for discretization of momentum conservation equation.

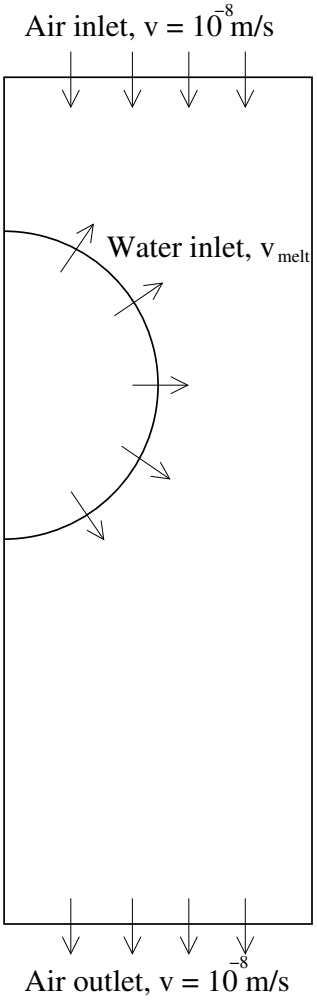

Figure 3.7: Principle schematic for CFD-based model

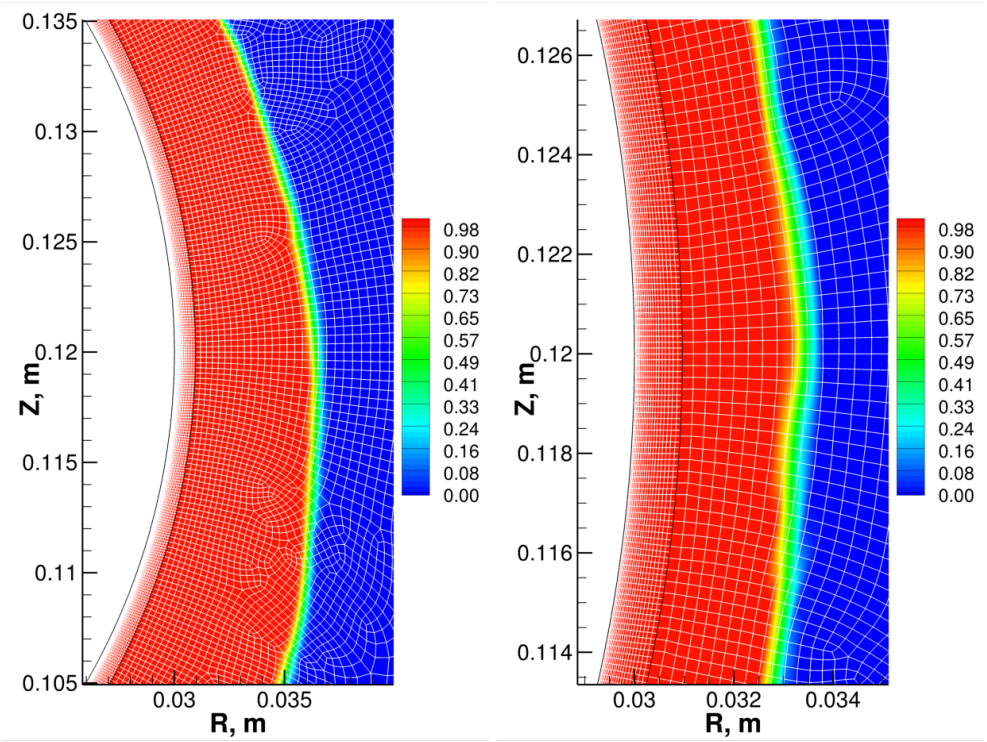

(a) v = 0.1 m/s (b) v = 0.05 m/s

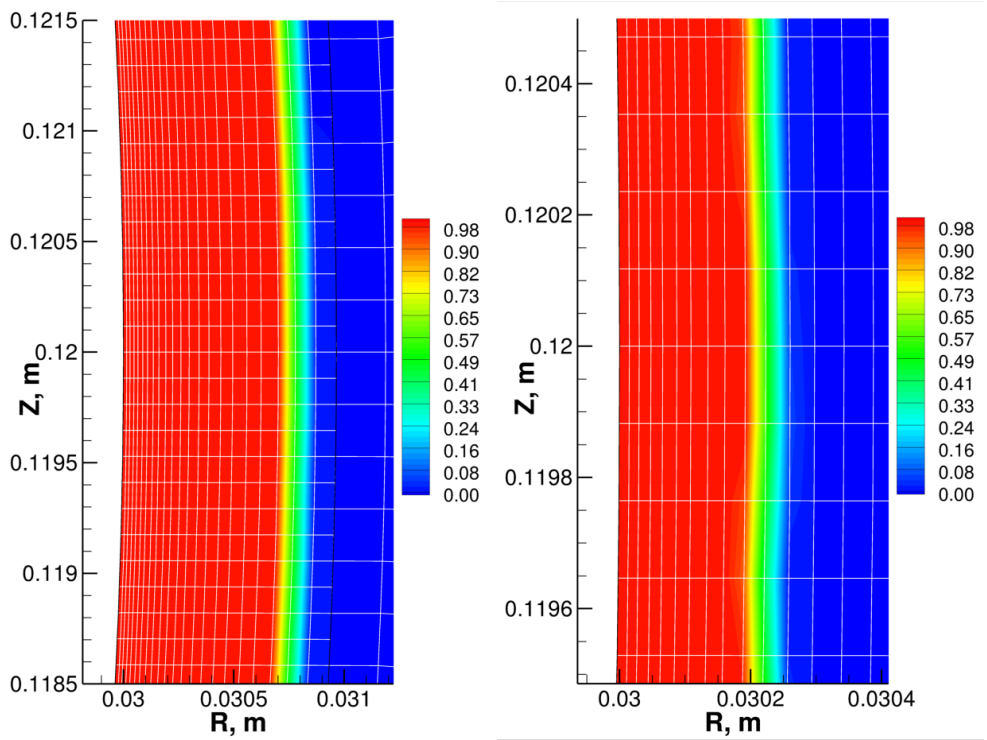

(c) v = 0.01 m/s (d) v = 0.001 m/s

Figure 3.8: Water layer thickness with different velocities of water, v = 0.1 m/s, v = 0.05 m/s, v = 0.01 m/s, v = 0.001 m/s,

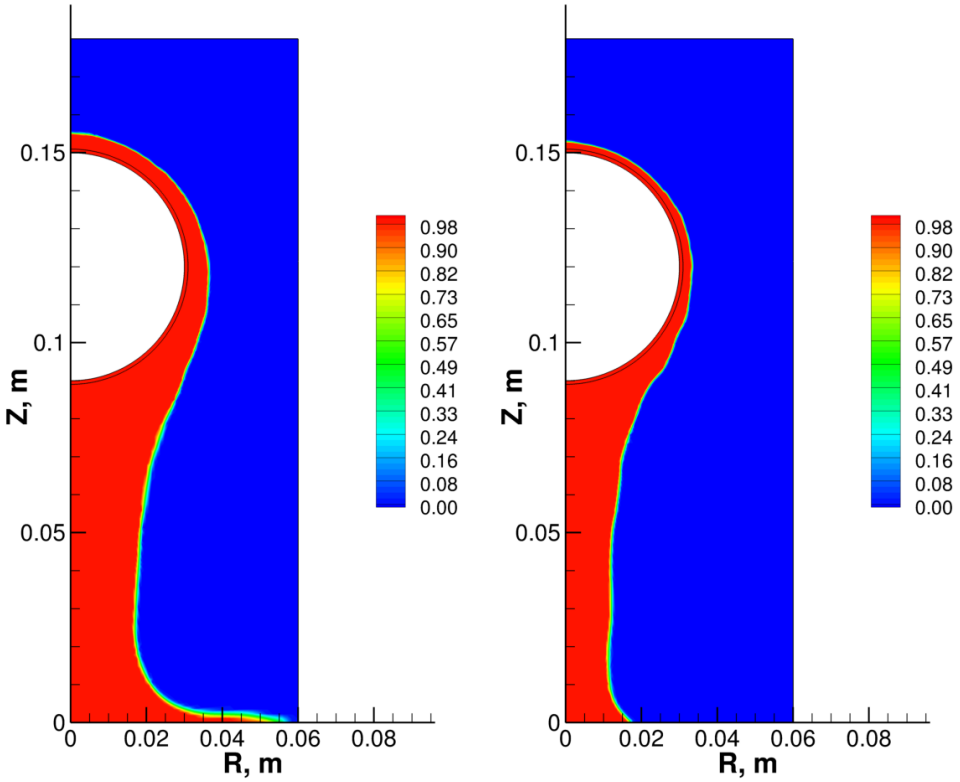

(a) v = 0.1 m/s (b) v = 0.05 m/s

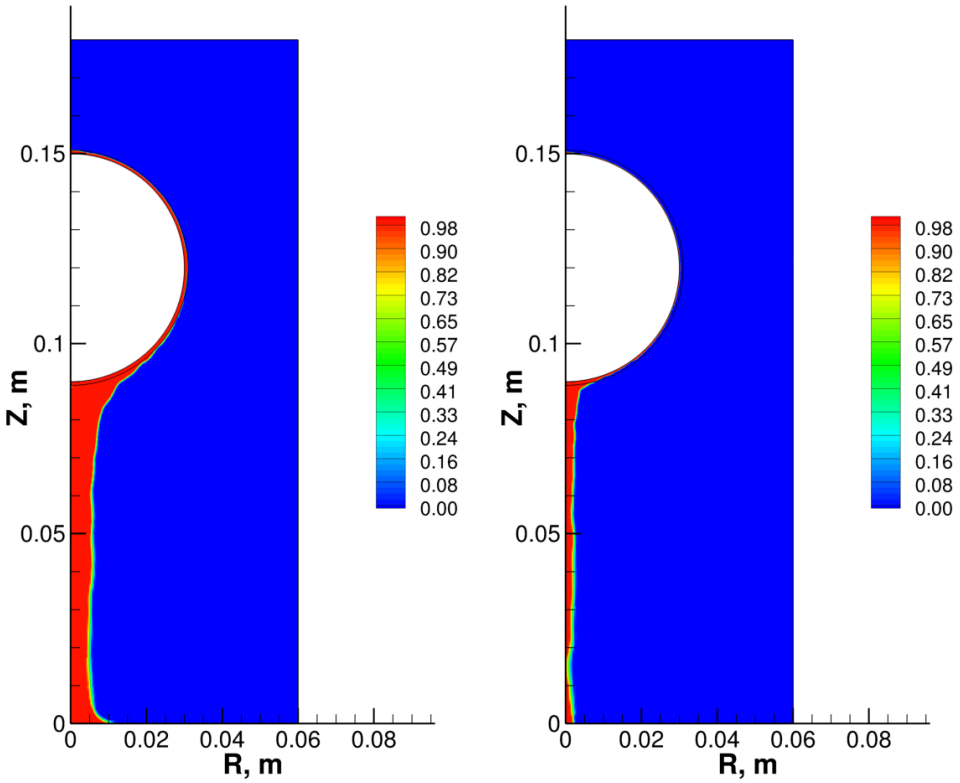

(c) v = 0.01 m/s (d) v = 0.001 m/s

Figure 3.9: Water layer thickness with different velocities of water, v = 0.1 m/s, v = 0.05 m/s, v = 0.01 m/s, v = 0.001 m/s,

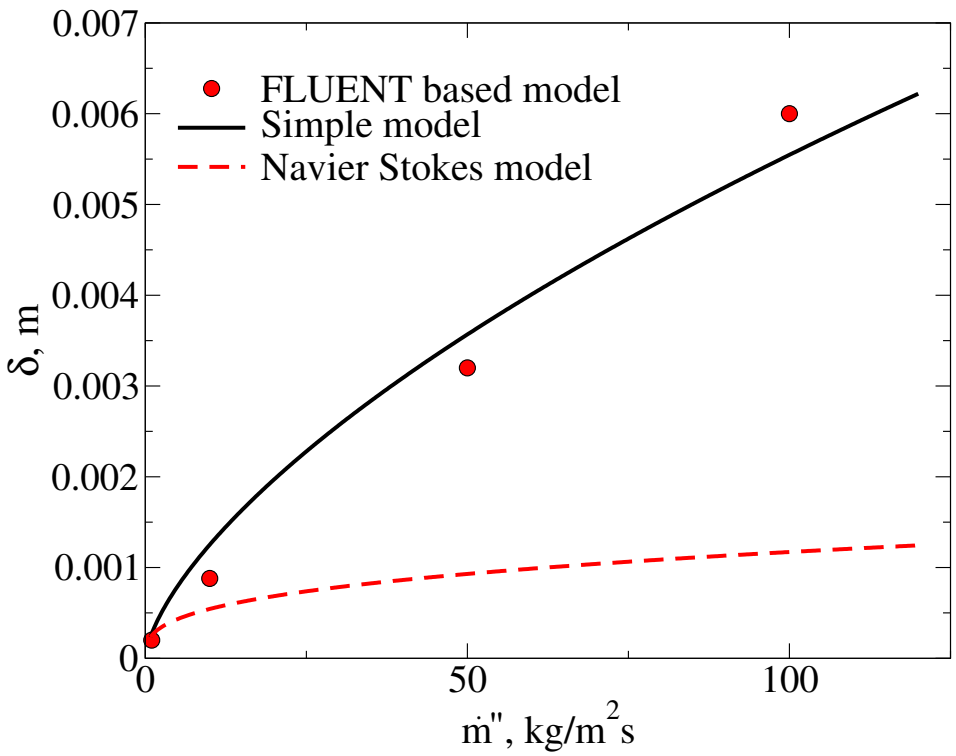

Figure 3.10: Predicted water thickness for different mass flux $\dot{m}''$ values

3.4 Validation

The submodel provided in section 3.2 for spherical and cylindrical ice particle is validated in this section against various experimental results. Also, the equation for mass flux of water vapor is validated separately against an existing experimental result [4]. The submodel for cylindrical ice particle will be compared against the experimental study conducted by Janna and Jakubowski [5] while submodel for spherical ice particle will be compared against our own experiments.

3.4.1 Evaporation flux

In this section, we will compare the water vapor mass flux values calculated using eq. 3.15a with the experimental results available in literature[4]. Nobel [4] carried out experiments in which water was evaporated from the horizontally aligned wet cylindrical surface. In short, a filter paper was placed around a cotton filled horizontal cylindrical tube with a thin slit on one side. The paper was kept wet through this slit so that it is in contact with the moistened cotton inside the tube. An air stream normal to the axis of cylinder was blown. Table 3.2 shows the conditions in

which experiments were carried out. To keep the consistency of variables as defined in section 3.2, subscript l is used in the table to denote the dimensions of cylindrical tube.

Table 3.1: Wet cylinder and ambient air properties in experiments conducted by Nobel [4]

Cylinder diameter, d_l	2 cm
Cylinder axial length, l_l	10 cm
Ambient air temperature, T_∞	20.1 C
Wind velocity, u_∞	10 cm/sec - 1000 cm/sec
Concentration of water at surface, C_{ws}	16.8 gm/cm^2
Concentration of water in ambient air, $C_{w\infty}$	9.8 gm/cm^2

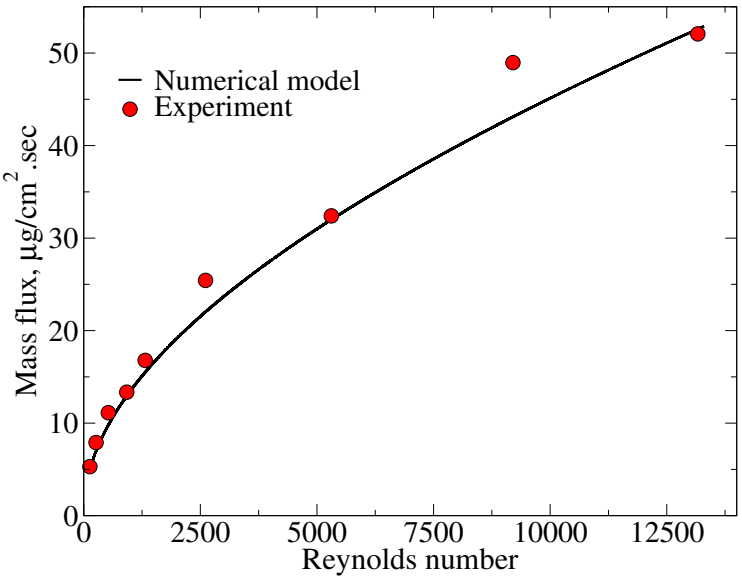

Figure 3.11: Comparison between experimental [4] results and numerical results

As water will evaporate from the wet filter paper, a diffusion mass transfer boundary layer will develop around the filter paper as depicted in section 3.2 within which concentration of water vapors varies from y_{ws} to $y_{w\infty}$. Implementing eq. 3.15a for this case, mass flux rate of water vapor can be predicted. Since the considered experiment is a case of forced convection over horizontal cylinder, following Nusselt number can be used [1]:

$$Nu_{s,d_l} = 0.3 + \frac{0.62 Re_{d_l}^{1/2} Pr^{1/3}}{(1+(0.4/Pr)^{2/3})^{1/4}} \left(1 + \left(\frac{Re_{d_l}}{2.82 * 10^5}\right)^{5/8}\right)^{4/5} \quad \text{where } Re.Pr > 0.2 \tag{3.23}$$

Converting concentrations of water given in table 3.2 to the mass fractions y_{ws} and $y_{w\infty}$ and then using eqs. 3.15a, 3.16a and 3.23, mass flux rate of water vapor leaving the wet cylindrical tube can be predicted. Fig.3.11 shows the comparison between numerical and experimental results. The Reynolds number plotted on the x-axis was following function of u_{air}:

$$Re_{d_l} = \frac{\rho_\infty u_\infty d_l}{\mu_\infty} \tag{3.24}$$

where properties of air were calculated at ambient temperature, T_∞. Various thermophysical properties used in the calculations are listed below:

Table 3.2: Wet cylinder and ambient air properties in experiments conducted by Nobel [4]

Thermophysical property	Numerical value
Air density, ρ_∞	1.1929 kg/m^3
Dynamic viscosity, μ_∞	$181.2250 \cdot 10^-7$ Pa-s
Air Prandtl number, Pr	0.7087
Diffusion coefficient, D_{lg}	$0.24 \cdot 10^-4$ m^2/s

3.4.2 Three-phase change model for cylindrical particle

Janna and Jakubowski [5] carried out an experiment in which an ice cylinder was suspended by a string in air with its axis aligned vertically. Other end of string was attached to the cantilever beam. A strain gage was attached to the beam to measure the weight of ice cylinder as it melts. Principle scheme of the experimental setup is shown in fig. 3.12.

Table 3.3 lists the various parameters at the start of experiment.

Table 3.3: Ice sample and air properties at the start of experiment [5]

Ice cylinder diameter, d_p	0.14 m
Ice cylinder length, l_p	0.146 m
Ambient air temperature, T_∞	298 K
Ice cylinder temperature, T_p	273 K

Since this is a case of three phase change problem, the submodel for cylindrical particle provided in section 3.2.2 can be used to predict the size of particle. Relative humidity of air is assumed to be 20% since it was not mentioned explicitly in the reported data [5] while air next to the water layer is assumed to be fully saturated i.e. having relative humidity of 100%. y_{ws} and $y_{w\infty}$ can be easily calculated by

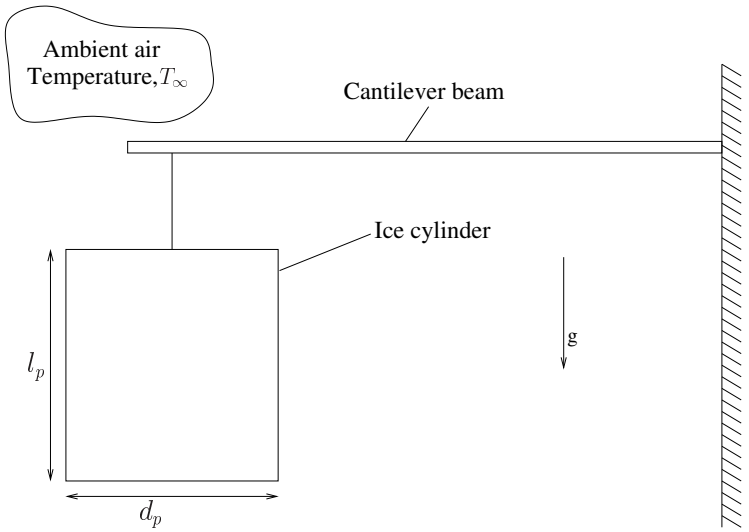

Figure 3.12: Principle scheme of the experimental setup [5]

converting relative humidity of air into mass fraction of water vapor using mole concept. Within each time step, following steps are followed to calculate the radius and height of cylinder:

- Calculate Rayleigh numbers using eqs.3.14 for all the three surfaces
- Calculate Nusselt numbers using correlation for the case of free convection using eqs. 3.13 and then calculate heat transfer coefficients using eqs. 3.12.
- Solve eqs. 3.16 for diffusion boundary layer thickness for three surfaces.
- Using eqs. 3.15, determine mass flux rates of water vapor at each surface.
- Solve non-linear heat balance equations given by 3.11 to find $T_{l,s}$, $T_{l,t}$ and $T_{l,b}$.
- Solve Stefan boundary equations given by 3.9 to calculate radius and height of ice particle.

The water layer thickness at each time step is calculated using eq. 3.18. The thermophysical properties of water and air used in calculations correspond to the temperature value of 273.15 K and 298.15 K respectively. Table 3.4 lists numerical value of various thermophysical properties used in calculations. Euler's explicit-based method with time step of 0.01 second was used to solve the Stefan boundary conditions. Lower time step values produced similar results.

Fig.3.13 compares the submodel and experimental results. Two different curves for submodel results can be seen in the figure with the difference being the different emissivity values of water layer used in calculations. It has been reported in

Table 3.4: Ice and air properties used in the validation process

Physical property	Numerical value
Ice	
ρ_p	920 kg/m^3
k_p	1.88 W/mK
c_p	2040 J/kgK
Air	
ρ_∞	1.180 kg/m^3
k_∞	0.0260 W/mK
μ_∞	$182.6 \cdot 10^{-7}$ Ns/m^2
$c_{p\infty}$	1006.92 J/kgK
β_∞	$3.3955 \cdot 10^{-3}$ K^{-1}
Water	
ρ_l	1000 kg/m^3
k_l	0.569 W/mK
μ_l	$1750 \cdot 10^{-6}$ Ns/m^2
Latent heats	
h_{sf}	$333.6 \cdot 10^3$ J/kg
h_v	$2260 \cdot 10^3$ J/kg
Radiation	
α_{ab}	0.1
τ	0.9

literature that a thin film of any liquid will take emissivity value lesser than that of bulk fluid [49],[50]. Emissivity of bulk water is 0.96 but for thin film of water, emissivity will take different value lesser than 0.96. Brissinger et al. [51] investigated radiative transfer through water film of different thickness. He concluded that water film with thickness 100-1000 μm has absorptivity, α_{ab} 80-100 % and water with thickness 100-500 μm has transmissivity, τ 0-10 %. Edalatpour and Francoeur [6] investigated the effect of thickness of thin film on its emissivity. he concluded that emissivity increases with the decrease in film thickness for metals and it decreases with the decrease in film thickness for dielectrics. As can be seen in fig. 3.14, emissivity of 0.9 brings lesser melting rate. Emissivity of 0.48 was found to bring the least deviation of submodel results from the experimental results.

As it was explained in section 3.1, some models don't consider the evaporation mass flux terms (given by eqs. 3.15) in their models and thereby ignoring the evaporative cooling at air-water interface. Fig.3.14 compares the numerical result with and without considering these mass flux terms in our submodel. It can be seen that omitting mass flux terms gives much higher melting rate with very large deviation from experimental results.

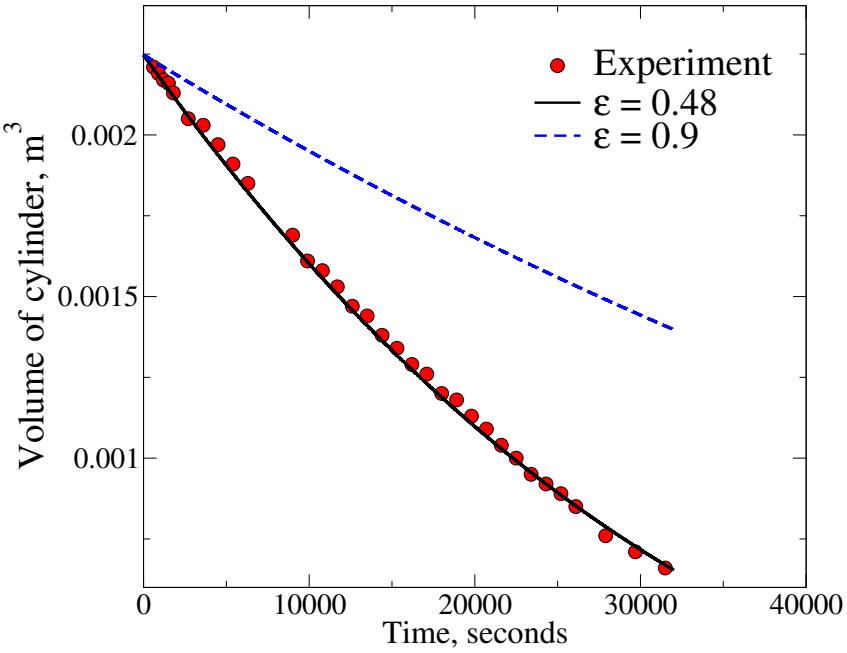

Figure 3.13: Comparison between experimental [5] results and numerical results

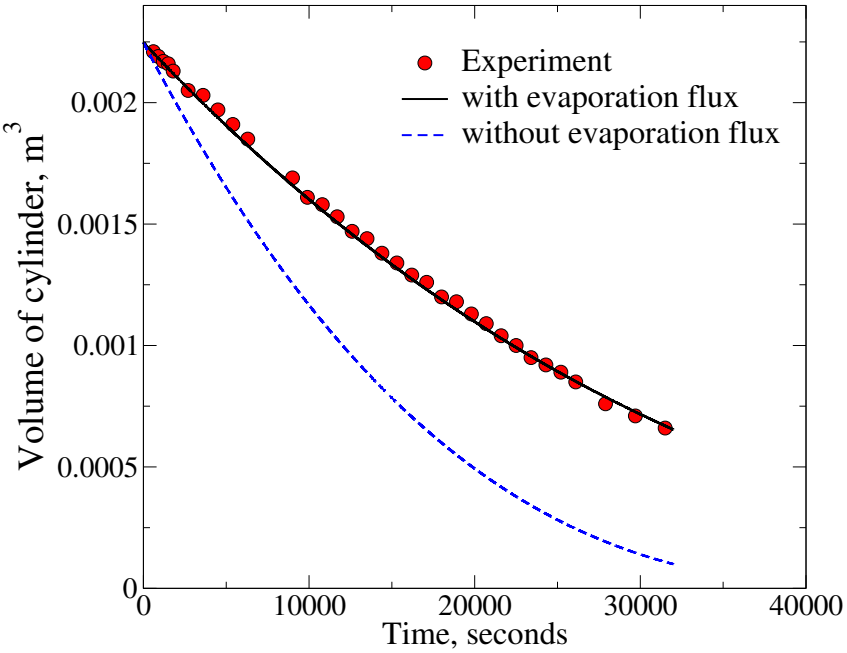

Figure 3.14: Effect of evaporation flux term on time history of volume of cylinder. Experimental results correspond to the work [5]

3.4.3 Three-phase change model for spherical particle

We conducted our own experiment for validation of submodel for spherical particle. A simple experiment of an ice sphere melting in atmospheric air was conducted. Fig. 3.15 shows the principle scheme of experiments. An ice sphere was attached to a thread through a steel hook. Other end of the thread was attached to a weighing scale placed over a wooden block as shown in the scheme. A container was kept under the hanging sphere to collect the melted liquid water. A photograph of the ice sphere during the melting is shown in fig. 3.16. Ambient air temperature and relative humidity were found to be 25^oC and 22 % respectively. Table 3.5 lists various parameters at the start of experiment. Weight of the hook was 1.4 gm. Mass of the ice sphere as recorded during the experiment is tabulated in table 3.6.

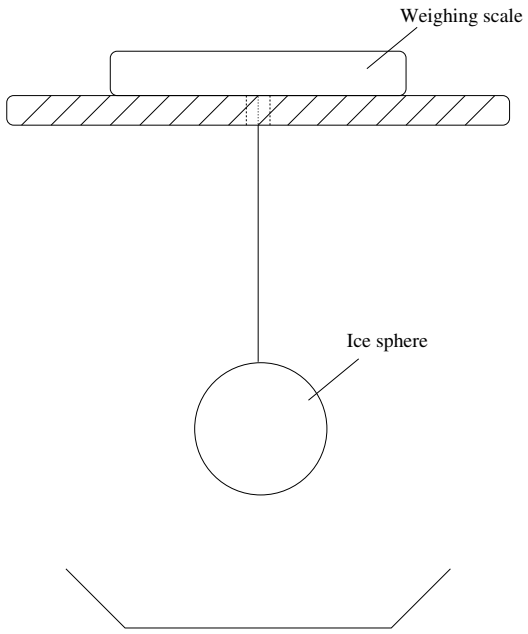

Figure 3.15: Principle scheme of own experiment [section: 3.4.3]

Table 3.5: Ice sample and air properties at the start of experiment

Ice sphere diameter, d_p	0.0559 m
Ambient air temperature, T_∞	298 K
Ambient air relative humidity, RH_∞	22 %
Ice cylinder temperature, T_p	273.15 K

The submodel provided in section 3.2 can be used to predict the radius of sphere as it melts. Similar to the validation of cylindrical particle, air next to the water

Figure 3.16: Ice sphere hanging in own experiment [section: 3.4.3]

layer is assumed to be fully saturated i.e. it has relative humidity of 100%. y_{ws} and $y_{w\infty}$ can be calculated from relative humidity values using simple mole concept. Similar to the cylindrical particle, Euler's explicit-based method with time step of 0.01 second was used to solve the Stefan boundary conditions. Lower time step values produced similar results.

Figure 3.17 compares the numerical and experimental results. Collectively, eqs. 3.1, 3.3, 3.4, 3.5, 3.7, 3.8, 3.19 are solved together to obtain the numerical results. All the thermophysical properties of air, water and ice used in the calculations correspond to the temperature values of 298 K, 273.15 K and 273.15 K respectively. Thus, table 3.4 lists numerical value of all the thermophysical properties used. Fig. 3.17 compares the submodel results and experimental results. Due to the similar reasons described in section 3.4.2, lower emissivity value (in this case 0.22) was found to give the best agreement with experimental results. As mentioned in section 3.4.2, Edalatpour and Francoeur [6] conducted an experimental study the effect of film thickness on its emissivity for various materials. Fig. 3.18 plots the experimental data for thin water film and also the two points which corresponds to our assumption of emissivity of water layer.

Table 3.6: Results obtained from the experiment on melting of ice sphere

Time, minutes	Collective weight of ice sphere and hook, gm
0	85.9
4	83.5
9	80.8
14	78.5
19	76.1
24	73.2
29	71.1
34	68
39	65.7
44	63.8
49	61.4
54	59.1
59	56.9
64	54.7
69	52.5
74	50.5

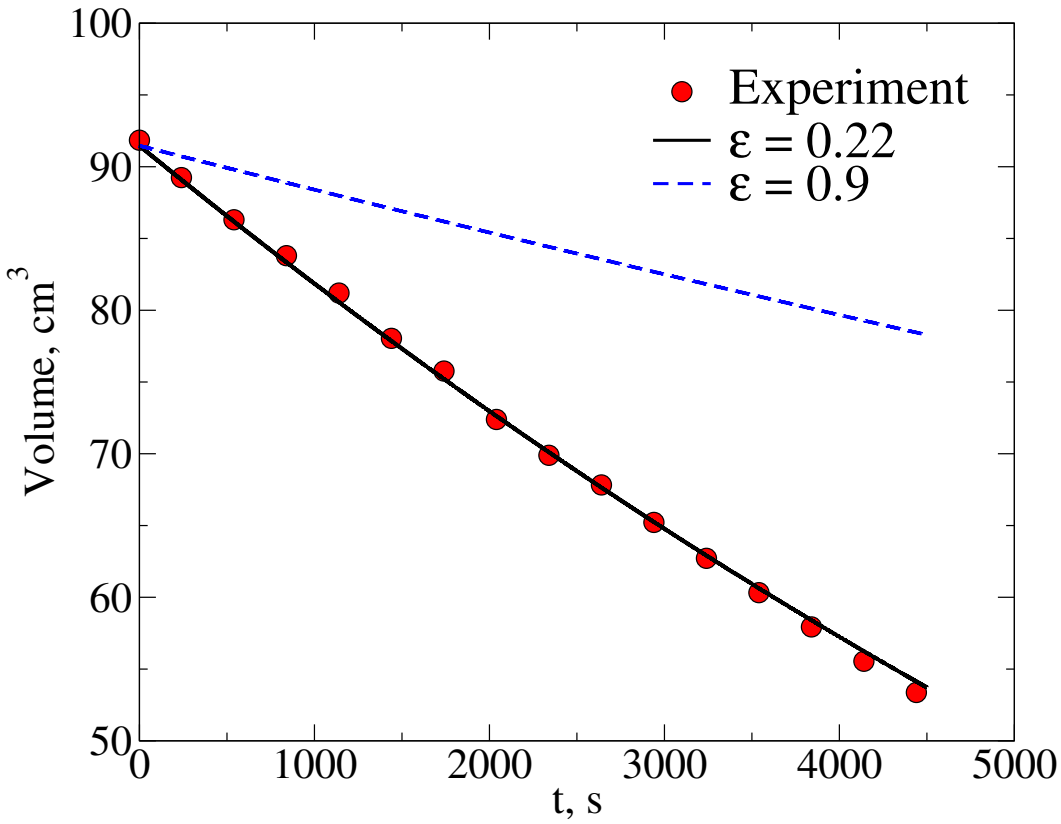

Figure 3.17: Comparison between results obtained from own experiment [section: 3.4.3] and numerical results

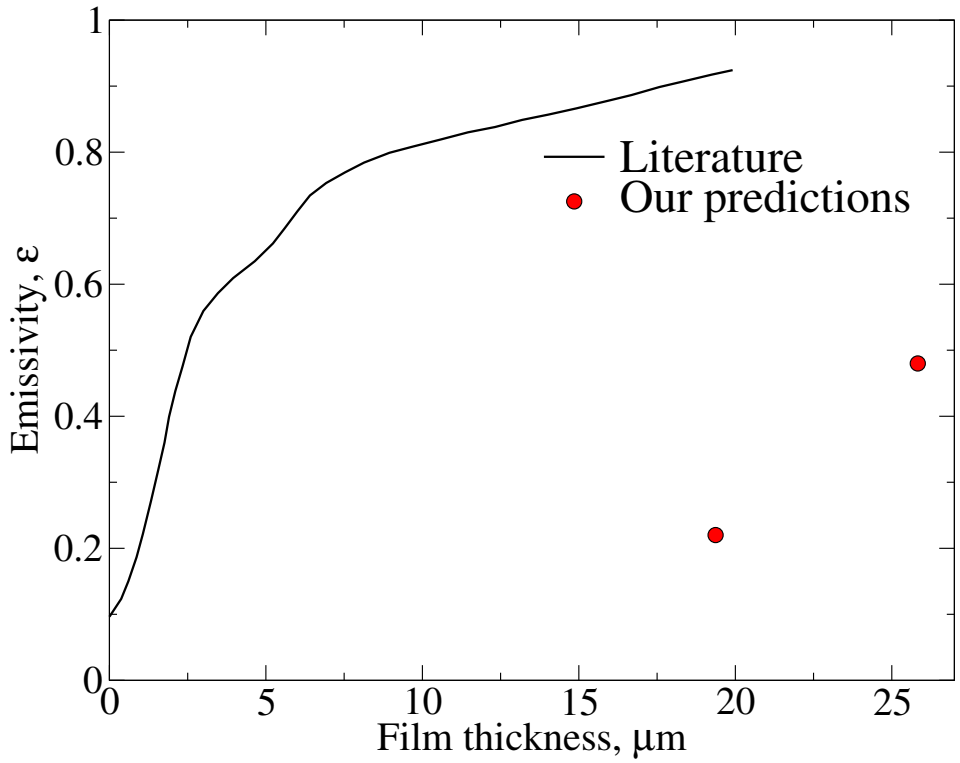

Figure 3.18: Comparison between the emissivity values reported in literature [6] and used in our calculations

3.5 Illustrations

3.5.1 Ice sphere falling in air

The submodel provided in this chapter can be used to predict the melting of ice sphere falling due to gravity in atmospheric air. Consider a single ice sphere 5000 m above the ground such that air temperature is -10^o C at this height and 25^o C at ground. Relative humidity of air is 25%. Initial temperature of particle is -2^o C. Following equations when solved together, will predict the size and temperature of ice sphere as it falls down:

Stefan boundary equation [13] on ice-water interface can be written as:

$$\rho_p h_{sf} \frac{4}{3}\pi \frac{dr_p^3}{dt} = \frac{4\pi k_l (T_m - T_l)}{1/r_p - 1/r_l} - \tau\sigma T_\infty^4 4\pi r_l^2 + \frac{4\pi k_p (T_m - T_p)}{1/r_t - 1/r_p} \tag{3.25}$$

Heat balance on water-air interface can be written as:

$$(h_c(T_l - T_\infty) + \epsilon\sigma T_l^4 - \alpha_{ab}\sigma T_\infty^4 + \dot{m}_l'' h_v) 4\pi r_l^2 = \frac{4\pi k_l (T_m - T_l)}{1/r_p - 1/r_l} \tag{3.26}$$

Evaporation flux from the water surface can be written as:

$$\dot{m}_l'' = \rho D_{lg} ln \left(\frac{1 - Y_\infty}{1 - Y_l} \right) \left(\frac{1}{\delta_l} + \frac{1}{r_l} \right) \tag{3.27}$$

where δ_l is given by:

$$\delta_l = \frac{r_l}{h_c r_l / k_\infty - 1} \tag{3.28}$$

and h_c is given by:

$$h_c = Nu_{d_l} k_\infty / d_l \tag{3.29}$$

where Nu_{d_l} is given by:

$$Nu_{d_l} = 2 + \frac{0.589 Ra_{d_l}^{0.25}}{(1 + \frac{0.469}{Pr_\infty}^{\frac{9}{16}})^{4/9}} \tag{3.30}$$

where Ra, Rayleigh number is give by:

$$Ra_{d_l} = \frac{g\beta(T_\infty - T_m) d_l^3}{\alpha_\infty \nu_\infty} \tag{3.31}$$

Fig.3.19 shows the results of the submodel for different water layer thicknesses.

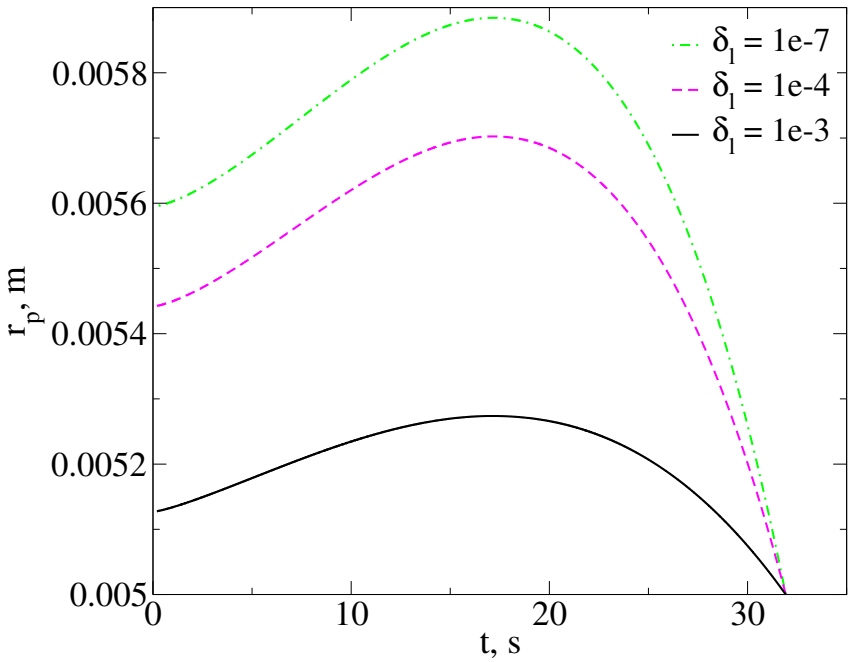

Figure 3.19: Time history of radius of sphere predicted numerically

3.5.2 Droplet solidification

Consider a drop of water falling in cold atmospheric air with subzero temperature. The submodel provided in this chapter can be used to predict the solidification process of droplet. Table 3.7 lists the initial condition of the process under consideration.

Table 3.7: Intial condition of the considered droplet solidification process

Diameter of drop	445 mm
Temperature of drop	500 mm
Temperature of ambient air	-20^o C
Relative humidity of ambient air	20%

The entire process of droplet solidification can be divided into two phases. First phase of the process would occur from time = 0 to the time when solidification of the droplet starts. Thus, the time when surface temperature of the drop reaches 0^o C would mark the end of first phase. Thereafter, second phase of the process would occur in which ice formation inside the drop takes place. In first phase, drop would lose only sensible heat whereas in second phase, drop will lose sensible as well as latent heat. The entire process can be explained numerically using following set of equations:

First phase (before start of solidification): Consider the water drop as shown in fig. 3.20. Dashed line represent the locus of surface inside sphere where the average temperature of particle T_p would exist.

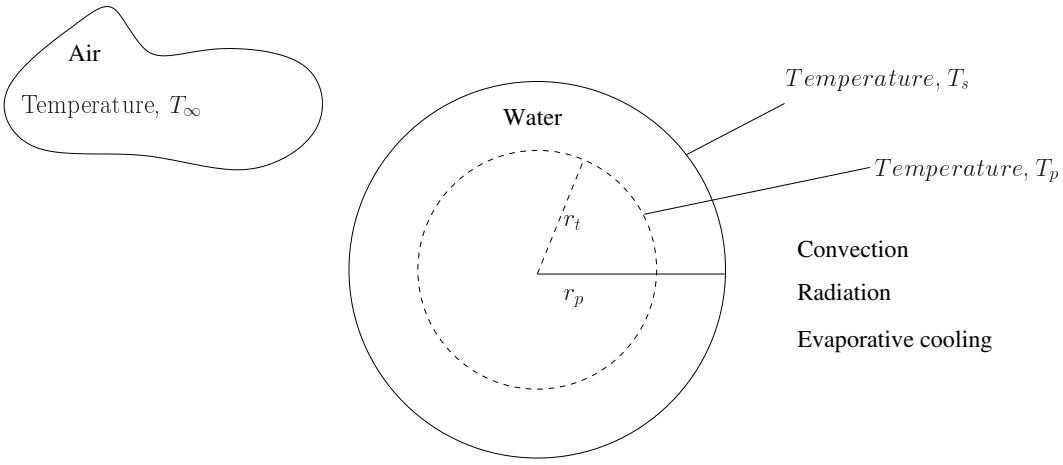

Figure 3.20: Water droplet before the start of solidification

Heat balance at water-air interface:

$$(h_c(T_s - T_\infty) + \epsilon\sigma T_s^4 - \alpha\sigma T_\infty^4 + m_s^{''} h_v) 4\pi r_l^2 = \frac{4\pi k_l (T_l - T_s)}{1/r_t - 1/r_l} \tag{3.32}$$

Heat balance inside the drop:

$$\frac{4\pi k_l (T_s - T_l)}{1/r_t - 1/r_l} = \rho v_l c_l \frac{dT_l}{dt} \tag{3.33}$$

Second phase (after start of solidification): In second phase, an ice layer would start appearing in the drop starting from its surface as shown in fig. 3.21. Since there is no water on the outer sphere of ice layer, evaporation term in surface heat balance equation will be dropped.

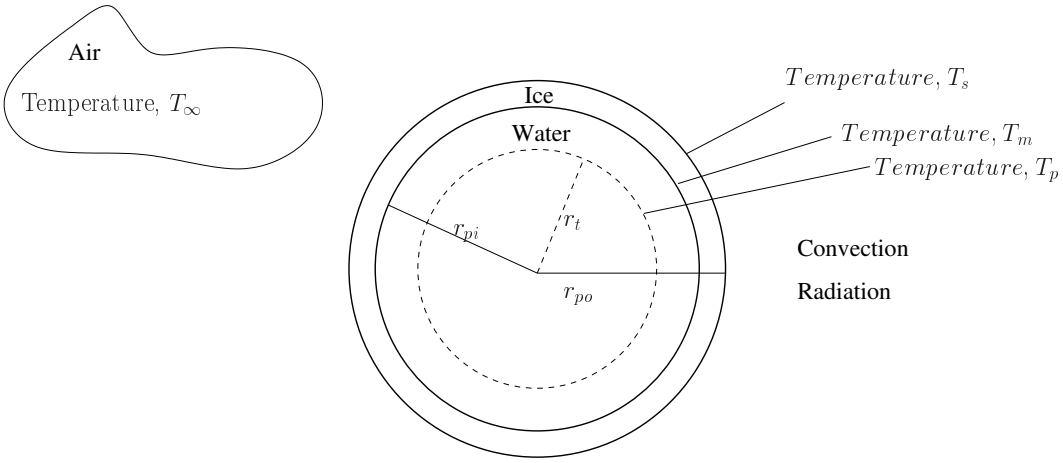

Figure 3.21: Water droplet after the start of solidification

Heat balance at ice-air interface:

$$(h_c(T_s - T_\infty) + \epsilon\sigma T_s^4 - \alpha\sigma T_\infty^4) 4\pi r_p^2 = \frac{4\pi k_p (T_m - T_s)}{1/r_l - 1/r_p} \tag{3.34}$$

Stefan BC at ice-water interface:

$$\rho_p h_f \frac{dv_l}{dt} = \frac{4\pi k_p (T_m - T_s)}{1/r_l - 1/r_p} + \frac{4\pi k_l (T_m - T_l)}{1/r_t - 1/r_l}$$

$$\implies \rho_p h_f 4\pi r_l^2 \frac{dr_l}{dt} = \frac{4\pi k_p (T_m - T_s)}{1/r_l - 1/r_p} + \frac{4\pi k_l (T_m - T_l)}{1/r_t - 1/r_l} \tag{3.35}$$

Heat balance inside the water drop:

$$\frac{4\pi k_l(T_m - T_l)}{1/r_t - 1/r_l} = \rho_l v_l c_l \frac{dT_l}{dt} \tag{3.36}$$

3.6 Conclusion

A new semi-empirical submodel for a solid particle undergoing solid-to-liquid-to-gas phase change in gas under the influence of convection has been developed. The results were in good agreement with experimental data in literature [5] and own experimental data [section: 3.4.3]. The importance of evaporation term in the heat balance on particle surface was illustrated and it was found that omitting this term results in completely different particle size predictions. Also, it was found that emissivity of water layer is significantly lower as compared to the bulk water emissivity. Finally, our submodel provided in this chapter can be used in Euler-Lagrange models to "bridge" interfacial (micro) heat and mass transfer with large-scale models used for the modeling of particulate flows where a phase change effect plays an important role. The possible applications of this numerical model include modeling in scientific fields like meteorology, material science and aerospace engineering.

Chapter 4

CFD Modeling of Ice Particles Melting in Hot Water

4.1 Introduction

In previous chapters, different zero dimensional submodels were developed and validated to predict the melting/solidification phenomena for sphere and cylindrical particles under various conditions. However, such submodel are not capable to describe the dynamics of a particle shape during it melting/solidification in a bulk flow. Only experimental studies or CFD-based modeling are able to investigate the time history of a particle shape under phase conditions. It should be noted that CFD-based simulations of phase change phenomena received recently significant attention in science and engineering due to their abilities to 'see' processes occurring on the interface between solid and liquid phases.

Basically, people use a fixed grid method solving the temperature of enthalpy equation over the whole domain including liquid and solid phases. The phase change conditions are taken into account using a source term. The velocity inside the solidified solid is damped utilizing permeability approach.

Kumar and Roy [52, 53] studied the process of melting of metal spherical particle caused by the forced convection and superheat of its own liquid. A numerical model consisting of 2D axisymmetric Navier–Stokes and energy equations was solved on fixed multi-block grid with the use of finite volume method. The simulations were carried out for material of different Prandtl numbers typically of the order of 10^{-2} which causes thick thermal boundary layers. A correlation for Nusselt number in terms of Prandtl number, Stefan number and Reynolds number was provided at the end. Wittig and Nikrityuk [54] uses the exact same numerical approach as used in this chapter. They solved 2D and 3D numerical model of melting of pure Gallium in a cuboid cavity with fixed grid and validated it against an existing experimental data in literature. The model was then used to study the effect of cuboid width on

the flow and interface location. [55] studied the melting process of solids inside the liquid metals by conducting experiments and then solving a numerical model on ice-water and frozen ethanol-water system. The numerical model was developed based on ANSYS CFD commercial software package. The influence of temperature and composition driven buoyancy and surface tension on flow structure was studied in detail. A pie-shaped domain with 5^o angle between the faces was used in the study. However, the resolution used was not good enough in the paper to fully resolve the thermal boundary layer since Prandtl number of water is around 7. Galione et al. [56] studied the effects of different strategies in 2D and 3D numerical modeling of melting of n-Octadecane inside a spherical capsule using the same numerical approach as in this chapter. The volume fraction of the liquid near the interface was calculated using mixture enthalpy. The thermophysical properties of n-Octadecane were kept constant and were varied as function of temperature in different simulations and significant difference was observed in the computational cost. 2D and 3D models resulted in different local melting rates but overall liquid fraction didn't differ much. Bourdillon et al. [57] conducted a computational study on freezing of water inside a differentially heated cavity and inside a cylindrical enclosure with constant wall temperature of -18^oC. The numerical simulations were run using open source CFD code OpenFOAM with similar model as used in this chapter. Results were found to be in good agreement with other CFD codes but no validation was provided against experimental results. Khodadadi and Zhang [58] performed numerical simulations to study the relative effects of conduction and buoyancy-driven convection on constrained melting of phase change materials utilizing the numerical approach similar to this chapter. The model was validated against experiments and then solved for materials with different Prandtl numbers and the resulting flow and melting patterns were found to be significantly different.

In this chapter, we provide an axisymmetric CFD DNS model to understand the detailed physics and behavior of the process of melting of a single particle in a liquid surroundings. An attempt will be made to obtain a dimensionless number which will be useful to predict the melting behavior of the particle. This study will help us to further improve the efficiency and the end results of this process.

Also, this chapter will help us to extend the zero dimensional formulation for arbitrary shaped solid particles. Since the experiments related to the arbitrary shaped particles involve lot of uncertainties and skepticism, there aren't many such experimental data in literature. A 2-D axisymmetric DNS CFD model, applied to the melting of spherical and cylindrical ice particle in water due to natural convection, will be provided and validated against the existing experimental data in literature.

After the validation, various parameters of the numerical model can be played with. For instance, shape and size of the ice particle can be changed and results obtained can help us extend the submodel formulation for these particles. By introducing additional shape parameters to the submodel equations, we can predict the melting process of arbitrary shaped solid particles.

4.2 Problem Formulation

To start with CFD modeling, we consider the case of melting of spherical ice particle in water [2]. A submodel for the same was provided in section 2.2.1 and validated in section 2.3.1. As explained in earlier sections, Shukla et al. [2] carried out a series of experiments involving different shapes of ice particles melting in a cylindrical container filled with water. The dimensions of the container and water level inside were as follows:

Table 4.1: Water container dimensions in experiments conducted by Shukla et al. [2]

Diameter of container	445 mm
Height of container	500 mm
Height of water level	440 mm

Water temperature was changed to three different values namely, 20^oC 40^oC and 60^oC in different experiments, keeping it constant in each run. The detailed experimental data was given only for temperatures 20^oC and 60^oC. Ice was held centrally inside the water due to which the experiment apparatus had the symmetry around the axis of cylinder. So, a two dimensional axisymmetric CFD model can be used for this process given that the cold ice melt which flows down into the water in the container, stays in laminar flow regime. In other words, if Rayleigh number stays lower than 10^8, axisymmetric model can be used. For 20^oC water temperature, Rayleigh number comes out to be $3.7\text{x}10^7$ using ice sphere radius as characteristic length. It entails cold ice melt flow would stay in laminar regime. For 60^oC water temperature, Rayleigh number takes the value of $1.725\text{x}10^9$ entailing the cold melt flow will be turbulent. So, axisymmetric model can not be used for the case of 60^oC water temperature but can be used for 20^oC water temperature.

4.3 Model Formulation

In this section, we present and explain the governing equations that need to be solved in the provided DNS CFD model. Essentially, the CFD model described below was implemented into an open source code [1], where the SIMPLE algorithm with collocated-variables arrangement is used to calculate the pressure and the velocities.

A single set of conservation equations were written for both liquid and solid phase combined. The boundary conditions at solid-liquid interface was treated using the damping terms similar to Patankar's blocking off technique [60]. Specifically, problem under consideration can be described using following set of conservation equations [61]:

$$\nabla \cdot \vec{u} = 0 \tag{4.1}$$

$$\rho \frac{\partial \vec{u}}{\partial t} + \rho \, \vec{u} \cdot \nabla \vec{u} = -\nabla p + \nabla \cdot \left(\mu \cdot \left(\nabla \vec{u} + (\nabla \vec{u})^T \right) \right) + \vec{F}_B + \vec{F}_{IB} \tag{4.2}$$

$$\rho \, c_p \frac{\partial T}{\partial t} + \rho \, c_p \, \nabla \cdot (\vec{u} \, T) = \nabla \cdot (\lambda \nabla T) - \rho h_{sf} \frac{\partial \varepsilon}{\partial t} \tag{4.3}$$

$$\varepsilon = AMIN \left(1, \, AMAX \left[0, \, \left(\frac{T - T_m}{\delta_T} \right) \right] \right) \tag{4.4}$$

where ε is volume fraction of liquid in the given cell, δ_T is phase-change thickness, a free parameter which can take value according to the grid size and desired numerical stability. More details about various other terms will be provided later in this section.

Following assumptions have to made to use the above mentioned equations:

- Flow of the liquid phase is axisymmetric.
- Interface cells are treated as a mushy zone represented by porous media approach.
- Walls of the cylindrical container are adiabatic.

4.3.1 Grid

Fixed structured non-body fitted Euler grid was used in the simulations. Entire domain was split into 450 cells in the radial direction and 900 cells in the axial direction with total of 450x900 = 405000 cells. Grid size of 300x600, 320x640,

[1] An open source CFD code of a 2D Navier– Stokes solver [59] was adopted to model particles melting, see the book [59] how to download this open source code.

350x700 were also tried with the CFD code but all these coarser grids resulted in poor resolution of boundary layers and gave unstable solutions. The local Peclet number for some grid cells took value of During the process of melting, some grid cells in the bulk water take temperature values of higher than 20 ^{o} C which is clearly inconsistent since initial temperature of the water was 20 ^{o} C. The grid 450x900 resulted in stable solution, 3 to 4 cells in thermal boundary layer and 5 to 6 cells in momentum boundary layer and the maximum Peclet number for momentum and heat equation was 0.041 and 0.28 respectively. Time marching with a fixed time step of 0.005 second was used. Momentum equation was converged to have the residual less than 10^{-5} and energy equation was converged to the residual value of less than 10^{-4} within each time step. The maximum number of outer iterations allowed within each time step was 4000.The close up of the grid near solid particle at time = 0 is shown in fig. 4.1. Finite volume discretization scheme was used.

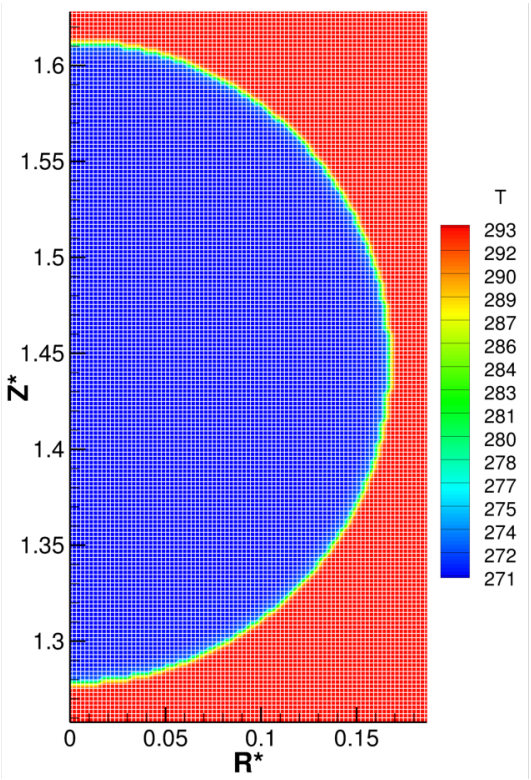

Figure 4.1: Close up of grid (white lines) near the solid ice particle; 151 cells along the diameter on z-axis

4.3.2 Discretization schemes

CDS (Central Difference Scheme) second order scheme was used to discretize the second order diffusive terms. Convective terms in the momentum equation were discretized using second order CDS with Deferred Correction and that in the temperature equation were discretized using QUICK (Quadratic upwind interpolation for convective kinematics) scheme. QUICK scheme is a third order UDS (upwind Difference Scheme) which uses two points on the upstream side and one point on downstream side thereby increasing the order of approximation [61]. On the contrary, UDS uses one point on the upstream side. The time derivatives were discretized by a three-time-level scheme using a quadratic backward approximation. Under Deferred correction scheme, cell-face value is expressed as follows [61]:

$$\psi_e = \underbrace{\psi_e^{UDS}}_{\text{implicit part}} + \underbrace{\psi_e^{CDS} - \psi_e^{UDS}}_{\text{explicit part}}$$

On converging, above equation produce pure second-order CDS on uniform grids. The system of linear equations was solved by using Stone's strongly implicit procedure (SIP).

4.3.3 Pressure-Velocity Coupling

To solve for velocities and pressure values, SIMPLE algorithm with collocated variables arrangement was used. All the velocity terms and pressure values were calculated at the center of each CV. Cell-face velocities were interpolated using the discretized momentum equation. Pressure gradient at cell face was calculated using the pressure difference between adjacent nodes. This technique of coupling pressure and velocities is known as Rhie and Chow stabilization. It erases the possibility of checker-boarded pressure field which is the primary concern in the SIMPLE algorithm when solved with collocated variables arrangement.

4.3.4 Interface Tracking

Evolution of the phase front is tracked using the eq. 4.4. In other words, temperature of the cell is used to calculate the volume fraction of liquid inside the cell. δ_T is the phase-change thickness parameter introduced to smear the phase change over a small temperature interval to attain the numerical stability. It is a free parameter which should be given a numerical value before the start of CFD simulation. Larger its value, larger will be the interface thickness. So, from physical point of view, δ_T should be given as small a value as possible but very small δ_T would result in

unstable or poorly converging solution. Fig. 4.2 explains the the impact of δ_T on CFD model. In this work, δ_t is set to be 0.1. Many test runs were carried out to find the optimum value of δ_T based on the numerical stability and interface thickness. Since δ_T is set at 0.1, volume fraction of liquid at $T = 273.1K$ will take value of 1 and at $T = 273K$ will take the value of 0. In between the two temperature values, volume fraction will vary from 0 to 1. Fig. 4.3 shows the zoomed view of the spatial distribution of the temperature and volume fraction of fluid at the solid-liquid interface.

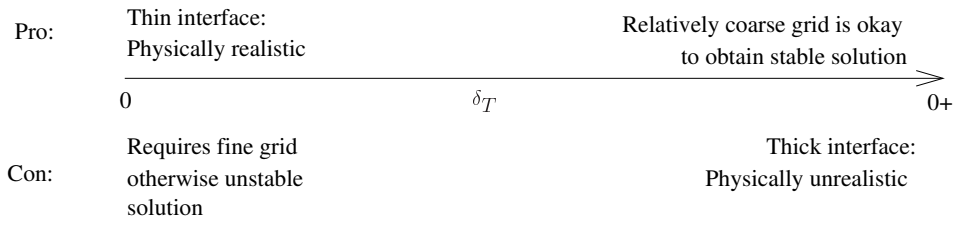

Figure 4.2: Impact of δ_T on CFD model

Damping terms

As it can be seen from the fig. 4.3, interface has some finite thickness. Due to this fact, no-slip boundary condition requires some special treatment. The solid-liquid interface cells are treated as a mushy zone or porous medium characterized by the permeability coefficient K. A common approach to the modeling of fluid flow through a porous medium is the Darcy model (in association with Kozeny-Carman equation [62, 63]) under which, coefficient K depends on volume fraction of the cells as follows: $K = K_o\varepsilon^3/(1-\varepsilon)^2$. At the same time, velocity $\vec{u}$ is damped using the similar technique as Patankar's *blocking-off* technique [60]. Taking into account these conditions, we can write following Fictitious boundary forcing term, F_{IB} [64]

$$F_{IB} = \begin{cases} -\mu\ (\vec{u})\ \ c_u \cdot \min\left(1,\ \frac{(1-\varepsilon)^2}{\varepsilon^3}\right) & 0 \leq \varepsilon < 1 \\ 0, & \varepsilon = 1 \end{cases} \tag{4.5}$$

where

$$c_u = \frac{1}{K_0} = 2 \cdot 10^4\, \Delta x_{\min}^{-1}$$

where ε is the liquid volume fraction.

So, F_{IB} is zero in the liquid regime. As soon as ε starts approaching zero from one, F_{IB} starts to increase until ε equals 0.56. Variation of the function

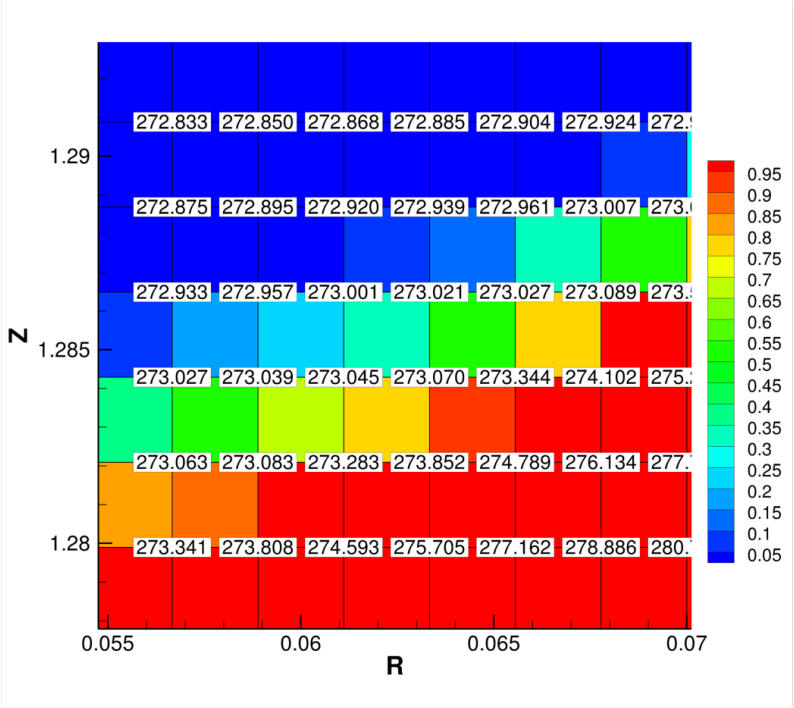

(a)

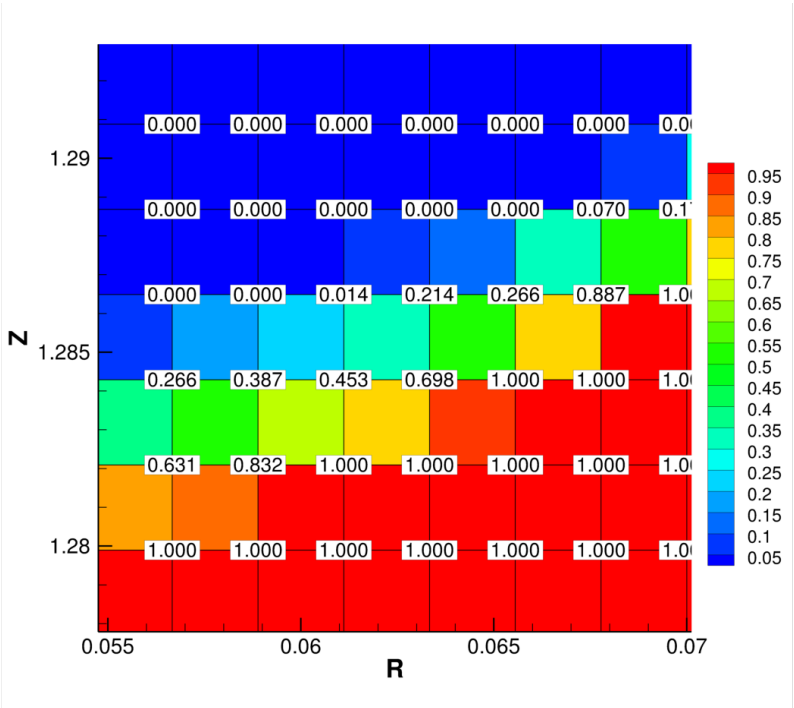

(b)

Figure 4.3: Zoomed view of the spatial distribution of the temperature and volume fraction of fluid near solid-liquid interface; (a) contour plot of volume fraction and node labels of temperature, (b) contour plot and node labels of volume fraction

"$\min(1, \frac{(1-\varepsilon)^2}{\varepsilon^3})$" is shown in fig. 4.4. Inside the control volumes occupied by the solid phase, a large magnitude of the F_{IB} forces any velocity predictions effectively to be zero. In the control volumes occupied by the liquid, this term has no consequence and usual form of the Navier-Stokes equation is assured. Due to this nature, F_{IB} is termed as "Fictitious boundary forcing term".

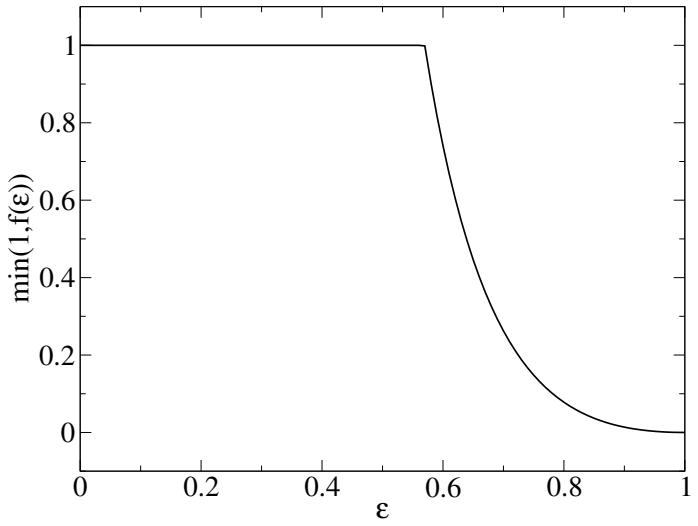

Figure 4.4: Variation of function $min(1, f(\varepsilon))$

4.3.5 Different shapes of Solid particle

As said earlier, CFD simulations are carried out for different shaped particles. The various shape profiles used are as follows:

Sphere: R = 0.037 m
Cylinder: H = 0.05 m; R = 0.04 m
Cross: W = 0.02076 m;
Sphere with bumps were created using following function:

$$r = R - A \cdot max(cos(10 \cdot \theta), 0) \tag{4.6}$$

All the variables are explained in fig. 4.5. The bump amplitude, A was varied to following four values: $R/20, R/10, R/7, R/2$.

4.3.6 Validation

This section provides the validation of CFD results for spherical and cylindrical ice particle against the experiments conducted by Shukla et al. [2]. Figures 4.6 and 4.7 shows the comparison of CFD and experimental results. The submodel results obtained in chapter 2.2 are also plotted for reference. In the experiments, radius was calculated using the planar laser-induced fluorescence technique [2]. So, essentially, maximum horizontal dimension of the ice particle was reported in the experimental results. Thus, two different radii are plotted in fig. 4.6 and among them, r_{max} (maximum horizontal dimension of the ice particle) should be compared with the experimental results. For cylindrical particle, only r_{max} is plotted. It should be noticed that CFD simulations and Submodel equations provide comparable results regardless of the fact that it took around 10 days to run the source code [59] for spherical particle and cylindrical particle each, and only few seconds took to solve the submodel equations. However, with the CFD simulations, we get detailed information about the characteristics of melt flow and melting front location which will be explained in section 4.4. Owing to this validation, the provided CFD model can be used to predict melting process of any arbitrary shaped particle.

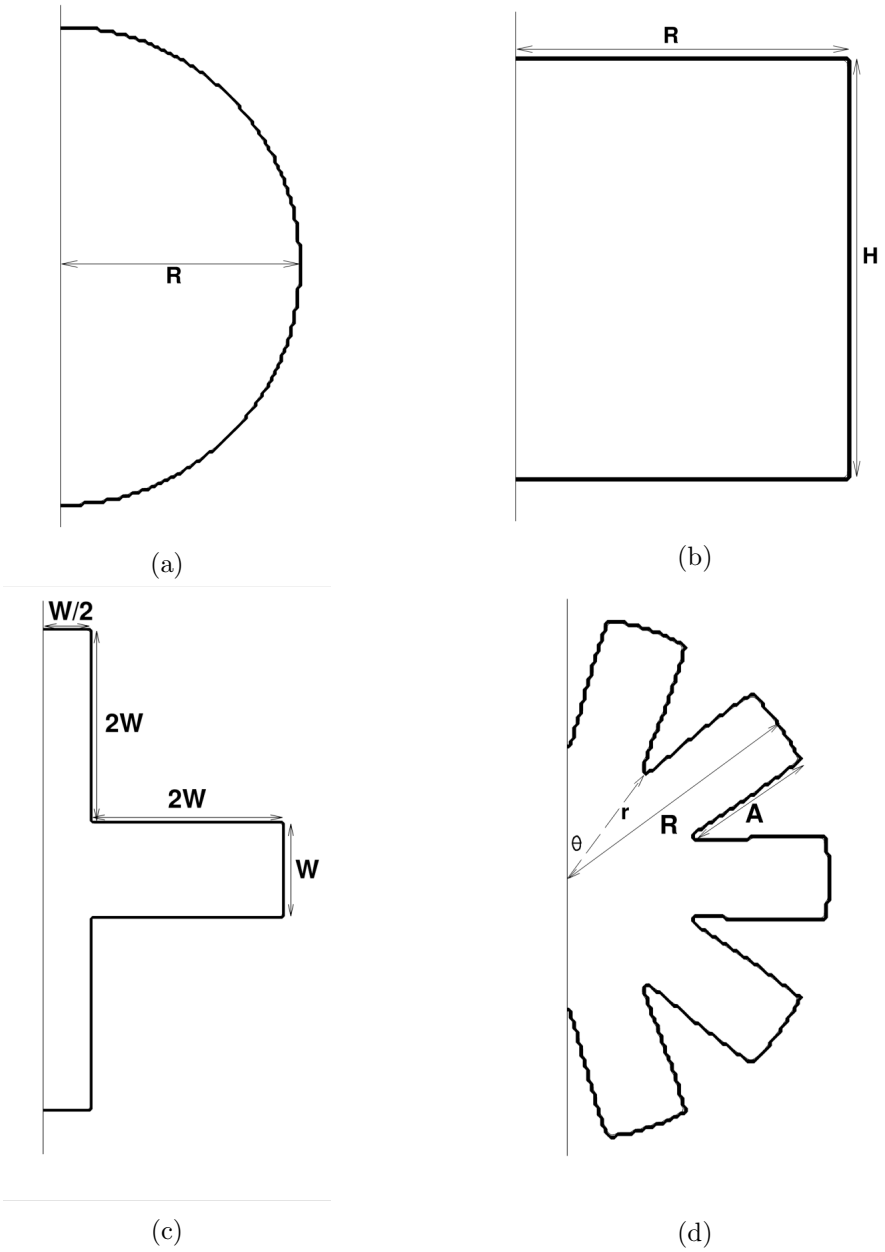

Figure 4.5: Shape parameters for (a) cross shaped cylinder; (b) sphere with bumps

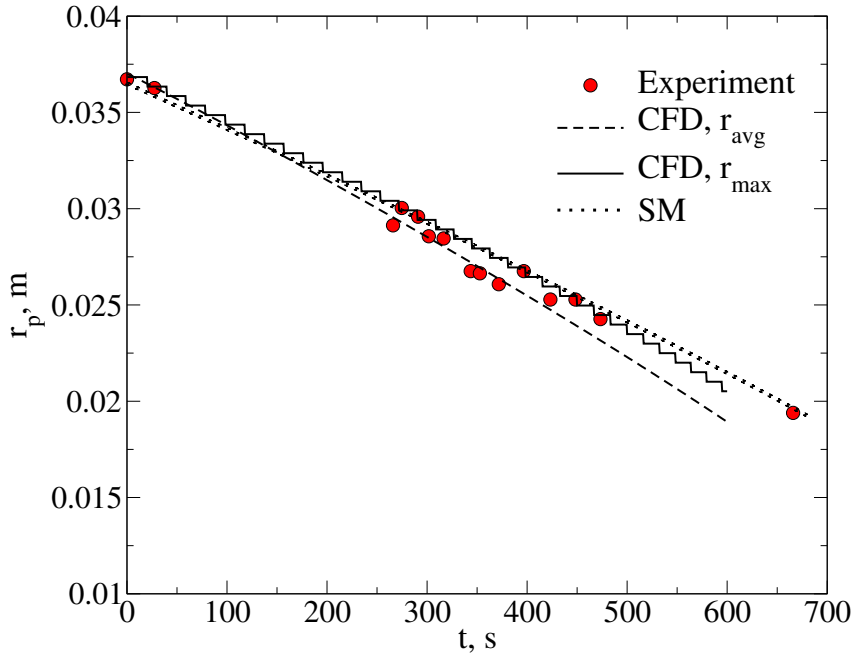

Figure 4.6: Time history of the ice sphere radius predicted numerically using CFD-based model, subgrid model and measured in experiment [2]; r_{avg} = Volume average radius of the ice particle, r_{max} = maximum horizontal dimensions of the ice particle

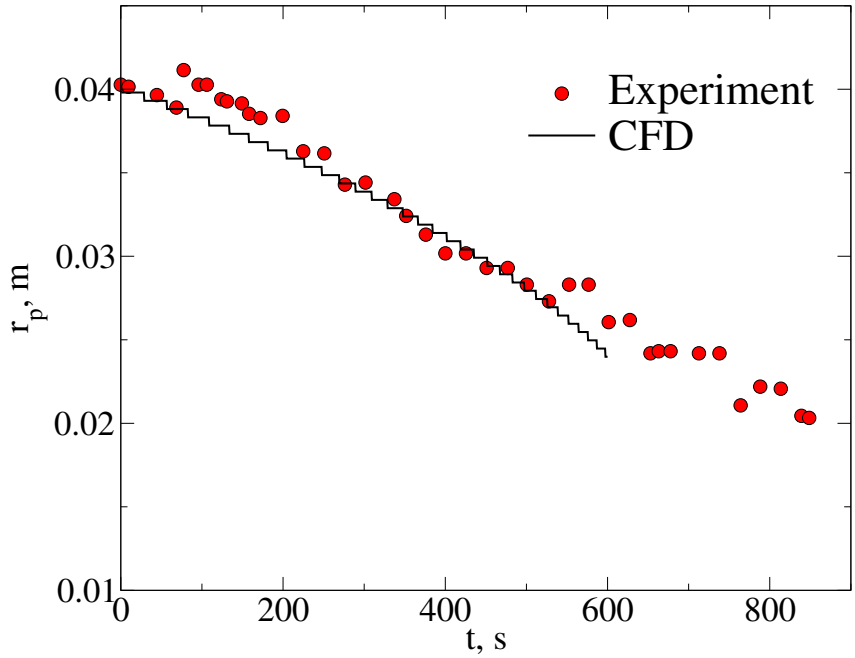

Figure 4.7: Time history of the ice cylinder radius predicted numerically using CFD-based model, subgrid model and measured in experiment [2]

4.4 Results

4.4.1 Flow characteristics/structure of cold melt

As the ice particle melts, the cold melt will flow down into the surrounding water resulting in the flow patterns in the bulk water. Cells in downstream direction of cold melt flow will have some finite velocities caused by these flow patterns. This phenomena is important in many physical processes. For instance, applications in which solid substance is to be dissolved into the liquid, intense cold melt flow will help the cold melt from solid mix faster in the liquid. To study this flow intensity, we make use of global velocities of the entire fluid in the cavity. Namely, we introduce the volume-averaged flow velocity as follows:

$$U_{rz} = \frac{2}{R_o^2 H_o} \int_0^{H_o} \int_0^{R_o} r\sqrt{u_r^2 + u_z^2} dr dz \tag{4.7}$$

where $R_o = 0.22$ m and $H_o = 0.44$ m is the radius and height of the cavity respectively. To analyze U_{rz} for different ice particles, we scale it using following parameters:

$$U_{ref} = \nu_l Gr^{1/3}/L_c; \quad t_{ref} = L_c H_o/\nu_l Gr^{1/3}; \quad Gr = \frac{g\beta(T_w - T_m)L_c^3}{\nu_l^2}$$

Here, L_c stands for the characteristic length of the particle i.e. the maximum dimension of the particle along the vertical axis. So, L_c for regular and irregular spherical particles will be the sphere radius, $R = 0.037$ m; for cylindrical particle, it will be $H = 0.05$ m and for cross shaped particle, $5W = 0.1038$ m. Variation of the dimensionless volume average velocity, based on the scale parameters introduced above, for different shapes of ice particle is shown in fig. 4.9.

Interestingly, all the plots show a rapid rise for first few minutes after which the volume average velocity starts decreasing. This first peak occurs when the cold melt reaches the walls of cavity. Thus, it occurs nearly at same time for all the particles. Figs. 4.10a, 4.14a, 4.16a, 4.18a show the snapshots when the first peak occurs for these ice particles. Until this peak, cold melt flow exhibits many vortices. Volume average velocity keeps on increasing because simply there is nothing to discontinue cold melt flow. As size of the particle decreases, volume average velocity is expected to decrease. However, immediately after the first peak, a sharp decline in U_{rz} can be noticed for all the particles. It is because of that fact that as the cold melt reaches the cavity walls, the overall process of melting reaches a pseudo-steady state. after which it exhibits lesser number of vortices. So, volume average velocity shows a

sharp decline.

It can be seen that Cylindrical and cross shaped particle exhibits the maximum values of U_{rz} among all particles. Also, in the snapshots of CFD simulations, it can be seen that cold melt flow in case of melting of cylindrical and cross shaped particle exhibits larger number of vortices as compared to other particles. This is because of the flat horizontal surface of these two particles. For spherical ice particle, cold melt flows along its curved surface until it reaches the bottom most point of sphere. Thereafter, cold melt flow breaks into the bulk water in streamlined manner with almost no vortices. For cylindrical ice particle, cold melt can break into the bulk water at any point on its bottom surface. For this reason, volume average velocity has higher values for cylindrical ice particle as compared to spherical ice particle. The same phenomena stands true for cross shaped particle. Since cross shaped particle has more surface area along the horizontal axis, cold melt flow in this case exhibits more vortices and its U_{rz} curve lies above the curve for cylindrical particle as can be seen in fig. 4.9a.

For cross shaped cylindrical particle, curve shows a sharp decline at 230 seconds. At this time, it looses its extended cylindrical arm. So, it changes to a simple vertical cylinder as shown in fig. 4.14c and 4.15c. Thereafter, cold melt flow is essentially a streamlined flow with no vortices. On the other hand, cylindrical ice particle retains its cylindrical shape throughout the time of melting. However, it melts faster from the vertical base ends as compared to the horizontal curved surface due to which it attains the shape of circular disc as shown in figs. 4.12d and 4.13d. Since cylindrical particle has a surface along the horizontal axis throughout the entire process of melting, velocities in cold melt flow die away slowly. At 280 seconds, volume average velocity curve for cylindrical ice particle overcomes that for cross cylinder shaped particle.

U_{rz} curve for spherical particle with bump amplitude, A = $R/2$ follows the same trend as other particles. However, at 210 seconds, volume average velocity unexpectedly starts increasing. This is the result of the fact that at this time, this particle loses its big mass at the center along the vertical axis as shown in fig. 4.18b and 4.19b. Due to this sudden loss, huge cold melt flows down into the bulk water increasing the volume average velocity for a while. After a while, as particle size continues to decrease, average velocity starts decreasing again. It can be seen from the U_{rz} curves in fig. 4.9b that this temporary increase in the velocity is less dominant for spherical particles with lesser bumps.

4.4.2 Solid phase front morphology

Evolution of solid phase front in CFD simulations is explained using snapshots of temperature contour and snapshots of flow vectors (magnitude proportional to length) as shown in figs. 4.10 - 4.19. Thermal Buoyancy is the primary flow driver in all the simulations. Figures 4.10 and 4.11 shows the snapshots of CFD simulations carried out for the melting of spherical ice particle. It can be seen that towards the end of simulations, it takes the shape of ellipsoid. The different values of r_{avg} and r_{max} in fig. 4.6 also demonstrates the same. This is because of the fact that cold water melt (melted water) envelopes the bottom surface of the sphere. As ice particle starts melting, the melted water flows down along the particle surface and mixes with the bulk water. As it flows along the particle surface, it creates an envelope on the bottom surface resulting in lower temperature gradient and thicker thermal boundary layer. This causes bottom surface to melt negligibly and top surface to continue to melt. Infact, bottom surface of the sphere stays at the nearly the same location throughout the process of melting. A sharp change in the slope of solid-liquid interface at the end of simulations can be observed near the top right portion of sphere due to this non-uniform melting over the surface. Also, there aren't many vortices seen in the flow of cold melt due to the reasons explained in section 4.4.1. The flow appears to be in laminar regime. Since the flow is less intense, volume average velocity has the least values in this case among all the particles as seen in fig. 4.9a.

Figures 4.12 and 4.13 shows the snapshots of CFD simulations carried out for cylindrical ice particle. Zoomed view of velocity vector plot shows the flow characteristics of cold melt around the ice particle. It can be seen that ice particle retains it's cylindrical shape throughout the entire melting process. It melts fastest through its top surface because of the same reason as described above for the case of spherical ice particle. The cold melt can be seen enveloping the bottom surface of particle in the zoomed views of velocity vector plot. Thus, bottom surface of the cylindrical stays at the same location throughout the entire melting process. Due to this non-uniform melting, towards the end of simulation time, it attains the shape of circular disc. Since cylindrical particle has the most non-spherical shape at the end of simulations as compared to other particles, it has the maximum volume averaged velocity towards the end of simulations. In comparison to spherical ice particle, cylindrical ice particle exhibits much more vortices mainly due to the flat bottom surface as explained in section 4.4.1. Fig. 4.21 shows the variation of volume with time for different particles. For each particle, volume is divided by its initial volume. Clearly, cylindrical ice particle melts faster than spherical particle

because cylindrical particle has higher surface area per unit volume. Higher surface area results in faster melting.

Figures 4.14 and 4.15 shows the snapshots of CFD simulations carried out for cross cylinder shaped ice particle. Similar to cylindrical particle, many vortices can be seen here as well in downstream of cold melt flow. Fig. 4.21a shows that cross shaped particle melts fastest among all the particles. It has melted almost completely after t = 600 seconds. This is because of its highest surface area per unit volume. In other words, cross shaped particle is exposed to the bulk water to the greatest extent among all the particles. Fig. 4.14c and 4.15c shows the fragmentation of the extended arm of cross shaped particle. As described in section 4.4.1, this arm gets completely fragmented at 230 seconds. This results in the sudden decrease in the surface area per unit volume thereby decreasing the rate of melting as seen in fig. 4.21a. Also, after the extended arm is fragmented completely, cold melt flows along the vertical curved surface of particle and breaks away at the bottom most point. So, it doesn't exhibit any vortices thereafter.

Figures 4.16-4.19 shows the snapshots of CFD simulations carried out for spherical particle with bump amplitude, $A = R/7$ and $A = R/2$. CFD snapshots for spherical particle with bump amplitude, $A = R/10$ and $A = R/20$ are not shown here since there isn't much difference between the physics behind. As it can be seen from the CFD snapshots and fig. 4.21b, particle with higher bumps melt much faster because of its higher surface area. Also, particle with higher bumps exhibits larger number of vortices in its cold melt flow. This is because, cold melt ceases to flow along the particle surface with higher bumps. In case of amplitude $A = R/7$, it easily flows along the surface and breaks away into the bulk liquid at the bottom most point. On the other hand, in case of amplitude, $A = R/2$, cold melt flow breaks away from the surface well above the bottom most point which results in larger number of vortices. Similar to cylinder, strong jets can be seen here as well in downstream of cold melt. Also, due to its higher surface area, it has lost much more solid mass as compared to spherical particle. The particle with lesser bumps attains the spherical shape at the end of simulations whereas other particle follows completely different phase front morphology. Both the particles lose bumps at the top surface faster as compared to the bottom surface as can be seen from figs. 4.16c and 4.18c. This is caused by the thicker thermal boundary layer on the bottom surface due to the flow of cold melt.

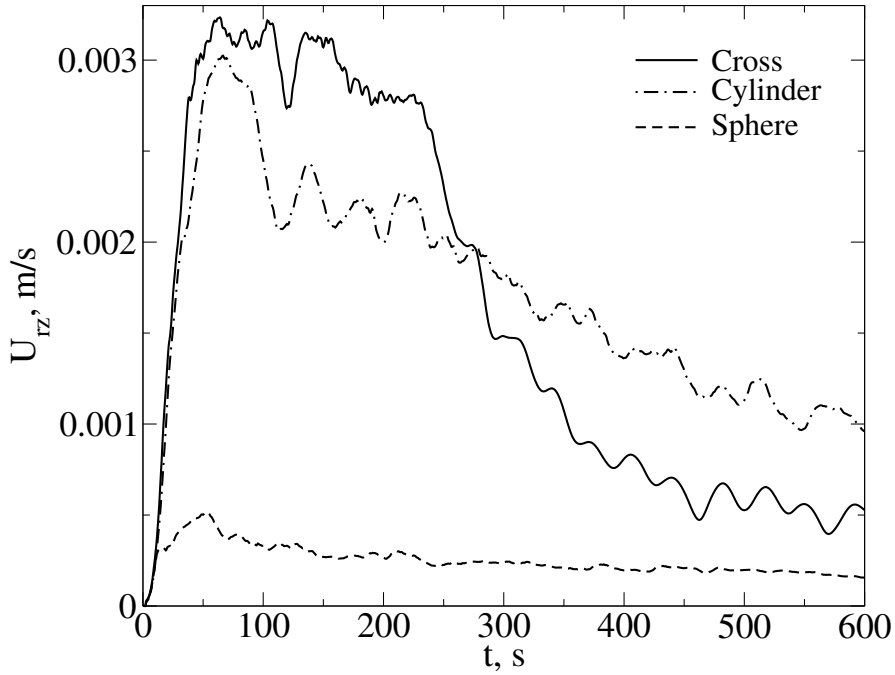

(a)

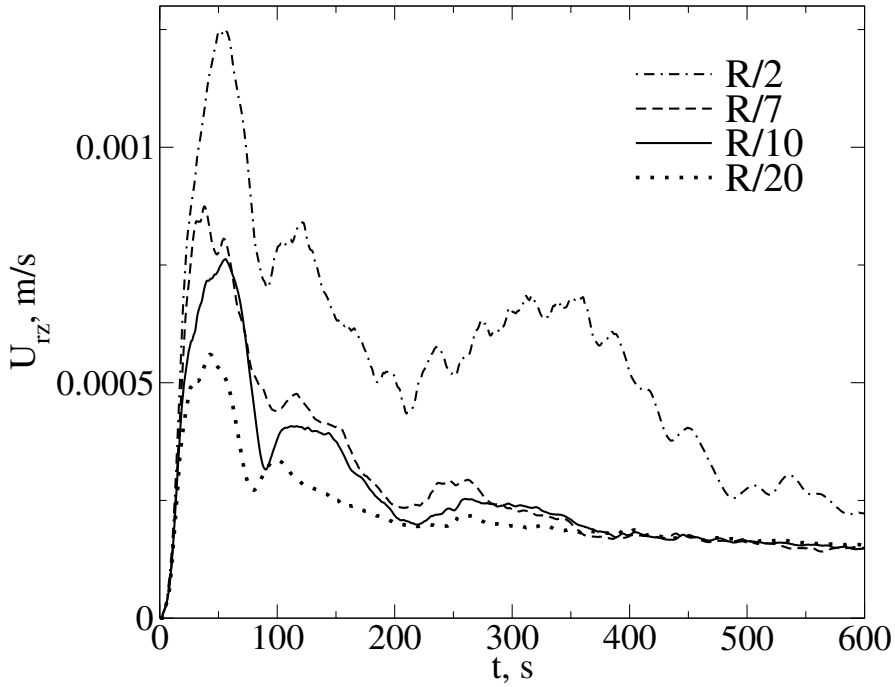

(b)

Figure 4.8: Variation of volume averaged velocity (Eq. 4.7) with time for (a) sphere, cylindrical and cross shaped cylindrical particle; (b) spherical particles with different bump amplitude (Eq. 4.6)

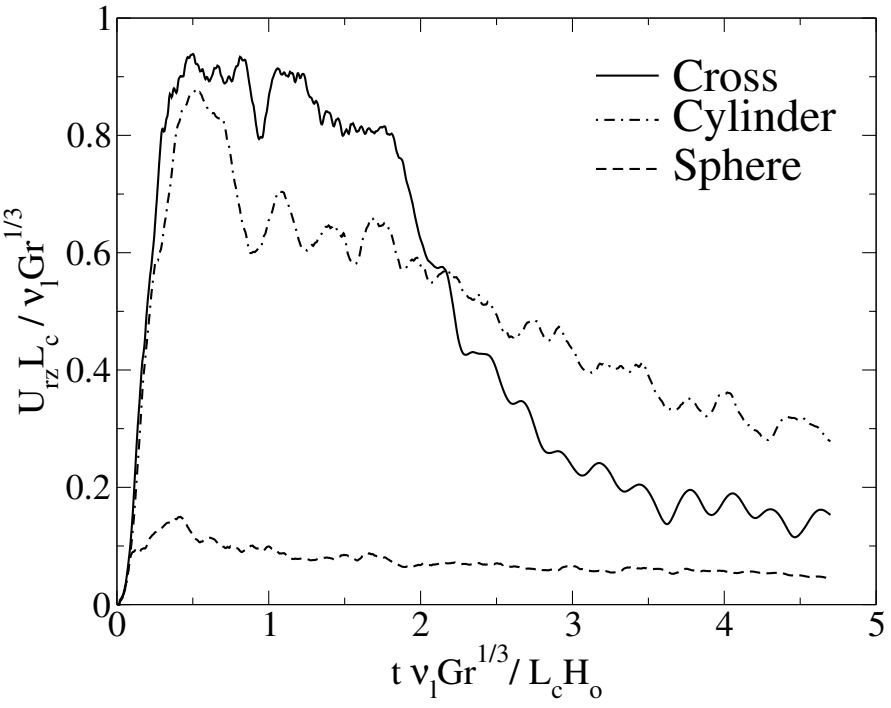

(a)

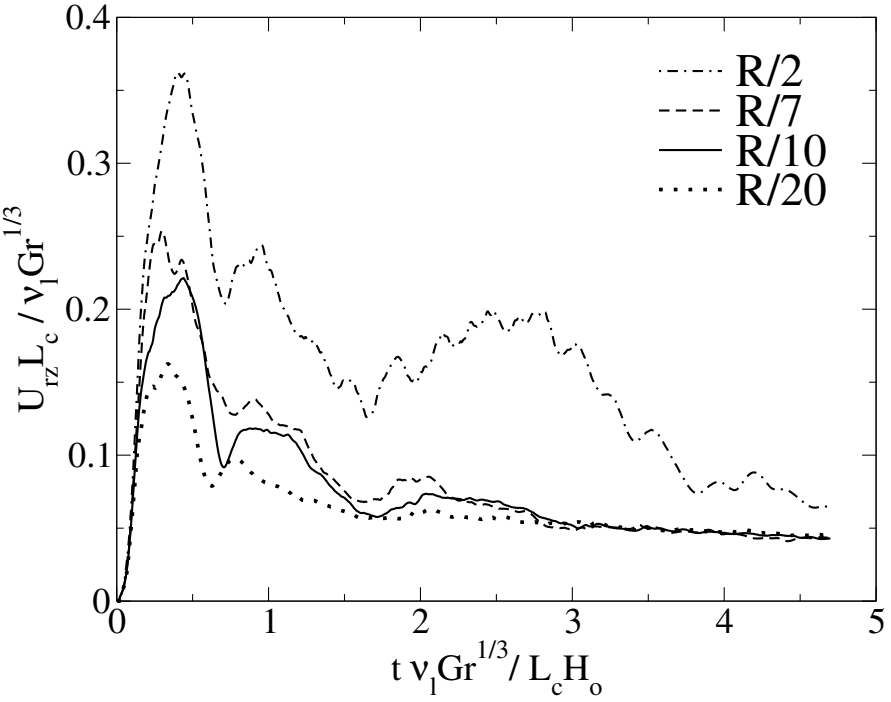

(b)

Figure 4.9: Variation of volume averaged velocity (Eq. 4.7) with time for (a) sphere, cylindrical and cross shaped cylindrical particle; (b) spherical particles with different bump amplitude (Eq. 4.6)

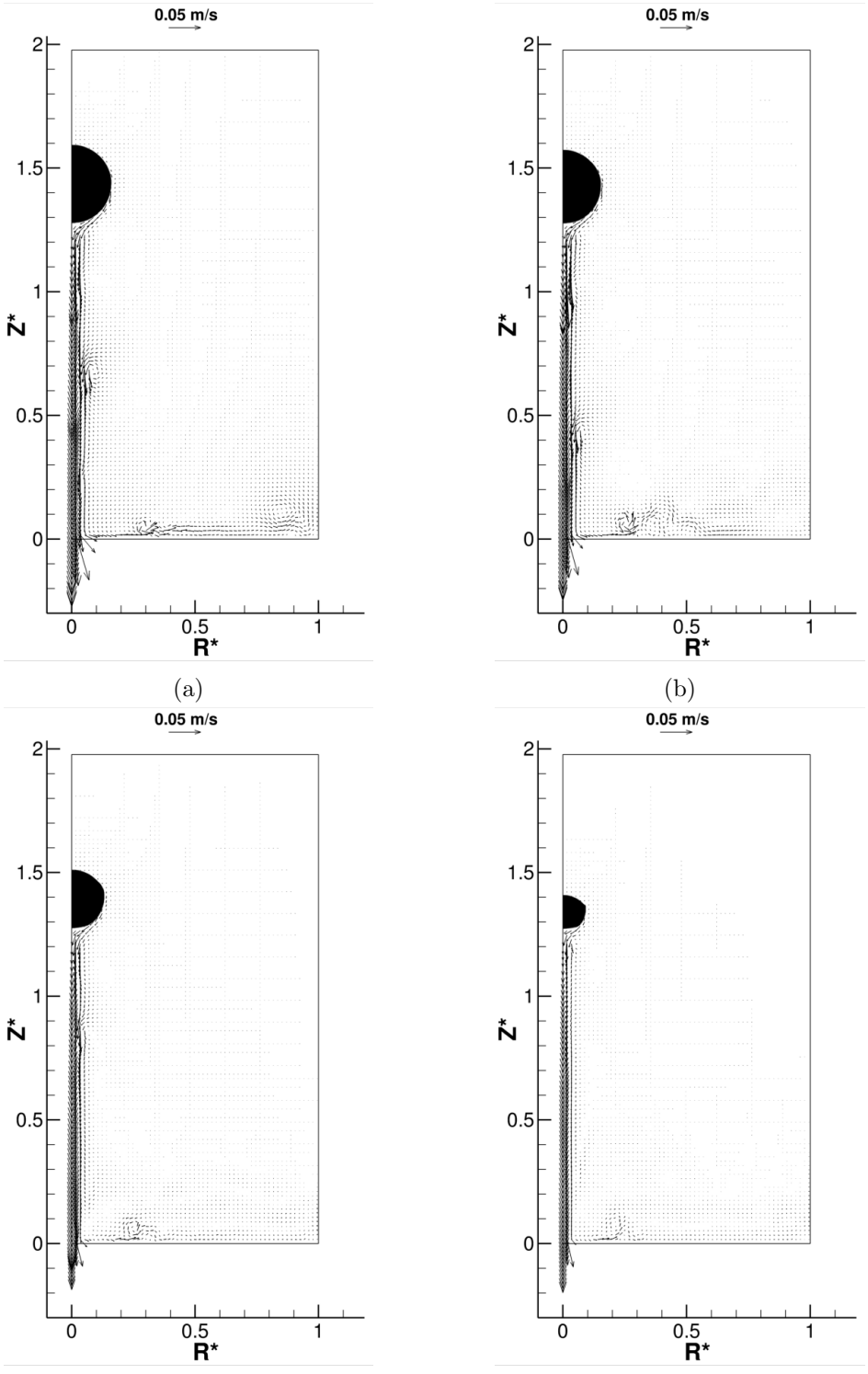

Figure 4.10: Snapshots of the vector plot of velocity at time = (a) 53.5, (b) 114, (c) 300, (d) 600 seconds predicted numerically for the case of melting of spherical ice particle

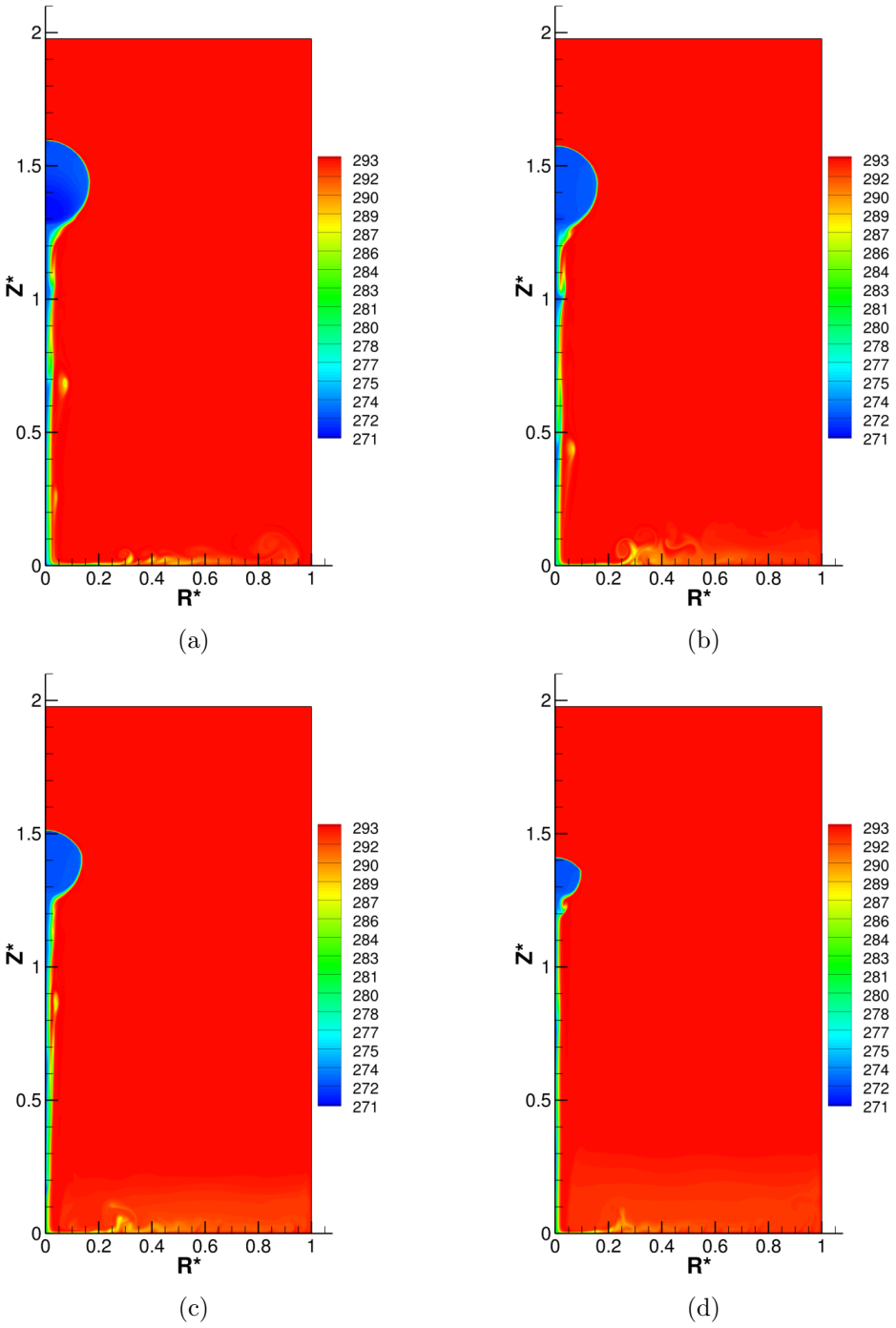

Figure 4.11: Snapshots of the contour plot of temperature at time = (a) 53.5, (b) 114, (c) 300, (d) 600 seconds predicted numerically for the case of melting of spherical ice particle

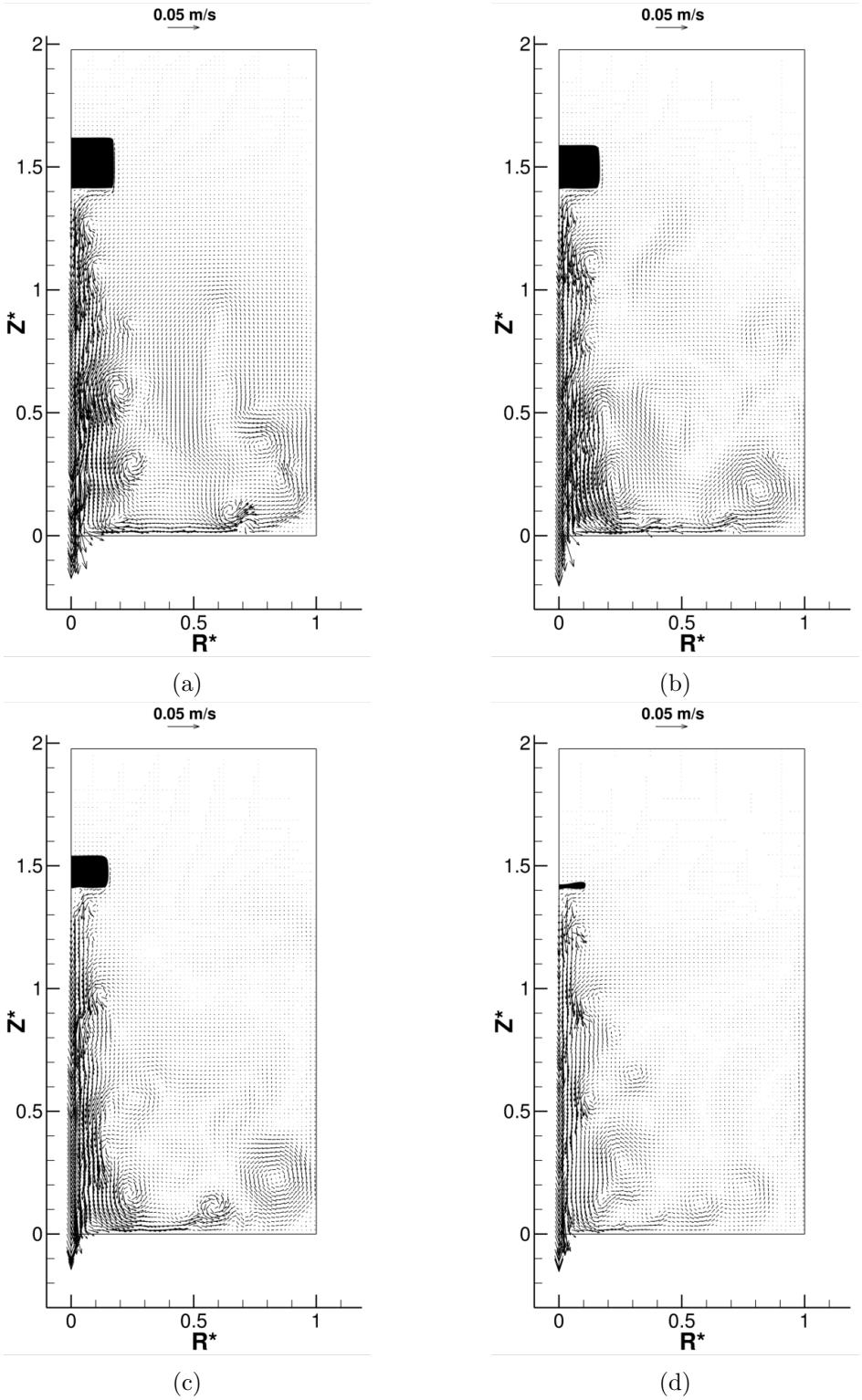

Figure 4.12: Snapshots of the vector plot of velocity at time = (a) 66.5, (b) 160, (c) 300, (d) 600 seconds predicted numerically for the case of melting of cylindrical ice particle

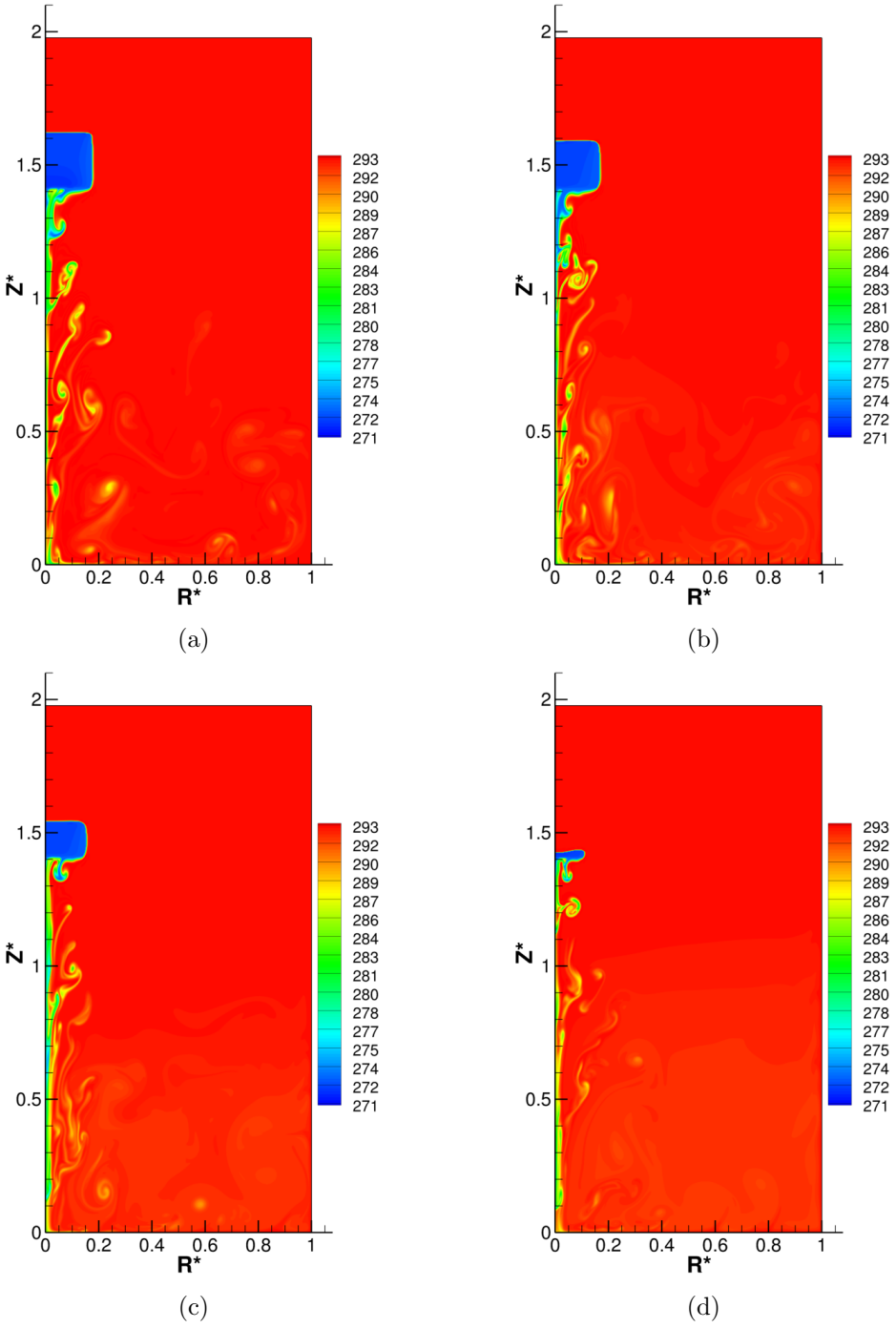

Figure 4.13: Snapshots of the contour plot of temperature at time = (a) 66.5, (b) 160, (c) 300, (d) 600 seconds predicted numerically for the case of melting of cylindrical ice particle

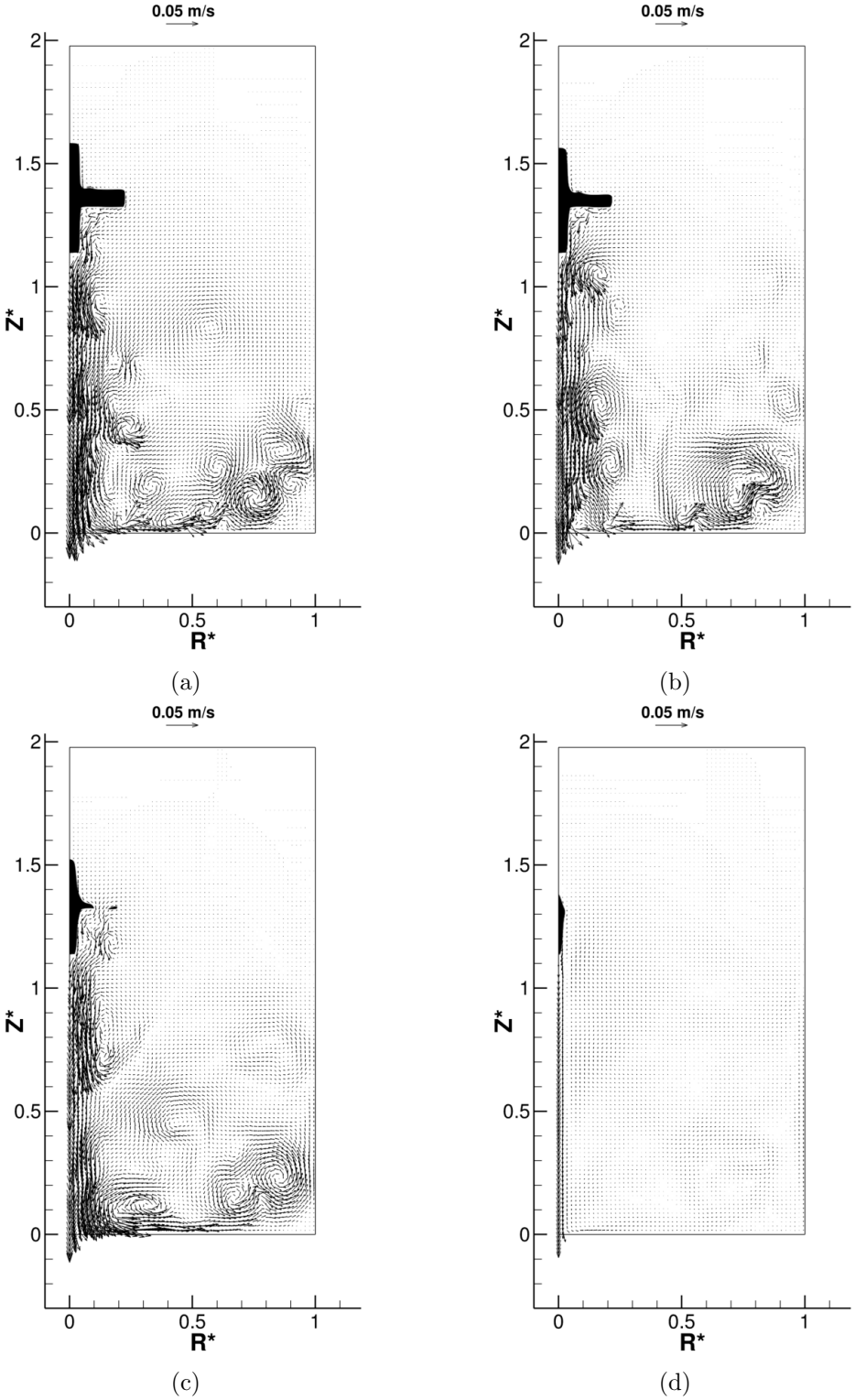

Figure 4.14: Snapshots of the vector plot of velocity at time = (a) 64, (b) 119.5, (c) 225, (d) 446 seconds predicted numerically for the case of melting of cross shaped ice particle

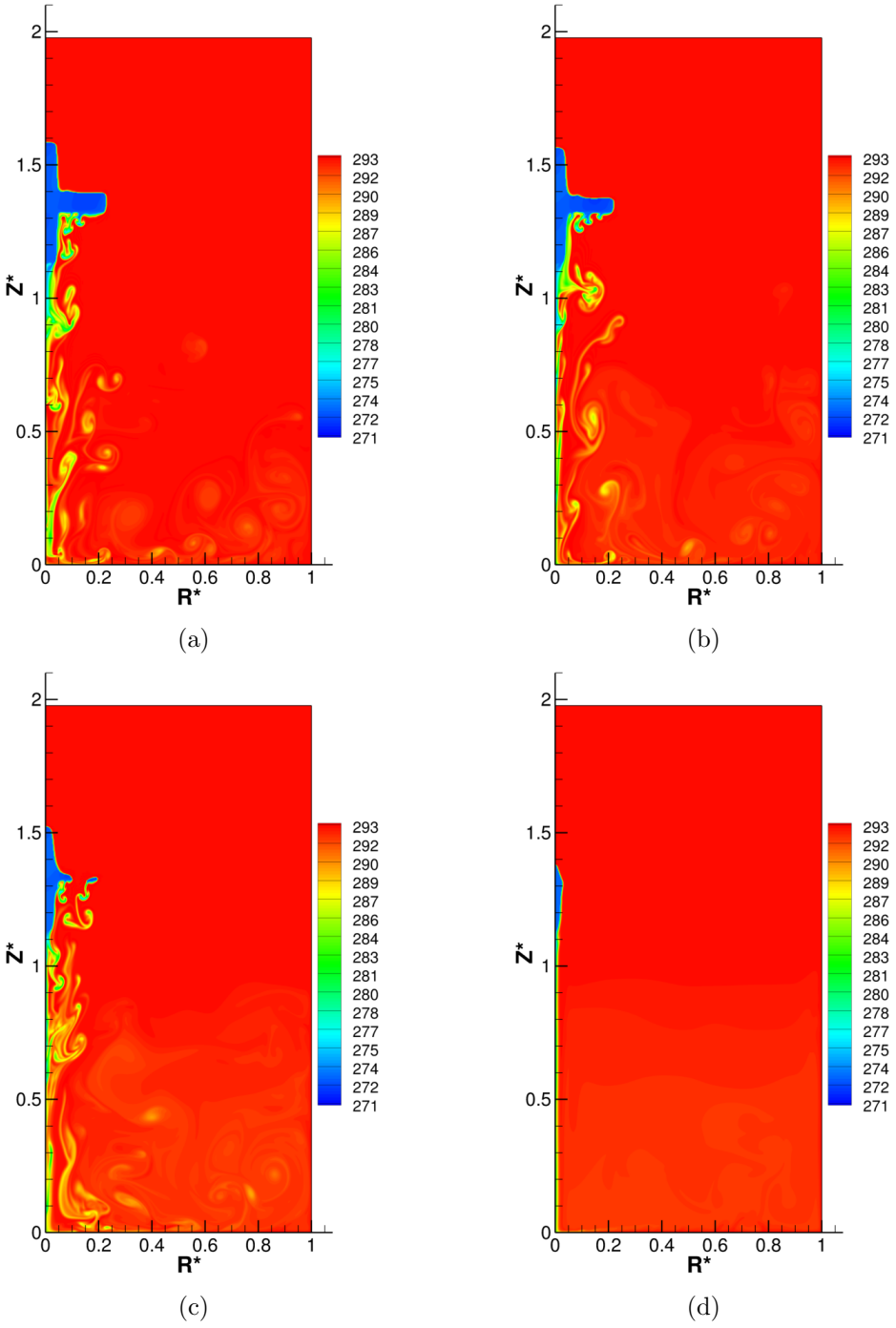

Figure 4.15: Snapshots of the contour plot of temperature at time = (a) 64, (b) 119.5, (c) 225, (d) 446 seconds predicted numerically for the case of melting of cross shaped ice particle

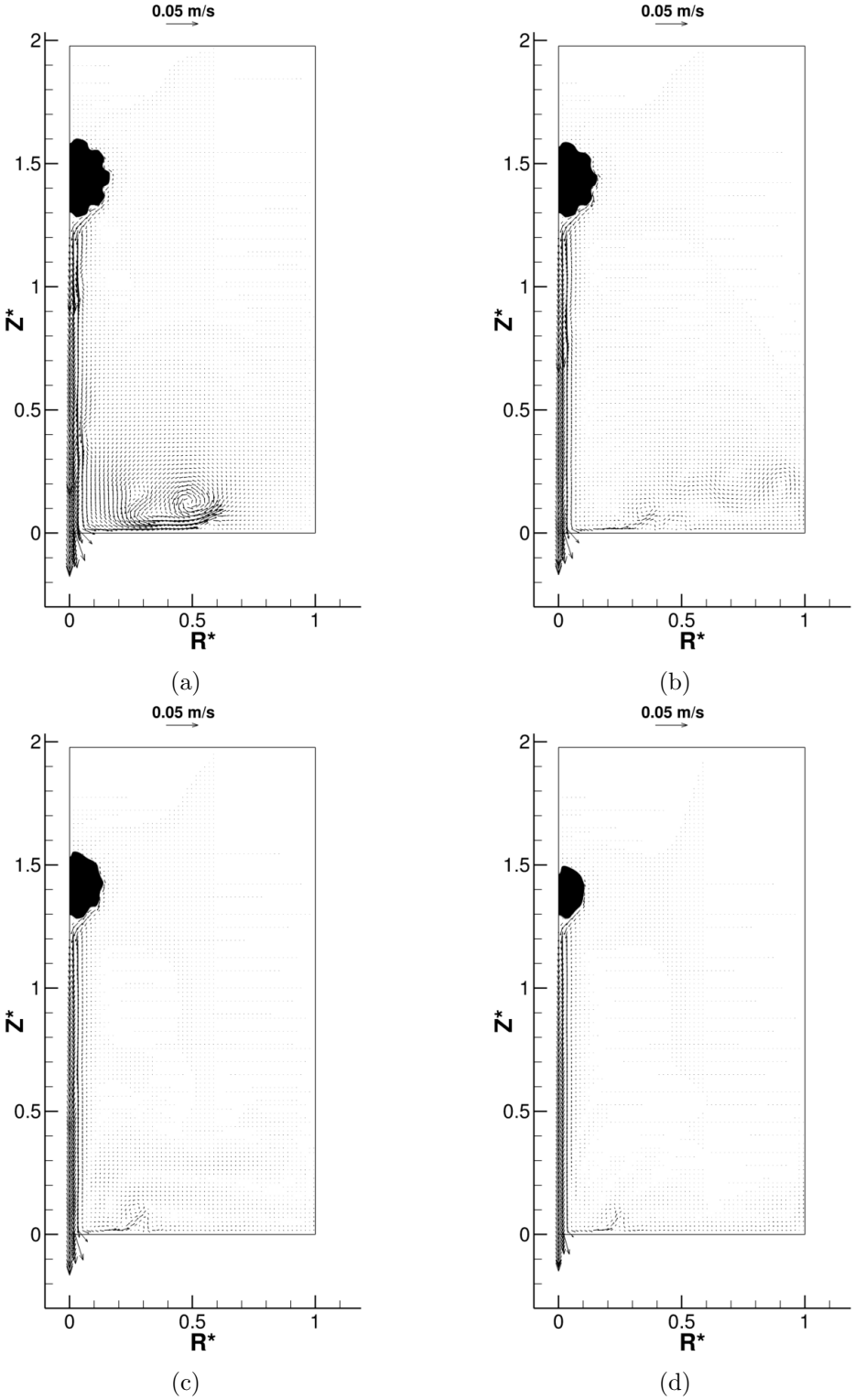

Figure 4.16: Snapshots of the vector plot of velocity at time = (a) 38, (b) 116.5, (c) 300, (d) 600 seconds predicted numerically for the case of melting of spherical ice particle with bump amplitude, $A = R/7$. See eq. 4.6

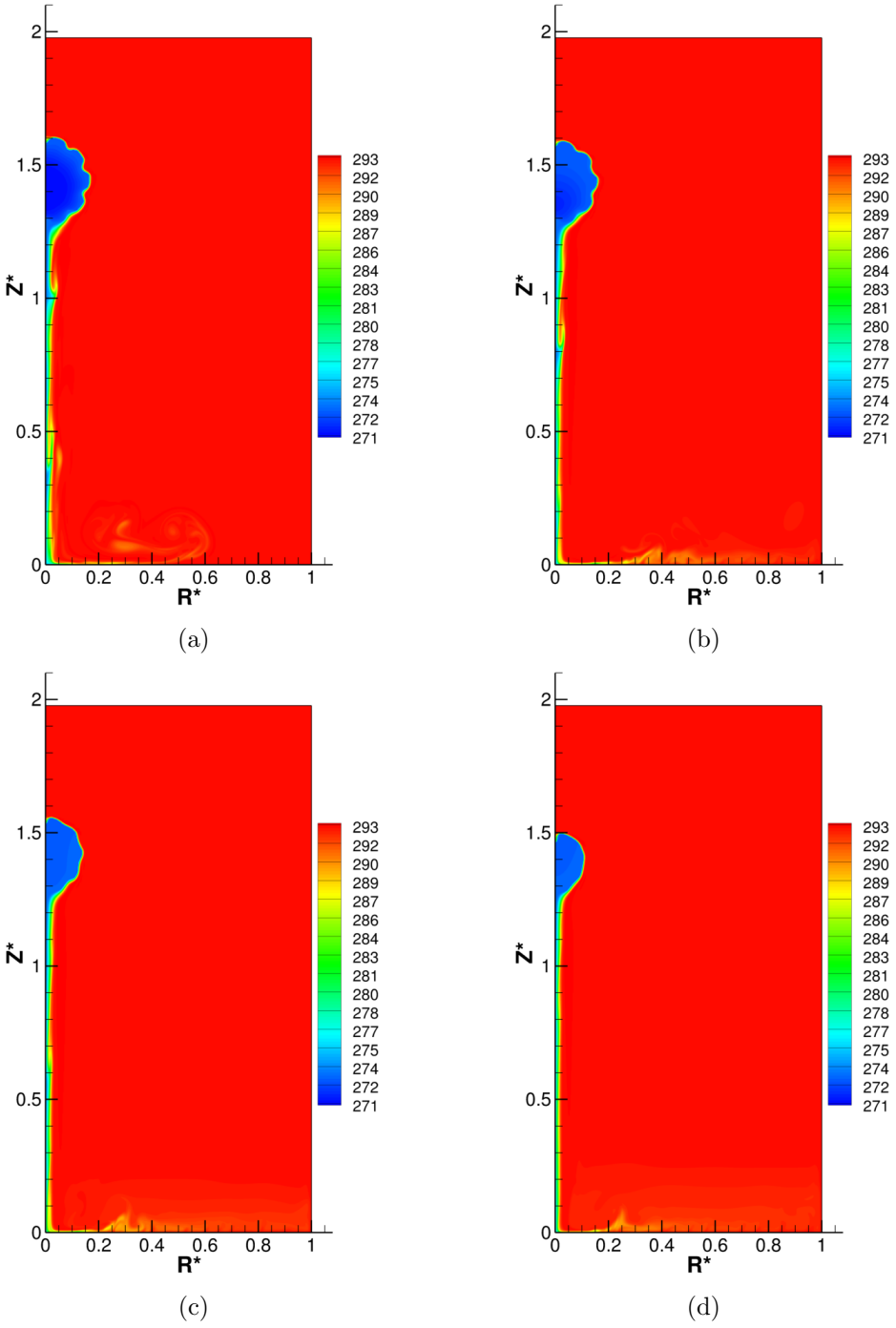

Figure 4.17: Snapshots of the contour plot of temperature at time = (a) 38, (b) 116.5, (c) 300, (d) 600 seconds predicted numerically for the case of melting of spherical ice particle with bump amplitude, $A = R/7$. See eq. 4.6

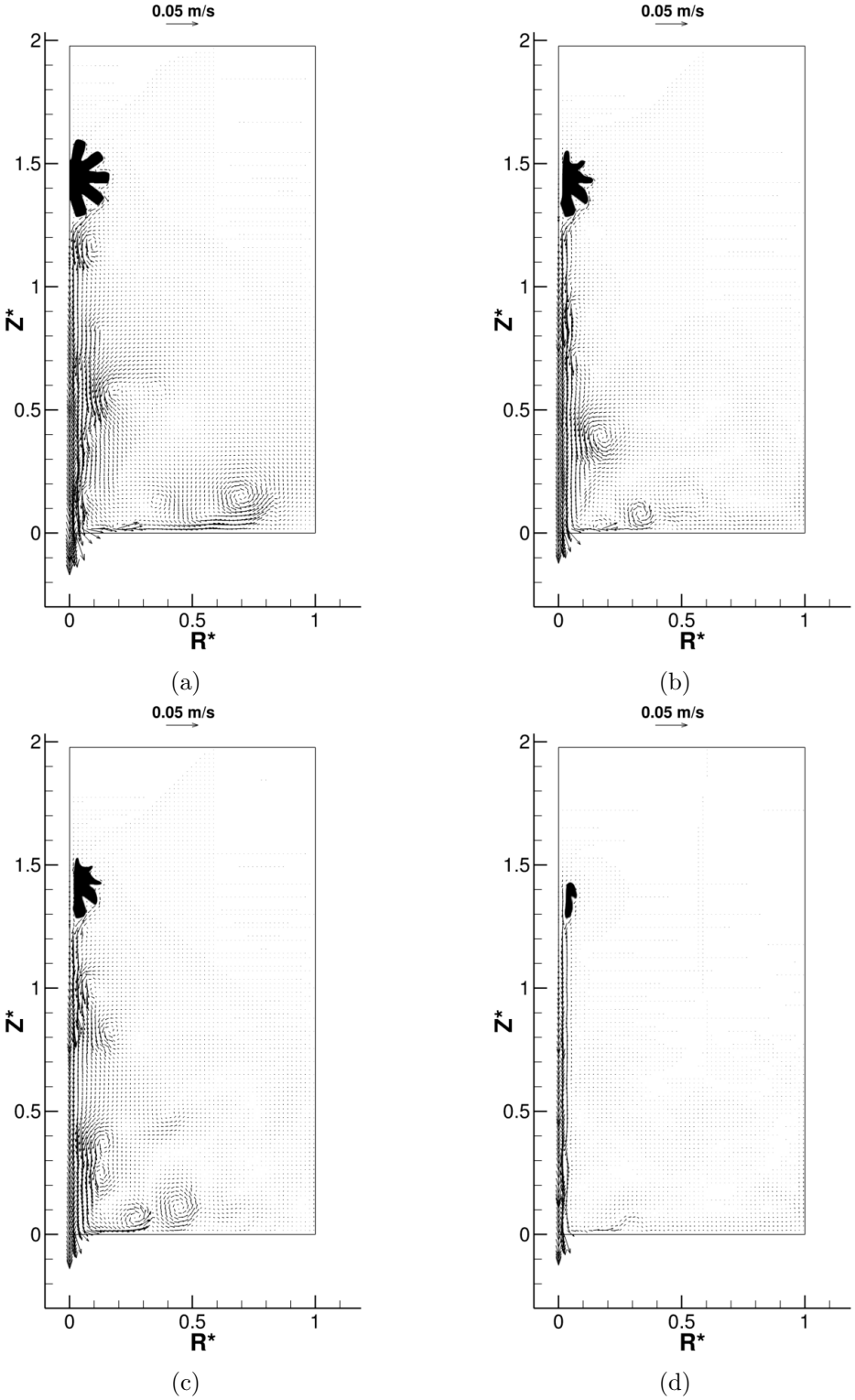

Figure 4.18: Snapshots of the vector plot of velocity at time = (a) 51, (b) 236.5, (c) 300, (d) 600 seconds predicted numerically for the case of melting of spherical ice particle with bump amplitude, $A = R/2$. See eq. 4.6

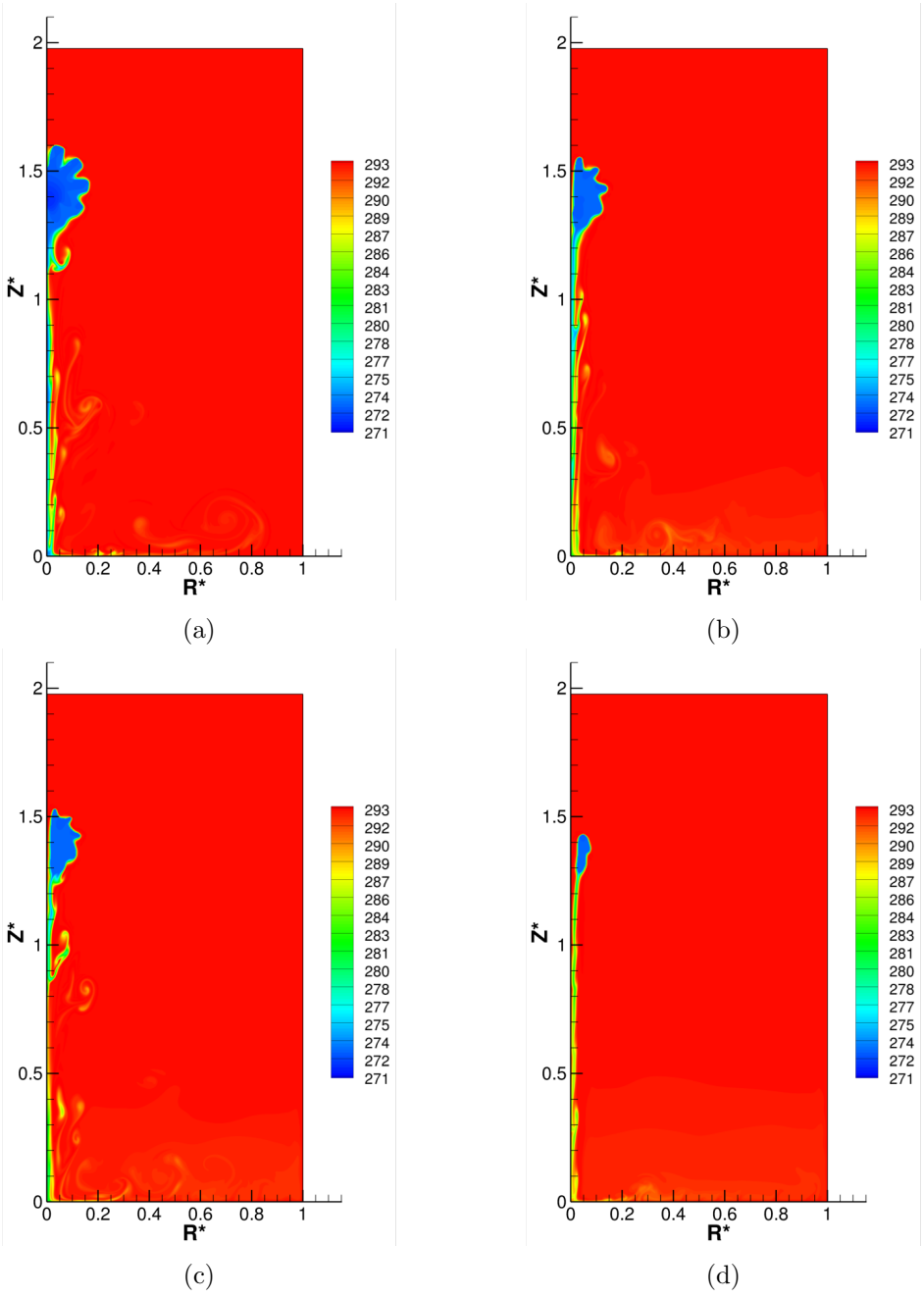

Figure 4.19: Snapshots of the contour plot of temperature at time = (a) 51, (b) 236.5, (c) 300, (d) 600 seconds predicted numerically for the case of melting of spherical ice particle with bump amplitude, $A = R/2$. See eq. 4.6

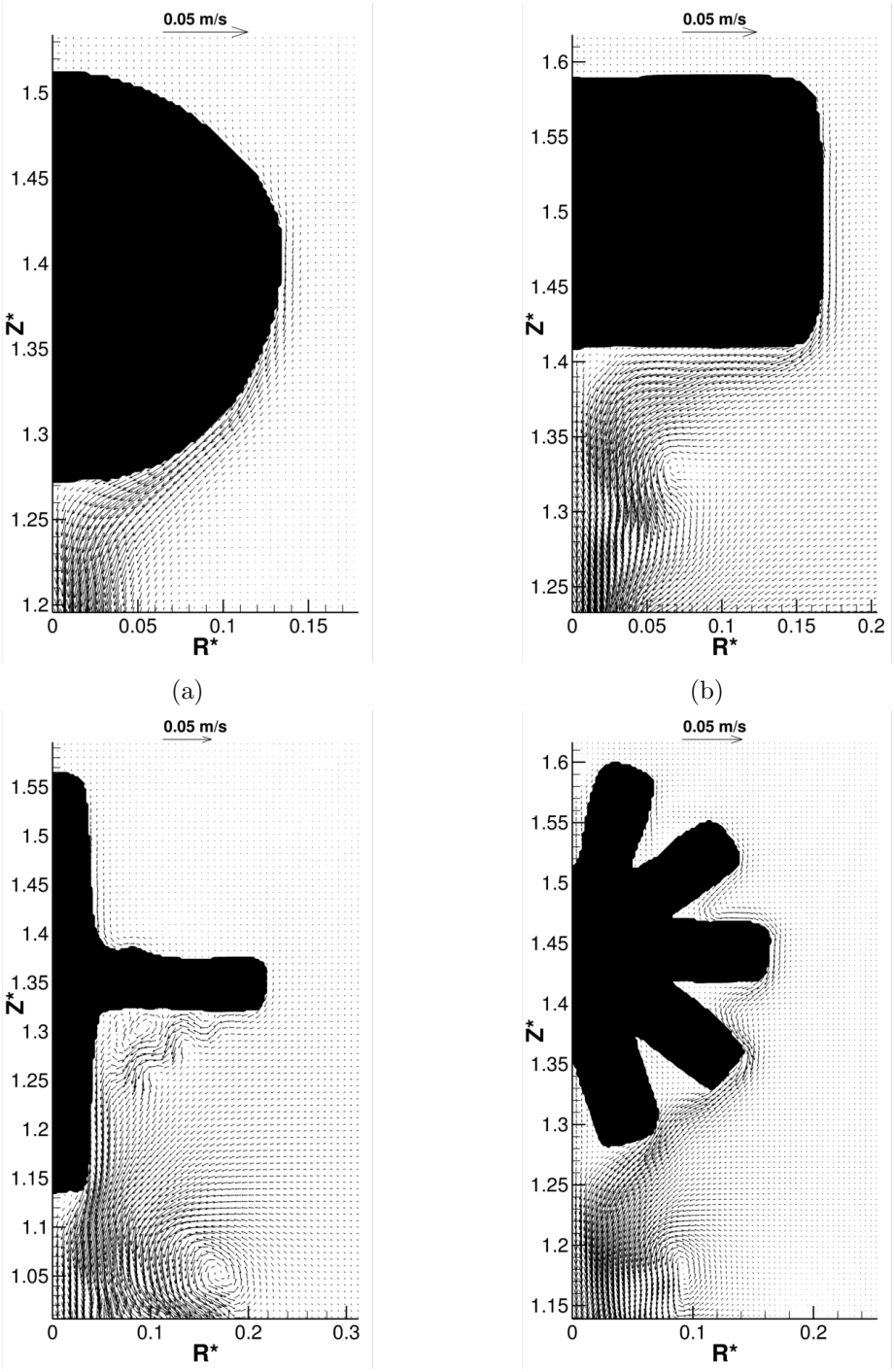

Figure 4.20: Zoomed snapshots of the vector plot of velocity at time = (a) 300 seconds for spherical particle; (b) 160 seconds for cylindrical particle; (c) 119.5 seconds for cross shaped particle; (d) 51 seconds for spherical particle with bump amplitude A = $R/2$. See eq. 4.6

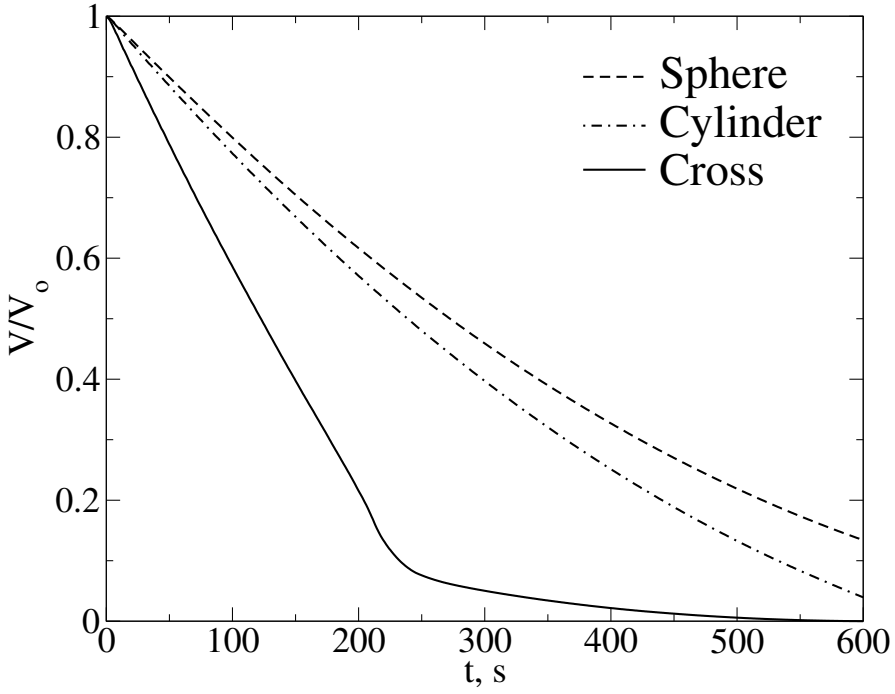

(a)

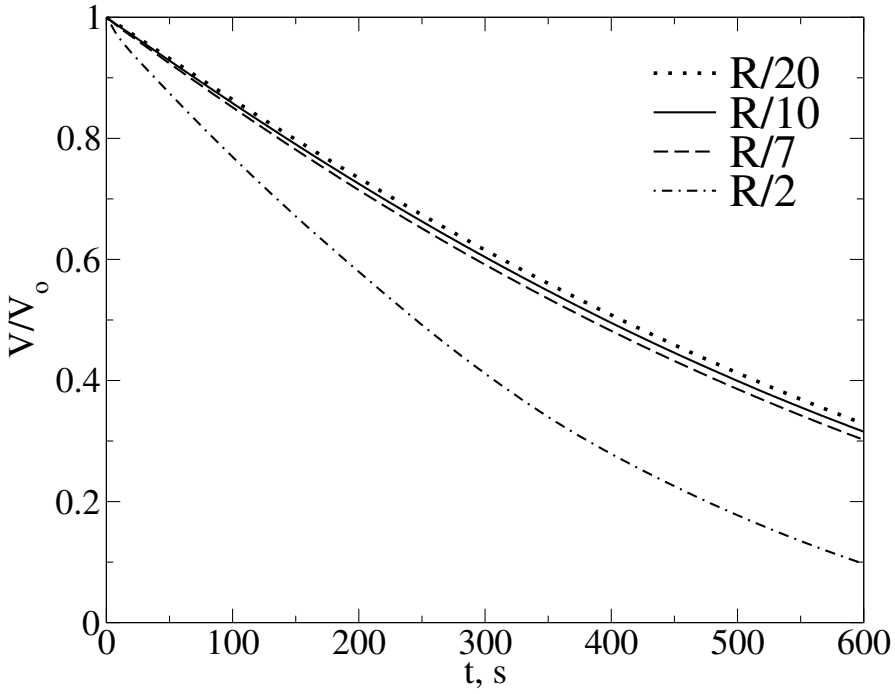

(b)

Figure 4.21: Variation of volume with time for (a) sphere, cylindrical and cross shaped cylindrical particle; (b) spherical particles with different bump amplitude (Eq. 4.6);For each particle, volume is divided by its initial volume.

4.5 Conclusions

A CFD-based model was provided to analyze the physics behind the melting process and to understand the melting process for arbitrary shaped particles. The results of the model for spherical and cylindrical ice particle were validated against the existing experimental data in literature [2] with good agreement. The provided CFD model was implemented in an open-source code [59]. Following were the main conclusions that can be drawn from the study in this chapter:

- The phase-change thickness parameter, δ_T was found to have the optimal value of 0.1 K depending upon the solid-liquid interface thickness and the numerical stability of the model.
- The grid of 450x900 cells was found to be sufficient to resolve all the major aspects of process namely the details of flow, temperature and interface location. Using the coarser grid resulted in false values of temperature. For coarser grids, few cells could be seen exhibiting the temperature values higher than 293 K i.e. higher than the initial bulk water temperature. With total 450x900 cells, 151 cells were present along the particle diameter on y-axis.
- The flow characteristics of the cold melt were studied by analyzing volume average velocity against time. Particles with the sharp edges and flat surface parallel to the x-axis exhibit higher velocities of cold melt. So, for mixing applications, those shapes are preferred.
- Cross shaped particle retained its shape till t = 213 seconds after which the extended arm in the right gets fragmented as seen in fig. 4.14c. Sphere particle with bump amplitude, A = $R/2$, gets fragmented through the center at t = 230 seconds as shown in fig. 4.18b. Sphere particle with bump amplitude, A = $R/7$, maintain the overall spherical shape throughout the melting process. However, it lost its bumps on the upper surface at t = 512 seconds thereby attaining a uniform surface with no bumps towards the end of melting time as seen in fig. 4.16d.
- The cylindrical ice particle, unlike other particles, retained its shape until the end of simulation time. Since it is the only particle at the end with a flat surface parallel to the x-axis, it has the highest volume average velocity towards the end of melting process. Spherical particle developed an ellipsoidal shape at the end as seen in fig. 4.10d.

- Particles with the highest surface area to volume ratio, lost the highest fraction of mass after 600 seconds as can be seen in fig. 4.21.
- The CFD model can be run for any arbitrary shaped particles and results obtained can be used to develop submodel equations for them. Using the some shape characteristic parameters, submodel equations provided in chapter 2 can be modified and used.

Chapter 5

Conclusions

This work attempts to develop and validate new subgrid models describing heat transfer between the bulk flow of liquid or gas and moving particles undergoing phase under the influence of forced/mixed/free convection. Specifically, in chapter 2, a new semi-empirical submodel for a particle undergoing phase change phenomena under the influence of convection has been developed. Comparison with experimental data available in the literature showed very good agreement. In particular, we showed that, applied to free convection flows, the use of the film temperature, which is an average of the bulk and surface temperature, gives better agreement with experiments compared to the use of the bulk temperature as a reference. At the same time, when applied to a forced convection or a case when free convection can be neglected, the use of bulk temperature produces results closer to experimental data. Performances of two-temperature formulations of the model are better in comparison to simple one-temperature models. Finally, our model presented in this work can be used in Euler-Lagrange models to "bridge" interfacial (micro) heat and mass transfer with large-scale models used for the modeling of particulate flows where a phase change effect plays an important role. Thus, submodels described in this chapter can be employed for the modeling of equiaxed dendrites moving under the influence of convection in the melt.

In chapter 3, a new semi-empirical submodel for a solid particle undergoing phase change in gas under the influence of convection has been developed. The results were in good agreement with experimental data. The importance of evaporation term in the heat balance on particle surface was illustrated and it was found that omitting this term results in completely different particle size predictions. Also, it was found that emissivity of water layer is significantly lower as compared to the bulk water emissivity. Finally, our submodel provided in this chapter can be used in

Euler-Lagrange models to "bridge" interfacial (micro) heat and mass transfer with large-scale models used for the modeling of particulate flows where a phase change effect plays an important role. The possible applications of this numerical model include modeling in scientific fields like meteorology, material science and aerospace engineering.

In chapter 4, a CFD-based model was provided to analyze the physics behind the melting process and to understand the melting process for arbitrary shaped particles. The results of the model for spherical and cylindrical ice particle were validated against the existing experimental data in literature [2] with good agreement. The provided CFD model was implemented in an open-source code [59]. Following were the main conclusions that can be drawn from the study in this chapter:

- The phase-change thickness parameter, δ_T was found to have the optimal value of 0.1 K depending upon the solid-liquid interface thickness and the numerical stability of the model.

- The grid of 450x900 cells was found to be sufficient to resolve all the major aspects of process namely the details of flow, temperature and interface location. Using the coarser grid resulted in false values of temperature. For coarser grids, few cells could be seen exhibiting the temperature values higher than 293 K i.e. higher than the initial bulk water temperature. With total 450x900 cells, 151 cells were present along the particle diameter on y-axis.

- The flow characteristics of the cold melt were studied by analyzing volume average velocity against time. Particles with the sharp edges and flat surface parallel to the x-axis exhibit higher velocities of cold melt. So, for mixing applications, those shapes are preferred.

- Cross shaped particle retained its shape till t = 213 seconds after which the extended arm in the right gets fragmented as seen in fig. 4.14c. Sphere particle with bump amplitude, A = $R/2$, gets fragmented through the center at t = 230 seconds as shown in fig. 4.18b. Sphere particle with bump amplitude, A = $R/7$, maintain the overall spherical shape throughout the melting process. However, it lost its bumps on the upper surface at t = 512 seconds thereby attaining a uniform surface with no bumps towards the end of melting time as seen in fig. 4.16d.

- The cylindrical ice particle, unlike other particles, retained its shape until the end of simulation time. Since it is the only particle at the end with a flat surface parallel to the x-axis, it has the highest volume average velocity

towards the end of melting process. Spherical particle developed an ellipsoidal shape at the end as seen in fig. 4.10d.

- Particles with the highest surface area to volume ratio, lost the highest fraction of mass after 600 seconds as can be seen in fig. 4.21.
- The CFD model can be run for any arbitrary shaped particles and results obtained can be used to develop submodel equations for them. Using the some shape characteristic parameters, submodel equations provided in chapter 2 can be modified and used.

Bibliography

[1] Theodore L Bergman, Frank P Incropera, and Adrienne S Lavine. *Fundamentals of heat and mass transfer*. John Wiley & Sons, 2011.

[2] Ajay Kumar Shukla, Olena Volkova, Piotr R Scheller, and Brahma Deo. Cold model investigations of melting of ice in a gas-stirred vessel. *Metallurgical and Materials Transactions B*, 42(1):224–235, 2011.

[3] Y. Hao and Y. Tao. Heat transfer characteristics of melting ice spheres under forced and mixed convection. *J. Heat Transfer*, 124:891–903, 2002.

[4] Park S Nobel. Boundary layers of air adjacent to cylinders estimation of effective thickness and measurements on plant material. *Plant Physiology*, 54(2):177–181, 1974.

[5] William S Janna and Gerald S Jakubowski. Parametric study of heat transfer to an ice cylinder melting in air. *Applied Energy*, 36(3):233–250, 1990.

[6] Sheila Edalatpour and Mathieu Francoeur. Size effect on the emissivity of thin films. *Journal of Quantitative Spectroscopy and Radiative Transfer*, 118:75–85, 2013.

[7] C_Y_ Wang and Ch Beckermann. Equiaxed dendritic solidification with convection: Part i. multiscale/multiphase modeling. *Metallurgical and materials transactions A*, 27(9):2754–2764, 1996.

[8] Andreas Ludwig and Menghuai Wu. Modeling of globular equiaxed solidification with a two-phase approach. *Metallurgical and Materials Transactions A*, 33(12):3673–3683, 2002.

[9] Menghuai Wu, Andreas Ludwig, Andreas Bührig-Polaczek, Martin Fehlbier, and Peter R Sahm. Influence of convection and grain movement on globular equiaxed solidification. *International journal of heat and mass transfer*, 46(15): 2819–2832, 2003.

[10] Andreas Ludwig and Menghuai Wu. Modeling the columnar-to-equiaxed transition with a three-phase eulerian approach. *Materials Science and Engineering: A*, 413:109–114, 2005.

[11] M Wu and A Ludwig. Modeling equiaxed solidification with melt convection and grain sedimentation—i: Model description. *Acta Materialia*, 57(19):5621–5631, 2009.

[12] M Wu and A Ludwig. Modeling equiaxed solidification with melt convection and grain sedimentation—ii. model verification. *Acta Materialia*, 57(19):5632–5644, 2009.

[13] L.I. Rubinshteĭn. *The stefan problem*, volume 27. American Mathematical Soc., 1971.

[14] Howard H Hu, Daniel D Joseph, and Marcel J Crochet. Direct simulation of fluid particle motions. *Theoretical and Computational Fluid Dynamics*, 3(5): 285–306, 1992.

[15] TI Hesla. The dynamical simulation of two-dimensional fluid/particle systems. *Unpublished notes*, 1991.

[16] Howard H Hu. Direct simulation of flows of solid-liquid mixtures. *International Journal of Multiphase Flow*, 22(2):335–352, 1996.

[17] Hui Gan, James J Feng, and Howard H Hu. Simulation of the sedimentation of melting solid particles. *International journal of multiphase flow*, 29(5):751–769, 2003.

[18] Zhaosheng Yu, Xueming Shao, and Anthony Wachs. A fictitious domain method for particulate flows with heat transfer. *Journal of Computational Physics*, 217(2):424–452, 2006.

[19] Zhi-Gang Feng and Efstathios E Michaelides. Heat transfer in particulate flows with direct numerical simulation (dns). *International Journal of Heat and Mass Transfer*, 52(3):777–786, 2009.

[20] C Dan and A Wachs. Direct numerical simulation of particulate flow with heat transfer. *International Journal of Heat and Fluid Flow*, 31(6):1050–1057, 2010.

[21] F Dierich, PA Nikrityuk, and S Ananiev. 2d modeling of moving particles with phase-change effect. *Chemical Engineering Science*, 66(22):5459–5473, 2011.

[22] MJ Andrews and PJ O'rourke. The multiphase particle-in-cell (mp-pic) method for dense particulate flows. *International Journal of Multiphase Flow*, 22(2): 379–402, 1996.

[23] J.A. Dantzig and M. Rappaz. *Solidification*. EPFL Press, A Swiss academic publisher distributed by CRC Press, 1st edition, 2009.

[24] C.Y. Wang and C. Beckermann. Equiaxed dendritic solidification with convection: Part I. multiscale/multiphase modeling. 27A:2754–2764, 1996.

[25] C.Y. Wang and C. Beckermann. Equiaxed dendritic solidification with convection: Part II. numerical simulation for Al-4wt Pct Cu alloy. 27A:2765–2783, 1996.

[26] C.Y. Wang and C. Beckermann. Equiaxed dendritic solidification with convection: Part III. comparisons with $NH_4Cl - H_2O$ experiments. 27A:2784–2795, 1996.

[27] M. Wu and A. Ludwig. A three-phase model for mixed columnar-equiaxed solidification. *Met. Mat. Trans. A*, 37:1613–1631, 2006.

[28] M. Wu, A. Ludwig, and A. Fjeld. Modelling mixed columnar-equiaxed solidification with melt convection and grain sedimentation - part ii: Illustrative modelling results and parameter studies. *Comput. Mat. Sci.*, 50:43–58, 2010.

[29] N.G. Deen, E.A.J.F. Peters, J.T. Padding, and J.A.M.Kuipers. Review of direct numerical simulation of fluid-particle mass, momentum and heat transfer in dense gas-solid flows. *Chem. Eng. Sci.*, 116:710–724, 2014.

[30] S. Tenneti and S. Subramaniam. Particle-resolved direct numerical simulation for gas-solid flow model development. *Annu. Rev. Fluid Mech.*, 46:199–230, 2014.

[31] H. Gan, J. Feng, and H. Hu. Simulation of the sedimentation of melting solid particles. *Int. J. Multiphase Flow*, 29:751–769, 2003.

[32] F. Dierich, P. Nikrityuk, and S. Ananiev. 2D modelling of moving particles with phase-change effect. *Chem. Eng. Sci.*, 66:5459–5473, 2011.

[33] C. Vanier and C. Tien. Free convection melting of ice spheres. *AIChE Journal*, 16:76–82, 1970.

[34] P. McLeod, D. Riley, and R.S.J. Sparks. Melting of a sphere in hot fluid. *J. Fluid Mech.*, 327:393–409, 1996.

[35] Y. Hao and Y. Tao. Melting of a solid sphere under forced and mixed convection: flow characteristics. *J. Heat Transfer*, 123:937–950, 2001.

[36] Y. Hao and Y. Tao. Non-thermal equilibrium melting of granular packed bed in horizontal forced convection. part i: experiment. *Int. J. Heat Mass Transfer*, 46:5017–5030, 2003.

[37] P.A. Cundall and O.D.L. Strack. A discrete numerical model for granular assemblies. *Geotechnique*, 29:47–65, 1979.

[38] H. Zhu, Z. Zhou, R. Yang, and A. Yu. Discrete particle simulation of particulate systems: a review of major applications and findings. *Chem. Eng. Sci.*, 63: 5728–5770, 2008.

[39] M. Van der Hoef, M. Van Sint Annaland, N. Deen, and J.A.M. Kuipers. Numerical simulation of dense gas-solid fluidized beds: a multiscale modeling strategy. *Annu. Rev. Fluid Mech.*, 40:47–70, 2008.

[40] C. Beckermann. Modelling of macrosegregation: applications and future needs. *Int. Materials Reviews*, 47:243–261, 2002.

[41] R. Schmidt, K. Wittig, and P. Nikrityuk. Single particle heating and drying. In P. Nikrityuk and B. Meyer, editors, *Gasification Processes: Modeling and Simulation*, pages 105–142. Willey-VCH Verlag GmbH & Co, Weinheim, Germany, 2014.

[42] W.E. Ranz and W.R. Marshall. Evaporation from drops. *Chem. Eng. Prog*, 48 (3):141–146, 1952.

[43] S.W. Churchill. Free convection around immersed bodies, 1983.

[44] Kwan-Soo Lee, Woo-Seung Kim, and Tae-Hee Lee. A one-dimensional model for frost formation on a cold flat surface. *International Journal of Heat and Mass Transfer*, 40(18):4359–4365, 1997.

[45] Kwan-Soo Lee, Sung Jhee, and Dong-Keun Yang. Prediction of the frost formation on a cold flat surface. *International journal of heat and mass transfer*, 46(20):3789–3796, 2003.

[46] BJ Murray, SL Broadley, TW Wilson, JD Atkinson, and RH Wills. Heterogeneous freezing of water droplets containing kaolinite particles. *Atmospheric Chemistry and Physics*, 11(9):4191–4207, 2011.

[47] Xiaomin Wu, Qiang Ma, Fuqiang Chu, and Shan Hu. Phase change mass transfer model for frost growth and densification. *International Journal of Heat and Mass Transfer*, 96:11–19, 2016.

[48] Ansys fluent - cfd software — ansys.

[49] Walter Viehmann and Alfred G Eubanks. Effects of surface contamination on the infrared emissivity and visible-light scattering of highly reflective surfaces at cryogenic temperatures. 1972.

[50] D Ghiasy, KVK Boodhoo, and MT Tham. Thermographic analysis of thin liquid films on a rotating disc: Approach and challenges. *Applied Thermal Engineering*, 44:39–49, 2012.

[51] D Brissinger, G Parent, and P Boulet. Experimental study on radiation attenuation by a water film. *Journal of Quantitative Spectroscopy and Radiative Transfer*, 145:160–168, 2014.

[52] Amitesh Kumar and Subhransu Roy. Melting of a solid sphere placed in an infinite medium—effect of forced convection. *Numerical Heat Transfer, Part A: Applications*, 55(6):594–609, 2009.

[53] Amitesh Kumar and Subhransu Roy. Heat transfer characteristics during melting of a metal spherical particle in its own liquid. *International Journal of Thermal Sciences*, 49(2):397–408, 2010.

[54] Kay Wittig and Petr A Nikrityuk. Three-dimensionality of fluid flow in the benchmark experiment for a pure metal melting on a vertical wall. In *IOP Conference Series: Materials Science and Engineering*, volume 27, page 012054. IOP Publishing, 2012.

[55] Jun Ou, Aniruddha Chatterjee, Steve L Cockcroft, Daan M Maijer, Carl Reilly, and Lu Yao. Study of melting mechanism of a solid material in a liquid. *International Journal of Heat and Mass Transfer*, 80:386–397, 2015.

[56] P.A. Galione, O. Lehmkuhl, J. Rigola, and A. Oliva. Fixed-grid numerical modeling of melting and solidification using variable thermo-physical properties–application to the melting of n-octadecane inside a spherical capsule. *International Journal of Heat and Mass Transfer*, 86:721–743, 2015.

[57] A.C. Bourdillon, P.G. Verdin, and C.P. Thompson. Numerical simulations of water freezing processes in cavities and cylindrical enclosures. *Applied Thermal Engineering*, 75:839–855, 2015.

[58] JM Khodadadi and Y Zhang. Effects of buoyancy-driven convection on melting within spherical containers. *International Journal of Heat and Mass Transfer*, 44(8):1605–1618, 2001.

[59] Joel H Ferziger and Milovan Peric. *Computational methods for fluid dynamics*. Springer Science & Business Media, 2012.

[60] Suhas Patankar. *Numerical heat transfer and fluid flow*. CRC press, 1980.

[61] Petr A Nikrityuk. *Computational thermo-fluid dynamics: In materials science and engineering*. John Wiley & Sons, 2011.

[62] Vaughan R Voller and C Prakash. A fixed grid numerical modelling methodology for convection-diffusion mushy region phase-change problems. *International Journal of Heat and Mass Transfer*, 30(8):1709–1719, 1987.

[63] W.D. Bennon and F.P. Incropera. A continuum model for momentum, heat and species transport in binary solid-liquid phase change systems-I. model formulation. *International Journal of Heat and Mass Transfer*, 30(10):2161–2170, 1987.

[64] F Dierich and PA Nikrityuk. A numerical study of the impact of surface roughness on heat and fluid flow past a cylindrical particle. *International Journal of Thermal Sciences*, 65:92–103, 2013.